Aspherical Supernovae

by

Daniel Nathan Kasen

B.S. (Stanford University) 1997
M.S. (University of California, Berkeley) 2000

A dissertation submitted in partial satisfaction of the
requirements for the degree of
Doctor of Philosophy

in

Physics

in the

GRADUATE DIVISION
of the
UNIVERSITY OF CALIFORNIA, BERKELEY

Committee in charge:
Dr. Peter Nugent, Co-Chair
Professor Eugene Commins, Co-Chair
Professor Christopher McKee
Professor Alexei Filippenko

Spring 2004

The dissertation of Daniel Nathan Kasen is approved:

Co-Chair Date

Co-Chair Date

Date

Date

University of California, Berkeley

Spring 2004

Aspherical Supernovae

Abstract

Aspherical Supernovae

by

Daniel Nathan Kasen
Doctor of Philosophy in Physics

University of California, Berkeley

Dr. Peter Nugent, Chair

Although we know that many supernovae are aspherical, the exact nature of their geometry is undetermined. Because all the supernovae we observe are too distant to be resolved, the ejecta structure can't be directly imaged, and asymmetry must be inferred from signatures in the spectral features and *polarization* of the supernova light. The empirical interpretation of this data, however, is rather limited – to learn more about the detailed supernova geometry, theoretical modeling must been undertaken. One expects the geometry to be closely tied to the explosion mechanism and the progenitor star system, both of which are still under debate. Studying the 3-dimensional structure of supernovae should therefore provide new breakthroughs in our understanding.

The goal of this thesis is to advance new techniques for calculating radiative transfer in 3-dimensional expanding atmospheres, and use them to study the flux and polarization signatures of aspherical supernovae. We develop a 3-D Monte Carlo transfer code and use it to directly fit recent spectropolarimetric observations, as well as calculate the observable properties of detailed multi-dimensional hydrodynamical explosion simulations. While previous theoretical efforts have been restricted to ellipsoidal models, we study several more complicated configurations that are tied to specific physical scenarios. We explore clumpy and toroidal geometries in fitting the spectropolarimetry of the Type Ia supernova

SN 2001el. We then calculate the observable consequences of a supernova that has been rendered asymmetric by crashing into a nearby companion star. Finally we fit the spectrum of a peculiar and extraordinarily luminous Type Ic supernova. The results are brought to bear on three broader astrophysical questions: (1) What are the progenitors and the explosion processes of Type Ia supernovae? (2) What effect does asymmetry have on the observational diversity of Type Ia supernovae, and hence their use in cosmology? (3) And, what are some of the physical properties of Type Ic supernovae, believed to be associated with gamma-ray bursts?

Dr. Peter Nugent
Dissertation Committee Chair

To increase the accuracy or simplicity of planetary theory, Ptolemy's successors added epicycles to epicycles and eccentrics to eccentrics, exploiting all the immense versatility of the fundamental Ptolemaic technique. But the seldom or never sought fundamental modifications of that technique. The problem of the planets had become simply a problem of design, a problem to be attacked principally by the rearrangement of existing elements. What particular combination of deferents, eccentrics, equants, and epicycles would account for the planetary motions with the greatest simplicity and precision?

Thomas Kuhn, *The Copernican Revolution*

Contents

List of Figures

List of Tables

Acknowledgments

For a lot of astronomers, science begins as a hobby and turns into a vocation, but for me it was more the other way around. The only reason I ever got anything done was because a few people showed me how to make the business into a creative opportunity. For this, I owe my advisor Peter Nugent; out of positive spirit he turned things around for me, defined my direction, gave me good ideas and the freedom to follow them. The same should be said of Eddie Baron and David Branch, "advisors away from home" and scientific role models; the turning point in my research was when I was given the chance to work with them. Thanks to my campus advisor Gene Commins, and to my committee members Alex Filippenko and Chris McKee; thanks to Lifan Wang, for his generous sharing of ideas and data; to Rollin, for storming the path that I so often followed; to Rachel, for teaching me about all the things I already thought I understood; and to Jon and Steph (the two people I look up to the most) and my parents who gave so much, and seemed so happy at the little I gave back. My dad actually read every paper in this thesis, head to toe, and even pretended they were interesting.

Chapter 1

Introduction

The explosion of a supernova must be a spectacular event, but it's something that we never directly see – the spectacle is over quickly, with no more than a brief and sudden flash. What we do observe for the months and years to come is the expanding mass of hot, radioactive material shot out in the explosion (the *supernova ejecta*). The ejecta can glow as bright as a billion suns; bright enough to be seen billions of light years away.

It's not so easy to understand what we are seeing. The light emanating from the ejecta is the result of a complicated array of physical processes. To interpret the observations, we need to model how light is generated within the ejecta, how the light interacts with material inside the ejecta, and what the light looks like when it finally escapes to be captured by our telescopes. The results of such *radiative transfer calculations* can be directly compared to observations, in particular the brightness, color, spectrum and polarization of the supernova light. In doing so we hope to constrain the physical properties of the ejecta, such as its mass, expansion velocities, and chemical composition. Studying supernova ejecta in this way provides our main clues to the nature of the explosion itself, and the progenitor star system that gave rise to it.

One might expect the *geometry* of the supernova ejecta to provide particularly valuable insight into the conditions that led to its ejection. Unfortunately, almost all observed supernovae are too distant to be resolved, so we can't directly image the ejecta

structure. The only recourse it to use three-dimensional (3-D) radiative transfer models to determine how the ejecta shape might affect those quantities that are observable, in particular the spectral features and *polarization* of the supernova light.

The goal of this thesis is to advance new techniques for calculating 3-D radiative transfer, and to use them to interpret recent observations of supernovae.

1.1 Asymmetry of Supernovae

For the most part, spherically symmetric models have been successful in explaining the bulk properties of many observed supernovae. However, there are several reasons, both theoretical and observational, to believe that supernovae may have an intricate 3-dimensional structure. Among the theoretically anticipated scenarios that could lead to an asymmetry, we might mention the following: (1) Explosions of an initially aspherical progenitor star, e.g., one distorted by rapid rotation (Yamada & Sato, 1990; Steinmetz & Hoeflich, 1992); (2) Explosions occurring in a binary star system, for example the merging of two white-dwarf stars (Webbink, 1984; Iben & Tutukov, 1984), or the impact of an exploding star on its nearby companion (Marietta et al., 2000); (3) Random asymmetries in the explosion physics due to Rayleigh-Taylor instabilities, convective mixing, or instabilities in the nuclear burning front (Chevalier & Klein, 1978; Burrows et al., 1995; Kifonidis et al., 2000; Gamezo et al., 2003); (4) Inherently asymmetric explosion mechanisms, such as supernovae powered by bipolar jets from an accreting black hole (MacFadyen & Woosley, 1999; Khokhlov et al., 1999; Maeda et al., 2002).

Several lines of observational evidence have shown that some supernovae are indeed aspherical, including: (1) The interesting morphologies of the nearby remnants of ancient supernova explosions, e.g. Cas A (Fesen & Gunderson, 1996; Hwang et al., 2000) and Tycho (Decourchelle et al., 2001), which show clumpy, filamentary, and occasionally "jet-like" structures; (2) The peculiar shape of some line features in the optical spectra of supernovae, which have been used to infer a clumpy distribution of line opacity, e.g., the "Bochum event" observed in the Hα feature of SN 1987A (Phillips & Heathcote, 1989;

Utrobin et al., 1995); (3) The non-zero polarization measured in several supernovae, which indicates a preferred orientation of the ejecta geometry (e.g., Wang et al., 1996a,b, 2003a,b; Leonard et al., 2000b; Leonard & Filippenko, 2001; Leonard et al., 2001, 2002).

The last of these – supernova polarization observations – promises to be a new breakthrough in the study of ejecta asymmetry. It has only been in the last five years or so that high quality polarization measurements of supernovae have started becoming routine. Such observations are exceedingly difficult, as the polarization level in supernovae is typically of order $\lesssim 1\%$. The recent breakthrough was only possible by spending hours of observing time on the largest telescopes, picking out the very small signal in the dim and quickly fading supernova light.

The focus of this thesis will be in studying the optical flux and polarization spectrum of supernovae in the early phases ($t \lesssim$ a few months). Empirical interpretation of this data is rather limited – therefore to learn more about the supernova geometry, theoretical modeling must been undertaken.

1.2 The Theoretical Supernova Problem

The theoretical modeling of supernova explosions is one of the most challenging problems in astrophysics, encompassing all of the following: (1) Stellar evolution calculations to evolve a main-sequence star (or stellar system) to the pre-supernova stage; (2) Calculations of the the neutrino transfer, hydrodynamics, and explosive nucleosynthesis that lead to the supernova eruption; (3) Radiation/hydrodynamics calculations of the expulsion of the stellar envelope and its subsequent expansion; (4) Radiative transfer calculations to compute the spectra and polarization of the final ejecta structure once it has reached the free-expansion stage.

The challenge of solving this full supernova problem in 3-D is a formidable one, and generally we will have to oversimplify many aspects of the simulations. However, given recent advances in multi-processor supercomputers, several large-scale computational programs are now beginning to simulate sophisticated supernova explosions in 3-D (e.g.

Fryxell et al., 2000; Mezzacappa et al., 2002; Reinecke et al., 2002; Gamezo et al., 2003; Fryer & Warren, 2004).

For the most part, the 3-D radiative transfer component in these projects has been neglected; the work of this thesis is thus a first step toward bridging the gap between the 3-D models and the recent advance of spectropolarimetric observations. Two general methodologies to the radiative transfer problem can be applied:

1. *The "top-down" approach:* From an observational perspective, radiative transfer calculations are needed to directly interpret newly acquired supernova data. In the "top-down" approach, one uses fast, highly parameterized models that often grossly simplify the physics of the radiative transfer. The model parameters are varied by hand in an empirical spirit until a good fit to the data is found. The extracted information on the ejecta structure can be used to speculate about the sort of theoretical scenarios needed to reproduce the observed supernova properties.

2. *The "bottom-up" approach:* From a theoretical perspective, radiative transfer calculations are needed as the final processing stage of first-principle hydrodynamical/explosion models. The output of such models (i.e., the density, velocities and composition of the ejecta structure) are not directly comparable to observations. In computing synthetic model light curves, spectra, and polarization, radiative transfer calculations provide the definitive test of which theoretical scenarios successfully explain the observed phenomenon. For this purpose, one desires radiative transfer codes of the highest physical accuracy, and with the fewest free parameters.

In general, both of these approaches to the radiative transfer problem are needed to advance our understanding of supernovae, and in this thesis, we will pursue examples of each.

1.3 Astrophysical Motivations

Besides being interesting objects in their own right, supernovae have a broad astrophysical relevance. Supernovae are the inevitable fate of massive stars and, in the same breath, the birthplace of compact objects such as neutron stars and (probably) black holes. The explosive nuclear burning in supernova explosions has synthesized most of the heavy elements that enrich the stars, and are required for the building of terrestrial planets (and ourselves). In addition, the remnants of supernovae are important in the reprocessing of the interstellar medium, and in the acceleration of cosmic rays.

These important roles played by supernovae have been known for some time. More recently, however, three exciting developments have piqued the astrophysicist's interest:

1. *The gamma-ray burst/supernova connection:* The one class of astrophysical phenomena that might match the raw explosive appeal of supernovae is the gamma-ray bursts (GRBs). That some GRBs may in fact be produced in supernova explosions has been the source of much speculation ever since the peculiar Type Ic supernova SN 1998bw was discovered in the error box of GRB 980425 (Galama et al., 1998). Recently, this connection was definitively confirmed with the detection of a supernova (SN 2003dh) in the optical afterglow of GRB 030329 (Hjorth et al., 2003; Stanek et al., 2003; Matheson et al., 2003). Most theoretical explanations of the supernova/GRB phenomenon involve highly asymmetric explosions, usually powered by bipolar jets (MacFadyen & Woosley, 1999). Spherical models have also been proposed (Tan et al., 2001). By studying the geometry and energetics of Type Ic supernova ejecta, we can hope to illuminate as well the progenitors and central engines of GRBs.

2. *The progenitors and explosion mechanism of Type Ia supernovae*: Type Ia supernovae (SNe Ia) are widely believed to be the thermonuclear explosion of a white dwarf. The exact nature of the progenitor system and the explosion scenario, however, remain unclear. Recent 3-D explosion models of SNe Ia have begun to make detailed predictions regarding the ejecta structure arising in different scenarios. For example, if SNe Ia

arise in a binary star system, the existence of a nearby companion star may introduce an asymmetry in the ejecta. The instabilities in the nuclear flame physics can also lead to a complicated "clumpy" ejecta structure. Thus, studying the geometry and polarization properties of SNe Ia will provide completely new insights into the origin of these events.

3. *Type-Ia supernovae and cosmology.* The high-luminosity and homogeneity of Type Ia supernovae makes them attractive tools for measuring the cosmological parameters, leading to the recent discovery of the acceleration of the universe (Riess et al., 1998; Perlmutter et al., 1999). In future cosmology experiments, the primary challenge is to refine SNe Ia as calibrated candles by reducing their intrinsic scatter in luminosity, and controlling for systematic errors due to potential evolution with redshift. A serious concern for cosmology applications is the increasing number of "peculiar" SNe Ia discovered in the last few years (e.g., Li et al., 2001a,b, 2003; Howell, 2004). Some SNe Ia are known from polarization observations to be aspherical, and this is likely responsible for some of the observed diversity.

While these issues are not the direct focus of this thesis, we will touch on each of them, as multi-dimensional studies of supernovae can make important contributions to our understanding.

1.4 Organization of this Thesis

The first two chapters of this thesis introduce the general concepts and techniques needed to approach the radiative transfer problem in supernovae. In **Chapter 2**, we provide a brief overview of supernovae, and describe the basic physical ideas behind their flux and polarization spectra. We introduce the Sobolev method for computing line formation in expanding atmospheres, and derive some new analytic formulae that can be used to derive the physical conditions in the ejecta directly from the shape of observed line features.

In **Chapter 3**, we attack the radiative transfer problem in earnest, adopting a

Monte Carlo strategy. We describe the structure of a code that handles arbitrary 3-D supernova geometries, and includes an integrated gamma-ray transfer routine, polarization calculations, and a radiative equilibrium solution of the atmospheric temperature structure.

The following three chapters consist of applications of the radiative transfer techniques. In **Chapter 4**, we study SN 2001el, the first normal Type Ia supernova to show a significant polarization signal (Wang et al., 2003a; Kasen et al., 2003b). Using a "top-down" approach, we simultaneously fit the flux and polarization of an unusual, high-velocity line feature. This allows us to constrain the geometry of the outer layers of supernova ejecta.

In **Chapter 5**, we take a "bottom-up" approach, calculating the optical properties of a multi-dimensional SN Ia hydrodynamical model. Marietta et al. (2000) have predicted that the impact of the supernova on a nearby companion star will carve out a conical hole in the ejecta. We show that this "ejecta-hole asymmetry" is in fact consistent with what is known about about SNe Ia, and may explain some of the observed polarization properties and spectral diversity (Kasen et al., 2003a). In addition, we describe a few polarization signatures of an ejecta hole that can be used in the future to test the binary progenitor scenario of SNe Ia.

In **Chapter 6** we explore the spectral properties of a very unusual Type Ic supernova. SN 1999as was one of the most luminous supernovae ever, more than 6 times brighter than SN 1998bw. But in contrast to SN 1998bw, its spectrum showed surprisingly low expansion velocities, as well as several peculiar narrow Fe II absorption features. We show first that the spherical "hypernova" explosion models used to explain SN 1998bw are inconsistent with the spectra of SN 1999as. We then argue that circumstellar interaction may have played an important role in powering the luminosity of this supernova, and in dramatically restructuring the outer layers of ejecta.

Chapter 2

The Spectra and Polarization of Supernovae

2.1 Overview of Supernovae

At its peak, the luminosity of a supernova can reach $L \approx 10^{43}$ ergs s^{-1}, or a few billion times the brightness of the sun. In some cases the supernova may outshine all of the stars in the galaxy from which it came.

The extraordinary luminosity suggests that supernovae have large surface areas. For objects bright at visible wavelengths, we expect blackbody temperatures around $T \approx$ 6000 K. Using the relationship $L = 4\pi R^2 \sigma T^4$, we find that the observed luminosity implies a radius of $R \approx 10^{15}$ cm, or twenty times larger than the radius of the largest supergiant stars. To explain this large radius, we might suppose that the supernova has expanded to its present size over the 20 days or so it took it to reach peak brightness. The implied velocity of the material is then $R/t \approx 10^9$ cm s^{-1}, or a few percent of the speed of light. These kind of velocities are in fact observed in the Doppler shifts of absorption lines in the supernova spectrum.

Typically the luminosity of a supernova rises to and declines from its peak in a

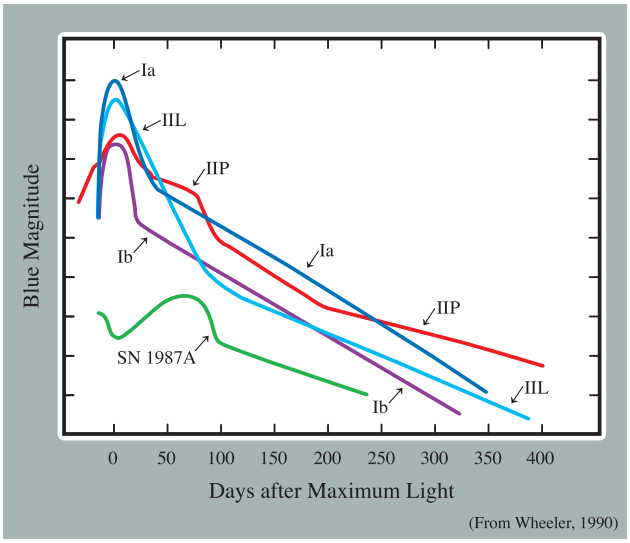

Figure 2.1 Light curves of different types of supernovae (from Wheeler, 1990). Each tick mark on the vertical axis corresponds to one magnitude.

period of $t_p \approx$ a few months (see Figure 2.1). Assuming that this temporal behavior results from the diffusion of photons out of the optically thick ejecta, we can make a rough estimate of the mass of the supernova material. A typical photon will take $N = (R/\lambda_p)^2$ steps in random walking out of the ejecta, where λ_p is the mean free path and R the ejecta radius. Using $\lambda_p = \kappa\rho$ and $R = vt_d$, we can solve for the diffusion time $t_d \approx N\ \lambda_p/c$,

$$t_p \approx \sqrt{\frac{\kappa M}{cv}} \approx 60 \text{ days} \left(\frac{M}{M_\odot}\right)^{1/2} \left(\frac{10^9 \text{ km s}^{-1}}{v}\right)^{1/2} \left(\frac{\kappa}{0.4 \text{ g cm}^{-2}}\right)^{1/2}, \qquad (2.1)$$

where the opacity $\kappa \approx 0.4$ is appropriate for electron scattering in ionized hydrogen. The observation $\tau_p \approx 60$ days suggests $M \sim 1M_\odot$. Longer duration luminosities (e.g., the SN IIP) may correspond to larger ejecta masses. Once the ejecta become optically thin, the light curve reaches a "tail" where the luminosity declines exponentially (Figure 2.1).

A supernova therefore consists of roughly a few solar masses or so of material expanding at high velocity, which suggests that we are witnessing the remnants of an exploded star. The implied kinetic energy of the explosion is large, $E_k \approx 1/2Mv^2 \approx 10^{51}$ ergs. By

comparison, the total energy the supernova radiates over its lifetime is about $E_r \sim Lt_d \approx 10^{49}$ ergs; thus although supernovae are incredibly luminous, their radiated energy is only about 1 percent of the total kinetic energy.

What might the source of this enormous energy be? Two possibilities are believed to be realized:

(1) *Core collapse supernovae*: After massive ($M \gtrsim 10M_\odot$) stars have exhausted their nuclear fuel, the inner core collapses to form a neutron star. The gravitational binding energy of a cool neutron star ($\sim 3 \times 10^{53}$ ergs) is sufficient to power a supernova, although it is not clear how exactly this energy is tapped to explode the star. The collapse releases a few times 10^{52} ergs in neutrinos, which are thought to energize a shock wave in the stellar envelope. Detailed 1-D simulations of this process, however, fail to produce a supernova (Burrows & Thompson, 2003), and therefore multidimensional effects (e.g., convection) appear to be essential. There is also the possibility that some stellar cores collapse all the way to form a black hole, after which the outer layers may be ejected through an energetic, bipolar jet (Woosley, 1993).

(2) *Thermonuclear supernovae*: There are various scenarios whereby a supernova may be triggered by the thermonuclear disruption of a carbon/oxygen white dwarf. For reasons discussed by Branch et al. (1995), Livio (2000), and others, the current favored progenitor scenario involves a white dwarf accreting material from a non-degenerate companion star (the *single-degenerate scenario*). When the mass of the accreting white dwarf approaches the limiting Chandrasekhar mass $M_{ch} \approx 1.4M_\odot$, the temperature in the center becomes high enough to ignite carbon. The energy released in carbon burning heats the star, which increases the burning rate further; because the white dwarf is degenerate, thermal pressure is initially insufficient to expand the star and quench the burning – the result is a thermonuclear runaway. The energy liberated in burning carbon and oxygen is about 8×10^{17} ergs/g, so that incinerating about $\sim 0.6\ M_\odot$ of the white dwarf results in $\sim 10^{51}$ ergs, sufficient to unbind the star and power a supernova explosion. Such thermonuclear explosions are labeled Type Ia supernovae (SNe Ia).

Immediately following a SN Ia explosion, the energy released from nuclear burn-

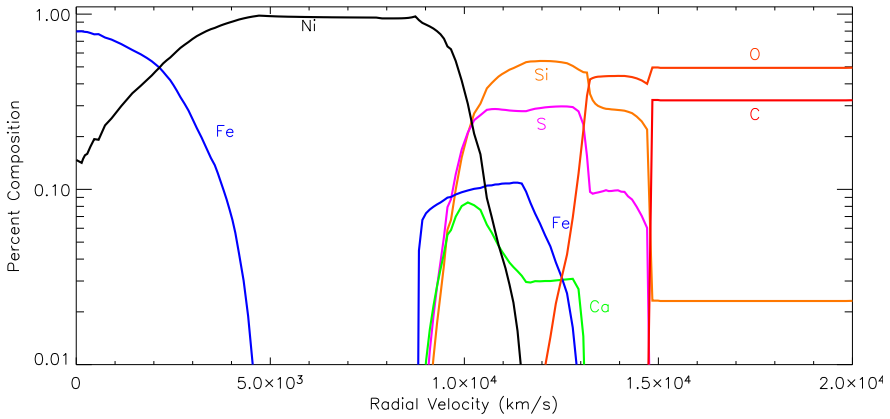

Figure 2.2 Composition structure of the spherical Type Ia explosion model W7, immediately following the explosion; from Nomoto et al. (1984).

ing is about equally split between the kinetic energy and the thermal energy of the hot expanding ejecta. However, because the progenitors of SNe Ia are compact white dwarfs of small radius ($R \approx 5 \times 10^8$ cm), they cool very quickly by adiabatic expansion. The cooling occurs as each hot shell of ejecta does $P\ dV$ work and accelerates the shell ahead of it – in this way almost all of the thermal energy from the explosion is converted into kinetic energy. This leaves the question of what powers the optical display; the answer is that the SN Ia luminosity is solely powered by the decay of radioactive isotopes synthesized in the explosion, in particular ^{56}Ni, which releases energetic gamma-rays in the decay chain $^{56}\mathrm{Ni} \rightarrow {}^{56}\mathrm{Co} \rightarrow {}^{56}\mathrm{Fe}$. The gamma-rays are absorbed and thermalized in the ejecta, to eventually re-emerge as the optical photons we observe.

Because ^{56}Ni is a doubly-magic nucleus, it is typically the primary isotope synthesized whenever temperatures are high enough to reach nuclear statistical equilibrium ($T_{nse} \approx 5 \times 10^9$ K). Figure 2.2 shows the resulting composition structure in a parameterized, spherical SN Ia explosion model (the w7 model; Nomoto et al., 1984). Most of the inner layers of the model are completely burned to ^{56}Ni (although in the very center the high neutrino excess favors production of ^{54}Fe). Above the ^{56}Ni zone, the temperatures

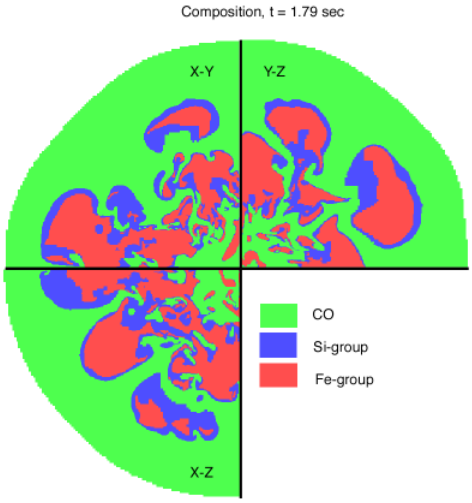

Figure 2.3 Composition structure of a 3-D Type Ia deflagration explosion model; from Khokhlov (1994).

are insufficient to completely burn C/O, and mostly silicon and sulfur are produced, along with some calcium and magnesium. Such intermediate-mass elements are prominent in the spectra of SNe Ia. The very outer layers of the model consist of unburned carbon and oxygen from the original white dwarf.

Realistic 3-D models of SN Ia explosions fail to show the stratified composition structure of Figure 2.2. For example, Figure 2.3 shows the result of a 3-D simulation of the deflagration (i.e., subsonic, turbulent burning) of a white dwarf (Khokhlov, 1994). Because the hot burned material is buoyant and hydrodynamically unstable, one finds plumes of ^{56}Ni floating upward in a substrate of unburned C/O. Whether this sort of highly aspherical explosion produces a realistic-looking SN Ia is not yet clear; the question awaits detailed 3-D radiative transfer calculations like those begun in this thesis. If not, one may rather favor a scenario where the subsonic deflagration transitions into a supersonic detonation, which would quickly burn away the inhomogeneities (Khokhlov, 1991). Unfortunately, the physics of such a deflagration-to-detonation transition is not well understood.

2.2 Spectra of Supernovae

Empirically, supernovae are classified according to the line features appearing in their optical spectra (Figure 2.4). The spectra provide a powerful observational probe into the structure of the supernova ejecta, with the strength of line features constraining the supernova composition and density structure, and the Doppler shifts of lines indicating the expansion velocities. In supernovae, the expansion follows a homologous velocity law, where the velocity is porportional to radius $\vec{v} = \vec{r}/t_{\rm exp}$ ($t_{\rm exp}$ is the time elapsed since the explosion). This is just the equation of material freely expanding in the abscence of forces. Such a flow is self-similar, such that over time the structure of the ejecta remains fixed in velocity coordinates. For this reason we prefer to use velocity as a radial coordinate, where it is understood that a "velocity distance" v corresponds to a physical distance $vt_{\rm exp}$. The line flux at different Doppler shifts thus gives us information regarding the distribution of the supernova ejecta in velocity space.

During the early, optically thick phases, the spectra of supernovae consist of broad line features superimposed on a pseudo-blackbody continuum. The line profiles have a characteristic P-Cygni shape, consisting of a blueshifted absorption and a redward emission feature (see Figure 2.5). The shape and width of the profile is the natural result of Doppler shifts arising from the expansion of the supernova ejecta. In the simple diagram of Figure 2.5, the continuum flux can be thought of as coming from the surface of an optically thick photosphere (the "light bulb shining through the fog"). Line formation occurs in the "fog" above the photosphere, which we call the supernova *atmosphere*. The line opacity in the region directly intervening between the photosphere and the observer (the "absorption region") scatters or absorbs flux from the photosphere, thereby causing an absorption feature. As the material in the absorption region is moving toward the observer, the absorption feature is blueshifted. Material outside of this "tube" (the "emission region") does not obscure the photosphere, but rather scatters or emits additional flux *into* the observer line of sight. This leads to an emission feature that is centered on the line rest wavelength. The material in the tube behind the photosphere (the "occluded region") is not visible at

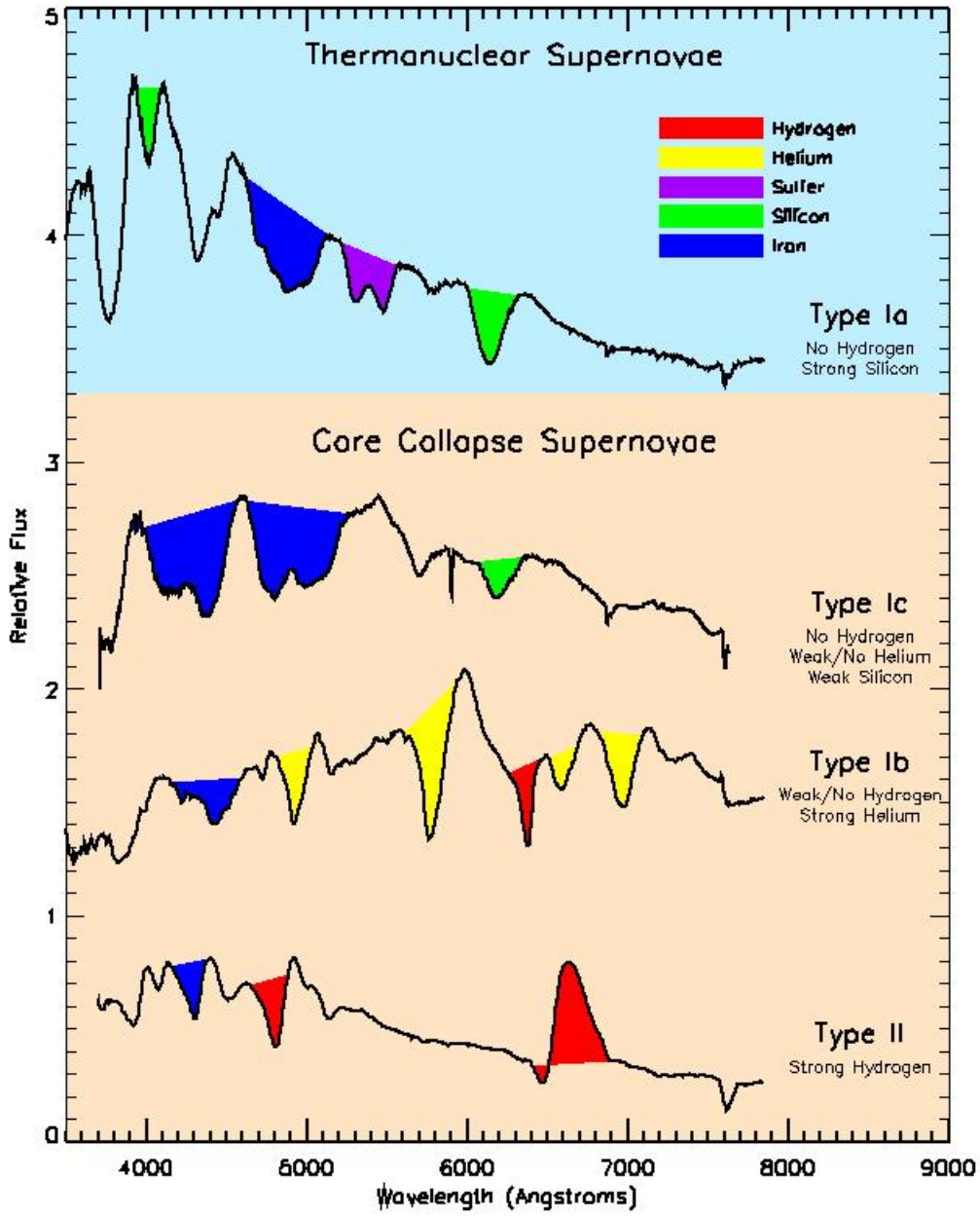

Figure 2.4 The spectral classification of supernovae.

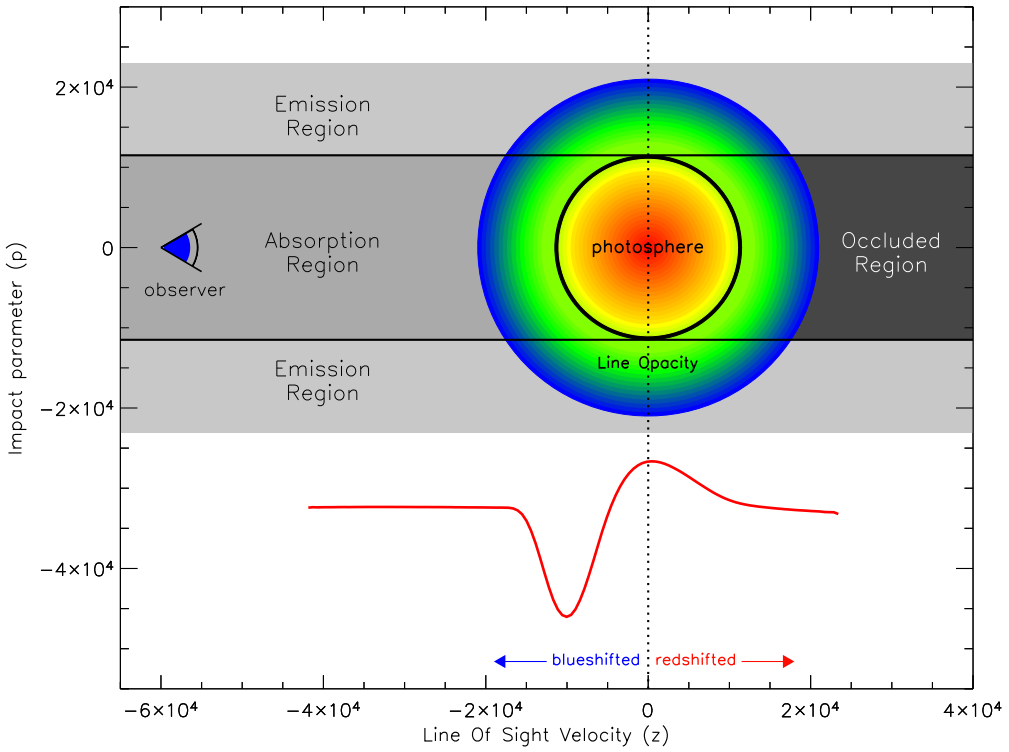

Figure 2.5 Formation of the P-Cygni line profile. All the material on a vertical plane perpendicular to the observer's line of sight has the same component of velocity along the observer's line of sight, and hence the same Doppler shift.

all.

The breadth of P-Cygni profiles in supernova spectra reflects the fact that the ejecta velocity along the observer's line of sight typically ranges from $\sim -20,000$ to $20,000$ km s^{-1}, corresponding to a Doppler shift width of 600 Å at 5000 Å. Because of this breadth, each feature in a supernova spectrum is typically a blend of the P-Cygni profiles from many different line transitions. This greatly complicates the identification and analysis of the line features.

2.2.1 Calculation of Line Profiles

Because the P-Cygni profile will be a focal point of this thesis, it is useful to consider the line formation in more detail. As a useful heuristic, we assume that the continuum flux emerges from an optically thick, sharply delineated photosphere, and that there is no continuous opacity above the photosphere. The photosphere represents the surface at which the optical depth to electron scattering equals one – in reality a sharp distinction does not exist, rather there is a gradual transition from the optically thick to optically thin regimes.

Consider a photon emanating from the photosphere and propagating through this atmosphere toward the observer (labeled the z direction). Because the atmosphere is in differential expansion, the wavelength of the propagating photon is constantly Doppler shifting with respect to the local co-moving frame. If the photon wavelength in the observer frame is λ, then its co-moving wavelength is given by the (non-relativistic) Doppler formula

$$\lambda_{loc} = \lambda\left(1 + \frac{\vec{v}\cdot\hat{z}}{c}\right) = \lambda\left(1 + \frac{z}{ct_{\exp}}\right), \tag{2.2}$$

where we have assumed a homologous expansion law. Suppose the only opacity in the atmosphere is due to a single line with rest center wavelength λ_0. The photon will come into resonance with the line when $\lambda_{loc} = \lambda_0$, which by Equation 2.2 is at a point

$$z_r = ct(\lambda_0/\lambda - 1). \tag{2.3}$$

The region where the photon encounters the line opacity is known as a *resonance region.* Because the intrinsic width of the line is typically very small (thermal Doppler velocity of $v_d \approx 5$ km s^{-1}) compared to the dimensions over which the properties of the atmosphere vary ($v \approx 1000$ km s^{-1}), the resonance region is in fact very small and can be approximated by a point. This is known as the Sobolev approximation, or narrow line limit, and will be applied repeatedly throughout this thesis.

Let I_p be the specific intensity of a beam emerging from the photosphere in the z direction along a beam given by coordinates x, y. The intensity that reaches the observer

at infinity after passing through the line forming region is given by the Sobolev formalism

$$I_\lambda(x,y) = I_p(x,y)e^{-\tau} + (1-e^{\tau})S(x,y,z_r), \tag{2.4}$$

where τ is the Sobolev line optical depth at the resonance point (x,y,z_r) and S is the line source-function at this point. The first term in Equation 2.4 represents the photospheric light attenuated by the line optical depth; the second term represents light scattered or created to emerge into the line of sight by the line.

To generate the observed spectrum of an unresolved object, the specific intensity of Equation 2.4 must be integrated over the projected surface of the atmosphere, i.e., over the $x-y$ plane. Thus, a wavelength λ in the observed spectrum gives us information about the line optical depth and source function integrated over a plane at z_r, perpendicular to the observer's line of sight. Because all the material on such a z-plane has the same velocity component along the observer's line of sight (and hence the same Doppler shift, Equation 2.2) it is called a constant-velocity (CV) surface.

For a spherical atmosphere, it is useful to use polar coordinates (z,p,ϕ) such that the observer's line of sight is the z direction, with z increasing away from the observer. Let $v_{\rm ph}$ be the velocity of the photosphere, and $r_{\rm ph} = v_{\rm ph}t_{\rm exp}$ its radius. The emergent flux can then be written as an integral over the impact parameter p,

$$\begin{aligned} \frac{F(z)}{2\pi} &= \int_0^{p_0} I_{\rm ph} p\,dp + \int_{p_0}^{\infty} S(r)(1-\zeta(r))p\,dp + \int_{p_0}^{r_{\rm ph}} I_{\rm ph}\zeta(r)p\,dp \\ &= \frac{1}{2}p_0^2 I_{\rm ph} + \int_{p_0}^{\infty} S(r)(1-\zeta(r))p\,dp + \int_{p_0}^{r_{\rm ph}} I_{\rm ph}\zeta(r)p\,dp, \end{aligned} \tag{2.5}$$

where $\zeta(r) = e^{-\tau(r)}$ and $F(z)$ is the observed flux (apart from a factor of $1/D^2$, where D is the distance to the supernova) at wavelength $\Delta\lambda = \lambda - \lambda_0 = \lambda_0 z/ct$. The limit p_0 is given by the p location of the spherical photosphere for a given z, namely

$$p_0 = \begin{cases} 0 & \text{for } z \le -r_{\rm ph} \quad \text{(blue side)} \\ \sqrt{r_{\rm ph}^2 - z^2} & \text{for } -r_{\rm ph} < z < 0 \quad \text{(mid region)} \\ r_{\rm ph} & \text{for } z \ge 0 \quad \text{(red side)} \end{cases}$$

In what follows, we call the part of the line profile where $z < -r_{\rm ph}$ the blue side, the part where $-r_{\rm ph} < z < 0$ the mid region, and the part where $z \geq 0$ the red side.

2.2.2 Inversion of Supernova Lines

For a given line in a spherical supernova atmosphere, one can specify $\tau(r)$ and $S(r)$ and use Equation 2.5 to calculate a synthetic line profile. The values of $\tau(r)$ and $S(r)$ can then be adjusted through trial and error until they provide a good fit to observations; in this way we hope to constrain the composition and distribution of the supernova ejecta (e.g., Millard et al., 1999; Hatano et al., 1999). However, given the relative simplicity of Equation 2.5, it is possible, under certain conditions, to solve this inverse problem mathematically. For example, Ignace & Hendry (2000) derived an analytic formula that gave a combination of $S(r)$ and $\tau(r)$ as a function of the derivative of the red side of an emission feature. Here we derive a complete inversion solution for extracting both $S(r)$ and $\tau(r)$ from an observed line profile (Kasen et al., 2002).

We derive the inversion formulae assuming spherical symmetry, a homologously expanding atmosphere surrounding a sharp continuum-emitting photosphere that absorbs any flux scattered back onto it, no continuous opacity, and no line blending. Even when these assumptions are not strictly valid, the formulae should still give considerable insight into the physical conditions in the atmosphere. On the other hand, the limitations of the formulae provide an interesting result in their own right – they clearly show what type of features are impossible under the above assumptions, making it obvious where more complicated scenarios must be invoked to explain a spectrum. Of most interest to us, of course, are potential signatures of the breakdown of spherical symmetry.

Inversion for $\tau(r)$

We consider the inversion of each region of the line in turn, beginning with the mid region. The mid region of the line profile turns out to be sensitive only to the optical depth of the line near the photosphere. Using Equation 2.5, we change the integration variable

from p to $r = \sqrt{p^2 + z^2}$, and divide through by $I_{\rm ph}$

$$\frac{r_{\rm ph}^2}{2} f(z) \quad = \quad \int_{|z|}^{r_{\rm ph}} r\, dr + \int_{r_{\rm ph}}^{\infty} s(r)(1-\zeta(r)) r\, dr + \int_{r_{\rm ph}}^{\sqrt{z^2+r_{\rm ph}^2}} \zeta(r) r\, dr, \tag{2.6}$$

where we have defined $s(r) = S(r)/I_{\rm ph}$ and $f(z) = F(z)/(\pi I_{\rm ph} r_{\rm ph}^2)$ (i.e. the total flux divided by the continuum flux). $I_{\rm ph}$ has been assumed to be constant over the line profile.

Written this way we see that the term involving the source function is independent of z and so contributes a constant amount to the flux for every wavelength point in the mid region. The derivative of the mid region is therefore independent of the source function. The change in flux from a velocity surface at z to one at $z - \Delta z$ is due only to the fact that a bit more of the photosphere is now obscured by the optical depth of the line. One then expects the derivative df/dz to depend only on the optical depth.

Since the terms in Equation 2.6 only depend on z in the limits of the integral we can differentiate the integrals using Leibnitz' rule

$$\frac{d}{dz} \int_{\xi(z)}^{\eta(z)} g(t)\, dt = g(\eta)\frac{d\eta}{dz} - g(\xi)\frac{d\xi}{dz}. \tag{2.7}$$

Applying Equation 2.7 to Equation 2.6 allows us to solve for $\zeta(r)$,

$$\zeta(r = \sqrt{r_{\rm ph}^2 + z^2}) = 1 - \frac{r_{\rm ph}^2}{2|z|}\frac{df}{dz} = 1 - \frac{\lambda_0^2}{2|\Delta\lambda|}\frac{df}{d\Delta\lambda}\left(\frac{v_{\rm ph}}{c}\right)^2, \tag{2.8}$$

which is valid for $-r_{\rm ph} < z < 0$. In using Equation 2.8 to calculate $\zeta(r)$ from a spectrum, one can choose either $\Delta\lambda$, z, or r as the independent parameter. For instance, from $\Delta\lambda$ (which is always less than zero for Equation [2.8]) the other two parameters are determined by $z = r_{\rm ph}(\Delta\lambda/\lambda_0)(c/v_{\rm ph})$ and $r = \sqrt{r_{\rm ph}^2 + z^2}$. The velocity of the photosphere must be determined independently from a different line in the spectrum.

Equation 2.8 gives us some immediate insight into the relationship between line shape and optical depth. The steepness of the mid region (once the photospheric velocity has been scaled out) is a direct indication of the Sobolev optical depth. If no line feature exists, then $df/dz = 0$ and hence $\zeta = 1$ (i.e., $\tau = 0$). Thus, the absence of a feature implies

either negligible line optical depth or the breakdown of our assumptions – in this formalism there is no choice for the source function that allows a line to "erase" itself. A stair-step mid region could be a signal that the optical depth near the photosphere is oscillating between small and large values (i.e., the medium is clumpy in the radial direction).

Equation 2.8 only gives the value of ζ for the radial region $r_{\rm ph} < r < \sqrt{2} r_{\rm ph}$. This is expected to be the region of highest density opacity in the atmosphere. Nevertheless, in the following we show how it is possible to extend the solution for $\zeta(r)$ to arbitrary r by using information from the blue and red sides of the line profile.

Inversion for $S(r)$

We next consider the inversion of the red side of the line, which will allow us to solve for the source function. For the red side, the flux is given by a source term plus an unobstructed photosphere term

$$\frac{r_{\rm ph}^2}{2} f(z) = \frac{1}{2} r_{\rm ph}^2 + \int_{\sqrt{r_{\rm ph}^2 + z^2}}^{\infty} s(r)(1-\zeta(r)) r \, dr. \tag{2.9}$$

The second term in Equation 2.9 is a constant with respect to z since the photosphere is always completely unobscured for $z > 0$. The same technique of differentiating the integral allows us to solve for $s(r)$,

$$\begin{aligned} s(r = \sqrt{r_{\rm ph}^2 + z^2}) &= -\frac{r_{\rm ph}^2}{1-\zeta(r)} \frac{1}{2z} \frac{df}{dz} \\ &= -\frac{1}{1-\zeta(r)} \frac{\lambda_0^2}{2\Delta\lambda} \frac{df}{d\Delta\lambda} \left(\frac{v_{\rm ph}}{c} \right)^2 \end{aligned} \tag{2.10}$$

which is valid for all $z \geq 0$ and the independent parameter can be chosen to be any of $\Delta\lambda$, z, or r. This is essentially the same result derived by Ignace & Hendry (2000). Because Equation 2.8 together with Equation 2.14 (see below) gives ζ everywhere, Equation 2.10 can be used to determine the source function at all radii above the photosphere. Note that if $\tau = 0$, then $\zeta = 1$ and Equation 2.10 is undefined – if a line has no optical depth it is of course impossible to determine its source function. For large optical depth, $\zeta = 0$, and the

shape of the red side depends on the source function only. Since $s \geq 0$ and $\zeta \leq 1$ we must have $df/dz \geq 0$ on the red side – the red side always decreases (or stays flat) to the red.

Inversion for $\tau(r)$ for $r > \sqrt{2}r_{\rm ph}$

Finally, the flux from the blue side of the profile will allow us to extend the solution of ζ to large r. The flux is given by a source term plus a fully obstructed photosphere

$$\frac{r_{\rm ph}^2}{2} f(z) = \int_{|z|}^{\infty} s(r)(1-\zeta(r)) r\, dr + \int_{|z|}^{\sqrt{r_{\rm ph}^2+z^2}} \zeta(r) r\, dr. \tag{2.11}$$

The same differentiation technique yields

$$\zeta(r=\sqrt{r_{\rm ph}^2+z^2}) = \zeta(|z|) + s(|z|)\{1-\zeta(|z|)\} - \frac{r_{\rm ph}^2}{2|z|}\frac{df}{dz}, \tag{2.12}$$

which is valid for $z < -r_{\rm ph}$. Making use of spherical symmetry, Equation 2.10 can be used to replace the second term in Equation 2.12 with

$$s(|z|)(1-\zeta(|z|)) = -\frac{r_{\rm ph}^2}{2z_+}\frac{df(z_+)}{dz}, \tag{2.13}$$

where $z_+ = \sqrt{z^2 - r_{\rm ph}^2}$. Combining Equations 2.12 and 2.13 we obtain

$$\begin{aligned} \zeta(r=\sqrt{z^2+r_{\rm ph}^2}) \;\; &= \;\; \zeta(r=|z|) \\ &\quad -\frac{\lambda_0^2}{2}\left(\frac{v_{\rm ph}}{c}\right)^2 \left\{ \left[\frac{1}{\Delta\lambda}\frac{df}{d\Delta\lambda}\right]_{\Delta\lambda=\frac{\lambda_0}{ct}\sqrt{z^2-r_{\rm ph}^2}} + \left[\frac{1}{|\Delta\lambda|}\frac{df}{d\Delta\lambda}\right]_{\Delta\lambda=-\frac{|z|\lambda_0}{ct}} \right\}, \end{aligned} \tag{2.14}$$

where $|z| > r_{\rm ph}$ is the independent parameter for evaluating $\zeta(r=\sqrt{z^2+r_{\rm ph}})$ from $\zeta(r=|z|)$ and df/dz. Given $\zeta(r)$ for $r \in [nr_{\rm ph}, \sqrt{n+1}r_{\rm ph}]$, Equation 2.14 allows us to evaluate $\zeta(r)$ for $r \in [\sqrt{n+1}r_{\rm ph}, \sqrt{n+2}r_{\rm ph}]$, where $n \geq 1$ is an integer. Beginning with $\zeta(r)$ for $r \in [r_{\rm ph}, \sqrt{2}r_{\rm ph}]$, given by Equation 2.8, we can in fact use Equation 2.14 to find $\zeta(r)$ for all values of r.

The applicability of the inversion formulae presented here will necessarily be limited by the numerous assumptions that went into their derivation. Nevertheless, it is interesting to note that this particular inversion problem possesses a unique solution for both

$S(r)$ and $\tau(r)$. A persistent worry in supernova modeling is that very different physical parameters may lead to identical looking synthetic spectra. The analytic solutions above demonstrate that, at least in principle, each different choice of $S(r)$ and $\tau(r)$ produces a distinct line profile (although in practice it may be impossible to discern the differences from noisy data). For aspherical geometries, a unique inversion is obviously no longer possible. For a 3-D atmosphere, τ and S may vary arbitrarily across a given CV plane, but all the information is integrated over to produce the flux at the corresponding wavelength. Thus in pressing forward with our investigations into the 3-D structure of supernovae, we are plainly facing an insoluble inverse problem.

2.3 Polarization of Supernovae

While the flux spectra of supernovae may offer limited insight into the ejecta geometry, measurements of the *polarization* of supernova light provide a direct probe of asymmetry (Shapiro & Sutherland, 1982). Because a spherically symmetric system has no preferred direction, the net polarization must cancel – a non-zero polarization detection demands some degree of asymmetry. In the last five years or so, high quality supernova polarization measurements have become increasingly available. The latest *spectropolarimetric* observations have relatively good signal-to-noise ratio and spectral resolution, allowing us to study the polarization over individual line features.

Observers have now detected polarization in supernovae of all types. Notable polarization observations of Type II core-collapse supernovae include SN 1987A (Cropper et al., 1988; Bailey, 1988), SN 1993J (Trammell et al., 1993; Höflich et al., 1996; Tran et al., 1997), SN1999em (Leonard et al., 2001), and the Type IIn SN 1998S (Leonard et al., 2000a). Polarization measurements of Type Ic supernovae include the highly polarized SN 1997X (Wang et al., 2001) and the "hypernova-like" SN 2002ap (Leonard et al., 2002; Wang et al., 2003b). On average, the polarization in thermonuclear supernovae appears to be lower than in the core collapse SNe (Wang et al., 1996b, 1997; Leonard et al., 2000b). Nevertheless, a strong polarization signal of $\sim$0.7% was detected in the subluminous and spectroscopically

peculiar SN 1999by (Howell et al., 2001), and polarization of ∼0.4% has also been measured in the normal Type Ia supernova SN 2001el, the subject of our studies in Chapter 4.

2.3.1 Polarization Basics

The polarization state of light describes an anisotropy in the time-averaged vibration of the electric field vector. A beam of radiation where the electric field vector vibrates in one specific plane is completely (or fully) linearly polarized. A beam of radiation where the electric field vector vibrates with no preferred direction is unpolarized. Imagine holding a polarization filter in front of a completely linearly polarized light beam of intensity I_L. The filter only transmits the component of electric field parallel to the filter axis. Thus as the filter is rotated, the transmitted intensity, which is proportional to the square of the electric field, varies as $I(\theta) = I_L \cos^2\theta$ (where θ is the angle between the electric field and the filter axis).

The light measured from astrophysical objects is the super-position of many individual waves of varying polarization. Imagine a light beam consisting of the super-position of two completely linearly polarized beams of intensity I_L and I_R, whose electric field vectors are oriented 90° to each other. If the beams add incoherently, the transmitted intensity is the sum of each separate beam intensity

$$I(\theta) = I_L \cos^2\theta + I_R \cos^2(\theta + 90^\circ) = I_L \cos^2\theta + I_R \sin^2\theta. \tag{2.15}$$

If the beams are of equal intensity, $I_L = I_R$, then the transmitted intensity shows no directional dependence upon θ – i.e., the light is unpolarized. In this sense, we say that the polarization of a light beam is "canceled" by an equal intensity beam of orthogonal – or "opposite" – polarization. If $I_L \neq I_R$ the cancellation is incomplete, and the beam is said to be *partially linearly polarized*. The degree of polarization P is defined as the maximum percentage change of the intensity, in this case

$$P = \frac{I_L - I_R}{I_L + I_R}. \tag{2.16}$$

The polarization position angle (labeled χ) is defined as the angle at which the transmitted intensity is maximum.

It is tempting to think of the polarization as a (two dimensional) vector, since it has both a magnitude and a direction. Actually the polarization is a percent difference in intensity, and intensity is the *square* of a vector (the electric field). The polarization is actually a quasi-vector; that is, polarization directions 180° (not 360°) apart are considered identical. The additive properties of the polarization thus differ slightly from the vector case, as evidenced by the fact that the polarization is canceled by another equal beam oriented 90° to it, rather than one at 180° as in vector addition.

In this case, a useful convention for describing polarization is through the *Stokes parameters*, I, Qm and U, which measure the difference of intensities oriented 90° to each other. A Stokes vector can be defined and illustrated pictorially as (Landi degl'Innocenti, 2002)

$$\mathbf{I} = \begin{pmatrix} I \\ Q \\ U \end{pmatrix} = \begin{pmatrix} I_{0^\circ} + I_{90^\circ} \\ I_{0^\circ} - I_{90^\circ} \\ I_{45^\circ} - I_{-45^\circ} \end{pmatrix}, = \begin{pmatrix} \updownarrow + \leftrightarrow \\ \updownarrow - \leftrightarrow \\ \nwarrow\!\!\!\searrow - \swarrow\!\!\!\nearrow \end{pmatrix} \tag{2.17}$$

where I_{90°, for instance, designates the intensity measured with the polarizing filter oriented 90° to a specified direction called the polarization reference direction. To determine the superposition of two polarized beams, one simply adds their Stokes vectors. (A fourth Stokes parameter V measures the circular polarization of the radiation, but will not be discussed further, as circular polarization measurements have not been attempted for supernovae. For scattering atmospheres without magnetic fields, the radiative transfer equation for circular polarization separates from the linear polarization equations, allowing us to ignore V in our calculations).

We further define the fractional polarizations $q = Q/I$ and $u = U/I$. The degree of polarization (P) and the position angle (χ) can then be written in terms of the Stokes

Parameters

$$P = \frac{\sqrt{Q^2 + U^2}}{I} = \sqrt{q^2 + u^2}, \tag{2.18}$$

$$\chi = \frac{1}{2}\tan^{-1}(U/Q) = \frac{1}{2}\tan^{-1}(u/q). \tag{2.19}$$

2.3.2 Polarization In Supernova Atmospheres

The light from supernovae originates in thermal emission processes, which, being the result of random collisional processes, are necessarily unpolarized. The cause of polarization is believed to be the subsequent scattering by electrons, a dominate source of opacity in the hot, ionized atmospheres of supernovae.

To understand the polarizing effect of electron scattering, note that an electron scatters a fully polarized beam of radiation according to a dipolar $\sin^2\psi$ angular distribution (where ψ is the angle measured from the incident polarization direction). As mentioned above, incident unpolarized light can be considered the sum of two fully polarized beams oriented perpendicular to each other. The effect of the electron scatter is then to redistribute each of these polarized beams according to a differently oriented dipole pattern. In certain directions, therefore, the two beams no longer cancel and the polarization is non-zero. By careful consideration of the geometry of the $\sin^2\psi$ redistribution, the effect of an electron scattering on the Stokes vector $\mathbf{I}_{\rm in}$ can be expressed as

$$\mathbf{I}_{\rm out} = \frac{3}{2}\begin{pmatrix} \cos^2\Theta + 1 & \cos^2\Theta - 1 & 0 \\ \cos^2\Theta - 1 & \cos^2\Theta + 1 & 0 \\ 0 & 0 & 2\cos\Theta \end{pmatrix}\mathbf{I}_{\rm in}, \tag{2.20}$$

where Θ is the angle between the incoming and the scattered photon. The matrix acting on $\mathbf{I}_{\rm in}$ is called the Rayleigh phase matrix. The degree of polarization of scattered, initially unpolarized light is seen to be

$$P = \frac{1 - \cos^2\Theta}{1 + \cos^2\Theta}. \tag{2.21}$$

Light scattered at 90° is fully polarized, while that forward scattered at 180° remains unpolarized. The direction of the polarization is perpendicular to the scattering plane,

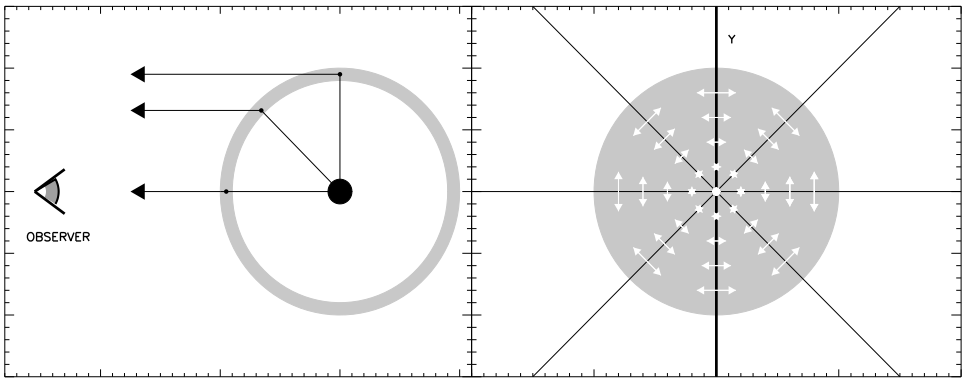

Figure 2.6 The polarization of a supernova atmosphere illustrated by a simple model: an unpolarized central source and a thin electron scattering shell (left side). Light from the edge of the shell has scattered at nearly 90° and is is highly polarized, while that from the center has scattered at 180° and is unpolarized. To the observer, the polarization of the shell will appear as illustrated on the right.

defined by the incoming and outgoing photon directions.

In general, the radiation incident on an electron will come from many directions at once. In order for the *net* scattered light to be polarized, the incident radiation field must possess some degree of anisotropy. For example, deep within the supernova atmosphere where the opacity is high, the trapping of photons leads to a radiation field that is nearly isotropic. Because the radiation incident on a scatterer is then nearly equal in all directions, the net polarization of scattered light cancels. On the other hand, in the outer optically thin layers of the supernova, the radiation field becomes highly anisotropic as photons stream radially out of the atmosphere. We therefore expect the polarization of the supernova light to occur mostly near and above the photosphere.

The right side of Figure 2.6 illustrates how the polarization of specific intensity beams emergent from a spherical, pure electron scattering photosphere might look. The double-arrows indicate the polarization direction of a beam, with the size of the arrow

indicating the degree of polarization (not the intensity). Note that (1) the polarization is oriented perpendicular to the radial direction and (2) The light from the photosphere limb is more highly polarized than that from the center. These properties can be understood by looking at the oversimplified diagram on the left of Figure 2.6, showing a unpolarized central source surrounded by a electron scattering shell. Light scattered off the shell will be polarized perpendicular to the scattering plane, which is the plane of the paper in the figure. Edge light has scattered more nearly at 90° and is therefore more highly polarized then the forward scattered central light.

The calculated polarization from a more realistic, power-law density electron scattering atmosphere is shown in Figure 2.7. Because the effective source is now of finite size, the incident radiation field is not completely radial, and thus the edge scattered light is less than 100% polarized. At an impact parameter equal to the photospheric radius, the degree of polarization equals 13%, which is not much different than the value of $\sim 11\%$ that Chandrasekhar (1960) found for a plane parallel atmosphere. At even larger radii, the incident radiation field becomes more dilute and anisotropic; the light scattered toward an observer is therefore of lower intensity and higher polarization. Note that most of the polarized flux from a supernova atmosphere comes from an annulus just above the photospheric radius.

Because observed supernovae are too distant to be resolved, what we actually measure in practice is the Stokes specific intensity integrated over the entire supernova surface. If the projection of the supernova along the line of sight is circularly symmetric, as in Figure 2.8a, the polarization of each emergent specific intensity beam will be exactly canceled by an orthogonal beam one quadrant away. The integrated light from the supernova will therefore be unpolarized. This result is of course obvious from symmetry – because a spherical system has no preferred direction, there is no reason for the polarization to point one way rather than another, and therefore it must be zero.

A non-zero polarization measurement demands some degree of asphericity. For example in the ellipsoidal photosphere of Figure 2.8b, vertically polarized light from the long edge of the photosphere dominates the horizontally polarized light from the short edge. The integrated specific intensity of Figure 2.8b is then partially polarized with $q > 0$ and,

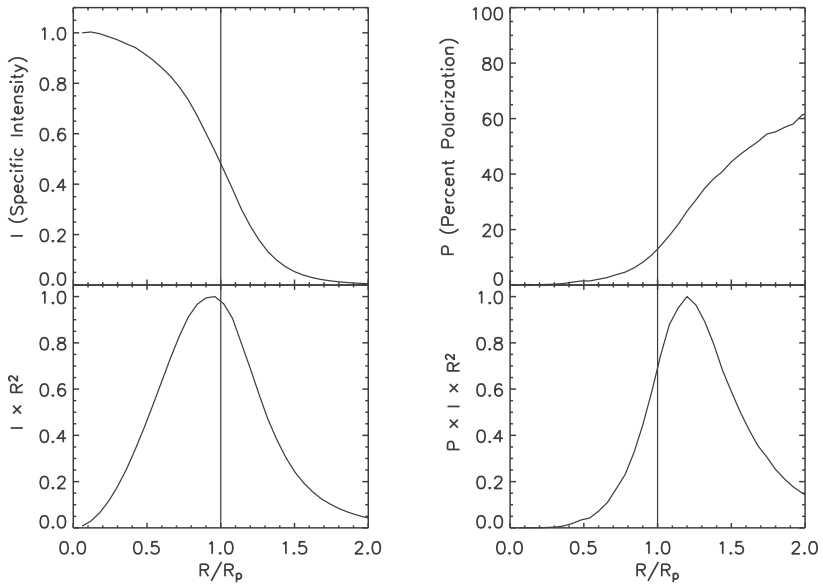

Figure 2.7 The intensity and polarization of light emergent from a spherical electron scattering medium at impact parameter R (in units of the photospheric radius R_p). At larger impact parameter, the radiation field becomes more dilute and anisotropic; the light scattered toward and observer is therefore of lower intensity and higher polarization. In this model, the density structure is a power law ($\rho \propto r^{-7}$), and the radiation source is a sphere placed at $\tau = 3$.

by symmetry, the diagonal polarization u cancels. In general, because an axially symmetric system has only one preferred direction, the polarization necessarily aligns either parallel or perpendicular to the axis of symmetry. The situation in Figures 2.8c and 2.8d is discussed in §2.3.3 below.

2.3.3 The Effect of Lines on the Polarization

A major focus of this thesis is to explore the effect of lines on the polarization of supernovae. Line opacity may have a polarizing effect very similar to electron scattering.

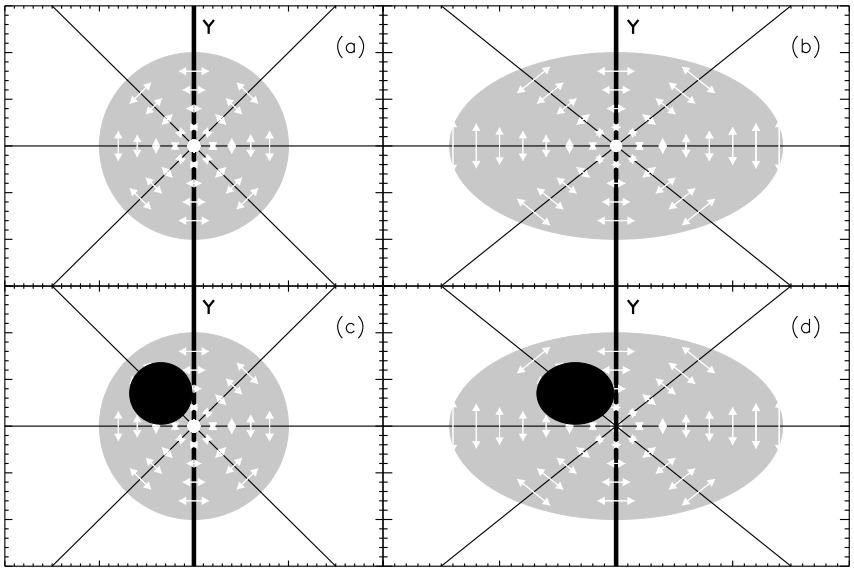

Figure 2.8 Illustrative diagrams of the polarization from a supernova atmosphere.

The effect depends upon the quantum angular momentum values J_l and J_u of the lower and upper levels of the atomic transition. Figure 2.9 illustrates the effect for $J_l = 0$, $J_u = 1$. An incoming photon will excite the atom to one of the three magnetic sublevels. If the atom immediately de-excites back to the ground state, the emitted radiation distribution is dipolar, and the polarization effect is given by the Rayleigh phase matrix, identical to electron scattering.

For other values of J_l and J_u, the effect is in general diluted compared to electron scattering. Hamilton (1947) has shown that the polarizing effect of resonance line scattering can be written as the sum of a dipole and an isotropic contribution. The effect is described

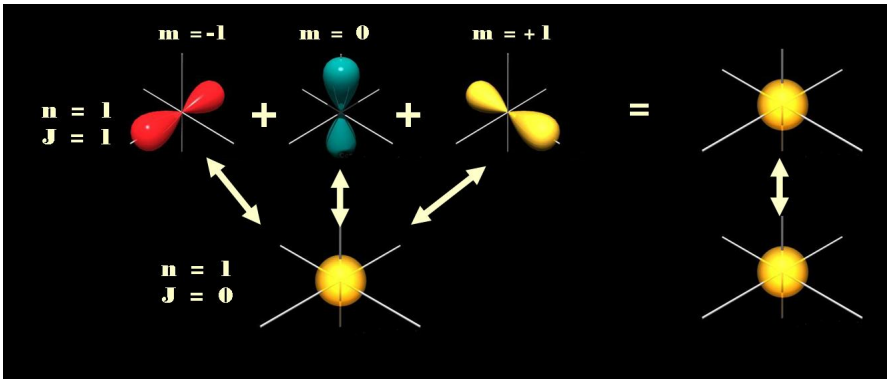

Figure 2.9 Diagram explaining the polarization effect of resonant line scattering. If a photon excites and immediately de-excites from one of the three magnetic sublevel (left), the scattered light is dipolar and polarized as in electron scattering. If, however, collisions redistribute the atom equally over all three states before de-excitation, the resulting state is on average spherically symmetric (right) and the scattered light isotropic and unpolarized.

by the hybrid phase matrix

$$\mathbf{I}_{\text{out}} = \left[W_2 \mathbf{P}(\Theta) + (1 - W_2) \begin{pmatrix} 1 & 0 & 0 \\ 0 & 0 & 0 \\ 0 & 0 & 0 \end{pmatrix} \right] \mathbf{I}_{\text{in}}, \tag{2.22}$$

where $\mathbf{P}(\Theta)$ is the Rayleigh phase matrix (Equation 2.20), while the second matrix is the depolarization matrix. The quantity W_2 is the polarizability factor of the line – it is 0 for a depolarizing line, and 1 for a line that polarizes just like an electron. Hamilton (1947) provides a simple formula for computing W_2 which depends only upon J_l and J_u. Because of the simplicity of this description of line polarization, Equation 2.22 has often been used beyond its scope to calculate the polarizing effect of non-resonance lines (e.g Jeffrey, 1989).

The Hamilton Equation 2.22 for line scattering only holds if collisions are unimportant. If on the other hand the collision time is short compared to the de-excitation time of the atom, collisions will tend to destroy the polarization state of the gas by randomly

redistributing the atom equally over all of the nearly degenerate magnetic sublevels (see Figure 2.9). The average atomic state will therefore be spherically symmetric, and the emitted light isotropic and unpolarized. This is the assumption typically made in models (Höflich et al., 1996; Howell et al., 2001).

Detailed estimates of the critical densities necessary for collisional depolarization in supernova atmospheres have not been attempted. There are, however, two additional reasons supporting the assumption of depolarization in lines: (1) As discussed in detail in §3.3.3, photons will multiple scatter in the resonance region of a line before escaping. Because of the multiple scattering, the radiation field in optically thick lines tends toward isotropy, and hence the scattered light will be unpolarized. (2) The polarizability factor for most lines is less than one, therefore their scattering effect is indeed depolarizing in comparison to electron scattering. This was the finding of Jeffrey (1989) in studying the polarization of the Hα line in ellipsoidal supernova atmospheres.

In this thesis, we will always assume that the light scattered in lines is unpolarized. However, this does not mean that lines necessarily produce a decrease in the degree of polarization in the spectrum. The actual effect will depend sensitively upon the geometry of the line opacity and the electron scattering medium. For example, Figure 2.10 shows the line polarization profile arising in an ellipsoidal atmosphere (McCall, 1984; Jeffrey, 1989). In this geometry, the blueshifted material in front of the photosphere preferentially absorbs lowly polarized central light, such that a greater percentage of highly polarized edge light reaches the observer; this produces a blueshifted *peak* in the polarization spectrum. At lower blueshifts, on the other hand, the line primarily obscures the edge light and leads to a polarization decrease. At redshifted wavelengths, the line does not obscure the photosphere, but will decrease the polarization by emission of unpolarized line light. The resulting polarization feature is often called an *inverted* P-Cygni profile.

While Figure 2.10 artificially separates the atmosphere into "photosphere" and "line opacity," this oversimplification in fact captures some essential features of the line formation, and is very useful in understanding the line polarization profiles arising in supernova atmospheres. For example, suppose the electron-scattering regime is spherical, but

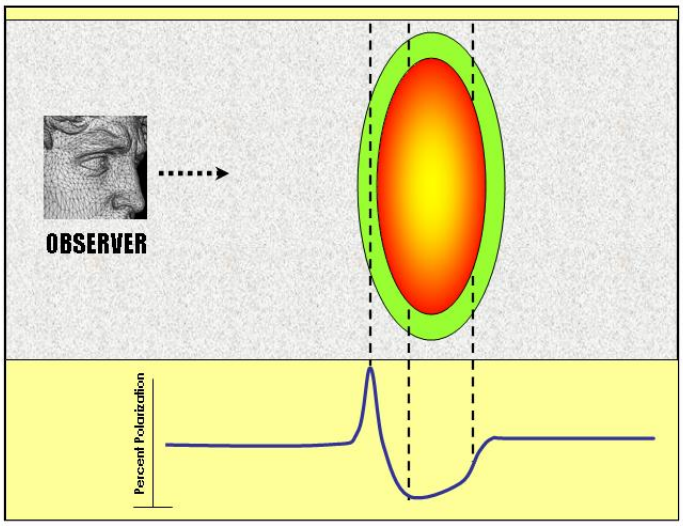

Figure 2.10 Formation of the inverted P-Cygni line polarization profile in an ellipsoidal supernova atmosphere.

the line opacity is confined to an asymmetric clump, as shown in Figure 2.8c. Because the line preferentially obscures light of a particular polarization direction, the cancellation of the polarization of the photospheric light will not be complete. The line thus produces a peak in the polarization spectrum, and a corresponding absorption in the flux spectrum. We call this effect the *partial obscuration line opacity effect* or just *partial obscuration*. As the clump in Figure 2.8c primarily absorbs diagonally polarized light, we expect the polarization peak to have a dominant component in the u-direction.

A non-axially symmetric supernova is shown in Figure 2.8d. The electron scattering medium is ellipsoidal, so the continuum will be polarized in the q direction. The clump of line opacity, which breaks the axial symmetry, preferentially obscures diagonally polarized light, so the line absorption feature will be polarized primarily in the u direction. Thus, the variation of the polarization angle over lines may give information regarding the orientation of different components of the ejecta with respect to the photosphere. This will

be the major focus of our investigations in Chapter 4.

To treat the problem of line polarization correctly requires a solution of the non-local thermodynamic equillbrium (NLTE) rate equations determining the level populations of all the angular momentum sublevels. This is a challenging task which has just recently begun to be tackled (Trujillo Bueno & Manso Sainz, 1999; Trujillo Bueno, 2003). A number of interesting NLTE effects have been explored and found to be important in explaining the polarization spectrum of the Sun (Stenflo & Keller, 1997; Trujillo Bueno et al., 2002). These are, however, beyond the scope of this thesis, and in any case do not appear to be of much importance for the polarization spectra of supernovae. In the extended atmospheres of supernovae, the geometrical obscuration of the photosphere will be the dominate effect.

Chapter 3

Radiative Transfer Methods

In this chapter, we develop methods for solving the 3-D polarized radiative transfer problem in supernova atmospheres. After a very brief description of the fundamental concepts and existing techniques, we turn to Monte Carlo methods, and the specifics of our 3-D supernova code.

Although we call our code a "3-D Monte Carlo" code, in fact the Monte Carlo routine is only one part of a larger code structure that uses both formal and probabilistic methods. We lay out the basic physical assumptions in §3.2. The overall structure of the technique is outlined in §3.3. A few example calculations are given in §3.4.

3.1 Framing of the Problem

3.1.1 The Radiative Transfer Equation

The fundamental quantity in radiative transfer is the specific intensity I_λ, which describes the flow of radiation in a specific direction

$$I_\lambda(\vec{r}, \hat{n}) = \frac{dE_\lambda}{\cos\theta \; dA \; dt \; d\lambda \; d\Omega}. \tag{3.1}$$

Here dE_λ is the energy with wavelength between λ and $\lambda + d\lambda$ flowing through a surface area dA at position $\vec{r}$ in the direction $\hat{n}$ and between times t and $t + dt$. The units of specific

intensity are ergs s^{-1} $Å^{-1}$ cm^{-2} $sterad^{-1}$.

The behavior of the specific intensity along a beam path is governed by the radiative transfer equation

$$\frac{\partial I_\lambda(\vec{r},\hat{n})}{\partial s} = -\alpha_\lambda(I_\lambda - S_\lambda), \tag{3.2}$$

where α_λ is the extinction coefficient (units cm^{-1}) and S_λ is the source function (units of specific intensity). The first term on the right-hand side of Equation 3.2 describes the attenuation of I_λ by absorbing or scattering material along the beam path; the second term represents the enhancement of the intensity by radiation emitted by this same material. For an atmosphere that is in thermal equilibrium, the source function depends on the local temperature only, and is given by the blackbody equation

$$B_\lambda(T) = \frac{2hc^2}{\lambda^5}\frac{1}{e^{hc/\lambda kT} - 1}. \tag{3.3}$$

On the other hand, for an atmosphere that purely scatters radiation, the source function is equal to the mean intensity J_λ, defined by integrating I_λ over all incident directions

$$J_\lambda(\vec{r}) = \frac{1}{4\pi}\oint I_\lambda(\vec{r},\hat{n})\ d\Omega. \tag{3.4}$$

Unlike B_λ, J_λ is not a purely local quantity, as it depends upon the temperature at distant points where the radiation was emitted.

If the transfer Equation 3.2 looks harmless enough, it is only because the notation obscures its complexities. The basic difficulty is that the source function depends upon the incident radiation field. For example, in the pure scattering case $S_\lambda = J_\lambda$ and Equation 3.2 becomes

$$\frac{\partial I_\lambda(\vec{r},\hat{n})}{\partial s} = -\alpha_\lambda I_\lambda + \frac{\alpha_\lambda}{4\pi}\oint I_\lambda(\vec{r},\hat{n})\ d\Omega. \tag{3.5}$$

Thus the equations for I_λ along different directions $\hat{n}$ are coupled together. In the more general case, both S_λ and α_λ depend upon I_λ in a complicated way through the detailed ionization and excitation state of the gas. Then the radiative transfer equation is coupled as well to the equations of statistical equilibrium.

In a traditional radiative transfer calculation, Equation 3.2 is solved numerically for several different beam paths through the atmosphere. The flux observed at wavelength λ is then obtained by integrating I_λ over the stellar surface. We call such approaches *formal integral methods*. Several 1-D codes exist that solve the co-moving radiative transfer equation in an expanding supernova atmosphere, coupled to the full equations of statistical equilibrium (Eastman & Pinto, 1993; Hoflich, 1995; Hauschildt et al., 1997). Such codes necessarily apply rather sophisticated numerical algorithms and require significant computing power.

Generalizing formal solutions of the radiative transfer to include 3-D geometries and polarization poses a formidable challenge. Because of the lack of symmetry, the radiative transfer equation must be solved along a large number of directions $\hat{n}$ to ensure that each point in the atmosphere is properly coupled to every other. While much progress is being made on this front (e.g., Trujillo Bueno, 2003), full 3-D formal solutions for expanding supernova atmospheres appear to be some years away.

3.1.2 The Monte Carlo Approach

The Monte Carlo (MC) approach to radiative transfer has several advantages over traditional formal integral methods. MC codes are intuitive, relatively easy to develop, and less likely to fall victim to subtle numerical errors such as resolution or edge effects (Auer, 2003). Because the method does not rely on any symmetry in the problem, it generalizes readily to 3-D geometries and the inclusion of polarization. Finally, MC codes parallelize almost perfectly, and so can profitably be run on multiprocessor machines.

The historical drawback of MC codes is their computational expense; because the approach is probabilistic, a very large number of packets must be tracked in order to overcome random noise. 1-D MC codes can be effectively run on a single workstation, but 3-D multi-wavelength calculations require the memory and computational power currently only available on supercomputers. Nevertheless, given the favorable scaling, and the continual increase in computing power, the computational inefficiency of MC codes will be increasingly

outweighed by their many advantages.

Monte Carlo approaches have been applied to a wide range of radiative transfer problems, especially multi-dimensional polarization problems (e.g., Daniel, 1980; Code & Whitney, 1995; Wood et al., 1996). The MC code described in Höflich et al. (1996) has been used to calculate the continuum polarization and polarization spectrum of 2-D supernovae (Höflich, 1991; Wang et al., 1997; Howell et al., 2001). In addition, the 1-D MC code of Mazzali & Lucy (1993) has been used in numerous studies of supernova flux spectra (e.g., Mazzali et al., 1995, 2001). The papers of Leon Lucy have been particularly important in developing the MC technique for astrophysical applications (Lucy, 1999a, 2001, 2002, 2003). The new techniques make it feasible for MC codes to eventually match the physical accuracy of formal solutions of the radiative transfer equation.

Monte Carlo Basics

In the MC approach, packets of radiation energy ("photons") are emitted from within the supernova envelope, and tracked through randomized scatterings and absorptions until they escape the atmosphere. Each photon possess a wavelength and polarization (described by a Stokes vector), which are updated at each scattering event. All photons escaping the ejecta in a specific direction are binned in wavelength to construct the spectrum and polarization of the supernova along that line of sight. In addition, we can use tallies of the number of photons passing through individual grid cells to construct estimators of local physical quantities, such as the mean intensity of the radiation field.

The behavior of individual packets in the MC simulation is determined by randomly sampling probability distributions $p(x)$. This is accomplished by finding the value x in the equation

$$z = \int_{x_{min}}^{x} p(x')dx', \tag{3.6}$$

where here and in what follows, the quantity z is a random number chosen from $0 < z < 1$ with uniform distribution.

We describe three ways in which Equation 3.6 may be solved. First, in some cases

it is possible to invert $p(x)$ analytically. To give an important example, the probability of a photon scattering in traveling a distance s is given by $p = 1 - \exp(-\tau)$, where $\tau = \int_0^s \alpha_\lambda ds$ is the optical depth. Inverting $p(\tau)$ gives

$$\int_0^s \alpha_\lambda ds = \tau_r = 1 - \ln(z). \tag{3.7}$$

Thus to determine the distance s a packet travels before scattering, the integral is calculated numerically by taking small steps until the accumulated optical depth along the path reaches τ_r.

In most other situations, it is either impossible or too computationally expensive to invert $p(x)$ analytically. In this case, the rejection method offers an alternative. As an example, suppose we want to emit photons according to a blackbody distribution $B(\lambda)$. After defining the normalized probability function $p(\lambda) = B(\lambda)/\mathrm{MAX}[B(\lambda)]$, a random λ is chosen between the imposed wavelength limits $\lambda_{\min}$ and $\lambda_{\max}$. If $p(\lambda) < z$, this wavelength is selected; otherwise it is rejected and new values of λ and z are selected until the rejection criterion is satisfied.

A final method of sampling discrete probability distributions $p(x_i)$ is the cumulative distribution function (CDF), defined by

$$P(x_i) = \frac{\sum_{x_{\min}}^{x} p(x_i)}{\sum_{x_{\min}}^{x_{\max}} p(x_i)}. \tag{3.8}$$

The function $P(x_i)$ increases monotonically from 0 to 1. To sample the probability function, a random z is chosen and a binary search performed to locate the value x_i where $P(x_i) = z$. For sharply peaked probability functions, the CDF approach is much faster than the rejection method.

3.2 Physical Assumptions

Any astrophysical code must balance the desire for complete physical accuracy with constraints on computing and code development time. In our transfer code we make the assumptions that the atmosphere is (1) in homologous expansion, (2) quasi-static, and

(3) that line transfer can be treated in the Sobolev approximation. Additional physical limitations include the assumption of local thermodynamic equilibrium, and the neglect of special relativity. In future work, we plan to relax each of these assumptions within the basic MC framework.

3.2.1 Homologous Expansion

We assume the velocity structure of the ejecta is given by a homologous (or free) expansion law, $\vec{v}(\vec{r}) = \vec{r}/t_{\rm exp}$, where $t_{\rm exp}$ is the time elapsed since the explosion. Soon after the explosion, the flow of supernova material is highly supersonic and the time scale for sound waves to transfer pressure forces is much longer than the expansion time of the ejecta. In the absence of forces, the location of a gas element is given by $\vec{r} = \vec{v}t_f + \vec{R}_0$, where t_f is the time since free expansion set in and $\vec{R}_0$ is the position of the material when this occurred. Typically free expansion sets in quite early (minutes to hours after the explosion), so that by a few days after the explosion $t_f \approx t_{\rm exp}$ and the ejecta has expanded through a sufficiently large distance that $\vec{R}_0$ can be ignored. Thus even if the explosion is highly asymmetric, the velocity structure will soon evolve to be spherical and homologous.

3.2.2 The Quasi-Static Approximation

Although supernovae are obviously transient phenomena, our calculations only treat "snapshots" of the ejecta frozen in time. This *quasi-static approximation* should be reasonable as long as the photon diffusion time (t_d) is short compared to the expansion time ($t_{\rm exp}$) of the supernova. If this holds, we can track photon packets through a static (rather than evolving) atmospheric grid, although the expansion of the ejecta must still be taken into account in the Doppler shifting of photons.

For a SN Ia at maximum light ($t_{\rm exp} \approx 20$ days), the electron scattering optical depth to the center of the ejecta is about ten, corresponding to a mean free path of $v_p \approx 1000$ km s^{-1}. A photon will on average undergo $\sim \tau_{es}^2 = 100$ scattering events before random walking out of the ejecta and therefore $t_d/t_{\rm exp} = 100 v_p/c \approx 0.3$. The quasi-

static approximation should then be marginally acceptable at maximum light, at least for wavelengths $\lambda > 4000$ Å, where electron scattering dominates the opacity. For photons with wavelengths < 4000 Å, the opacity from numerous iron peak line transitions increases the optical depth by a factor of 10-100. Fortunately, diffusion of the UV photons will be hastened by their absorption/re-emission and fluorescence to longer wavelengths. On the other hand, at early times, say $t_{\rm exp} = 10$ days, $\tau_{es} \approx 40$ and $t_d/t_{\rm exp} = 1.2$. The quasi-static approximation is no longer strictly appropriate, and a time-dependent treatment of the problem is desired.

3.2.3 The Sobolev Approximation

For atmospheres with large velocity gradients such as supernovae, the Sobolev approximation provides a simple and elegant treatment of line transfer (Sobolev, 1947). The basic idea behind the approximation has been mentioned in §2.2.1. Detailed derivations have been given (Mihalas, 1978; Jeffery & Branch, 1990; Castor, 1970), and the major results will be used repeatedly throughout this chapter.

Applying the Sobolev approximation increases both the efficiency and simplicity of a MC code, as (1) photon packets only interact with lines at unique, easily calculable points in the atmosphere, and (2) the transfer within a line can be treated analytically. Each photon/line interaction line can therefore be treated as a single MC event, with no need to explicitly follow the hundreds of multiple scatterings a photon may experience before escaping an optically thick line. As a result, the total number of photon/line interactions depends only upon the wavelength spacing of strong lines, with no regard to how optically thick the lines actually are. This is an important reason why Monte Carlo approaches – notoriously inefficient in high opacity regimes – are not necessarily doomed to failure in the heavily line blanketed atmospheres of supernovae.

For the Sobolev approximation to be valid, all relevant physical variables must remain fairly constant over a line resonance region. This will be true whenever the intrinsic width of a line (given by the Doppler velocity v_d) is much less than the scale height v_s over

which the atmospheric properties change. In supernova atmospheres, $v_d \lesssim 10$ km s^{-1} and $v_s \approx 1000$ km s^{-1}, therefore $v_d/v_s \lesssim 0.01$. Olson (1982) has shown that for ratios $v_d/v_s < 0.1$, the Sobolev approximation holds to a high degree of accuracy. Formal inaccuracy may occur for atmospheres with numerous small scale structures (i.e small v_s), or for very optically thick lines where the Lorentz wings become important.

One additional potential pitfall for the Sobolev approximation has been emphasized by Baron et al. (1996a). The Sobolev formalism is derived assuming that each line transition is isolated in wavelength from all others. In reality, the UV wavelengths are densely packed with overlapping lines, such that more than 100 lines may fall within a single Doppler width. Nevertheless, Eastman & Pinto (1993) have found that in practice the error thus incurred on the emergent spectra is very small. This is perhaps not surprising, as the vast majority of the millions of lines in supernova atmospheres will be exceedingly weak – typically only a few 10,000s will have optical depths larger than 0.5. The average spacing of such strong lines ($\sim$100 km s^{-1}) is much greater than a Doppler width. Because strong lines dominate the radiative transfer, treating all lines as non-overlapping may not lead to any serious error.

3.3 Structure of the Radiative Transfer Code

Our 3-D radiative transfer code was designed to calculate the optical properties of multi-dimensional supernova explosion models. The code takes as input the density, composition, and amount of ^{56}Ni at every point on a 3-D Cartesian grid. The time since explosion $t_{\rm exp}$, total supernova luminosity L_0, and an emission temperature T_{bb} must be specified as free parameters.

The outline of the code structure is diagrammed in Figure 3.1. The essential difficulty of the transfer problem is this: the opacities needed for the photon MC transfer depend upon the atmospheric temperatures, but these temperatures depend upon the photon heating and cooling rates, which will only be known *after* the MC transfer has been completed. Therefore we need an iterative approach to handle the interdependence. The

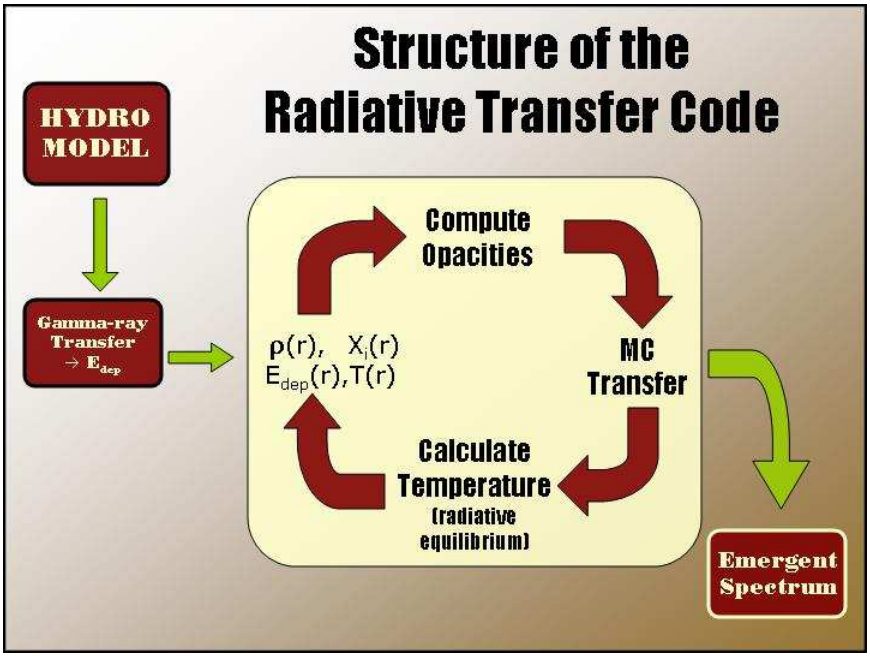

Figure 3.1 Structure of the radiation transfer code.

procedure is as follows:

1. Using a 3-D gamma-ray transfer routine, we determine where energy from the decay of radioactive ^{56}Ni and ^{56}Co is deposited in the supernova envelope (§3.3.1). This serves as the source geometry of the emitted optical photon packets.

2. The opacities at all wavelengths for each cell are computed assuming local thermodynamic equilibrium (§3.3.2). Because the atmospheric temperature structure is not initially known, we start with a reasonable guess, to be refined iteratively.

3. The MC transfer of optical photon packets is run, which provides the rate of photon absorption in each cell (§3.3.3).

4. A new temperature is determined for each cell (§3.3.4) by setting equal the rate of

photon absorption to the rate of thermal photon emission.

5. The temperature structure calculated in step (4) will differ from that used initially to compute the opacities in step (2). Thus, to bring about consistency, we recompute the opacities and return to step (3), iterating this procedure until the temperature and opacities change negligibly from one iteration to the next.

6. Once the atmosphere has converged, the synthetic flux and polarization spectra are generated during the MC transfer by collecting all photons escaping the atmosphere along a certain line of sight.

We now proceed to discuss each step in greater detail.

3.3.1 Energy Deposition

The Radiation Source Geometry

The first issue in any MC code is to specify the source of photon packets. In spherical MC codes, the source is usually taken to be an extended, spherical inner boundary surface (the "inner core"). Photon packets are emitted isotropically from the core surface and any packet backscattered onto the core is "absorbed" and removed from the calculation. The radius of the core becomes a free parameter of the simulation, but it is hoped that if the core is placed deep enough in the ejecta, the emergent spectra will be rather insensitive to its exact location.

While we will occasionally apply a spherical inner source, such a prescription is generally not appropriate for 3-D models. Most critically, the polarization depends upon the isotropy of the radiation field, and is therefore as sensitive to the shape and distribution of the radiation source as it is to the geometry of the scattering medium. Fortunately, a better representation of the 3-D source geometry can be given for the case where the luminosity is dominated by the decay of radioactive isotopes. In Type I supernovae, the energy is released in the decay chain $^{56}\mathrm{Ni} \rightarrow {}^{56}\mathrm{Co} \rightarrow {}^{56}\mathrm{Fe}$, with almost all of the decay energy emerging as ~ 1 MeV gamma-rays. The emitted gamma-rays will propagate some

distance before depositing their energy in the ejecta. The deposited energy is assumed to be thermalized, to eventually emerge as optical/UV photons.

We follow the propagation of gamma-rays using a MC routine similar to those described in Ambwani & Sutherland (1988), Swartz et al. (1995), and Hoeflich et al. (1994). This gamma-ray Monte-Carlo (GRMC) procedure is conceptually separated from the main MC transfer routine for the optical/UV photons (§3.3.3). Obviously the two routines could be integrated, such that each absorbed gamma-ray photon packet was immediately re-emitted as a thermal optical photon packet of equal energy. However, because the gamma-ray opacities do not depend upon temperature, there is no need to repeat the GRMC calculation for each temperature structure iteration. Instead, we calculate and store the rate of gamma-ray energy deposition once at the beginning of a run.

The instantaneous rate of gamma-ray energy deposition largely determines the total luminosity of the supernova. If V_i is the volume of cell i and $\dot{E}^i_{\rm dep}$ is the rate of energy deposition in that cell, then we write the total optical luminosity L_0 as

$$L_0 = \eta \sum_i \dot{E}^i_{\rm dep} V_i, \tag{3.9}$$

were η is a free "fudge-factor" parameter of order unity, that is used to account for the time-dependent effect of diffusive radiation stored in the supernova envelope. For the epochs after maximum light $\eta \gtrsim 1$ to account for photons trapped from earlier epochs. In this context, the quasi-static approximation amounts to assuming that the diffuse radiation field follows the current deposition geometry. As the "old" photons in fact came from the same ^{56}Ni source, the assumption does not seem totally unrealistic.

In supernovae such as SNe IIP where the luminosity is mostly powered by diffusion rather than radioactivity, one really needs to solve the time-dependent transfer problem. Whereas in a spherical SNe IIP model one can simply apply the diffusion approximation at depth, in a 3-D model there is no way of knowing the inner surface boundary conditions except by following the evolution of the temperature structure starting from the explosion itself. In the absence of this, one can only make an *ad-hoc* guess as to the source geometry.

Gamma-Ray Transfer Calculations

A ^{56}Ni nucleus decays by electron capture to an excited state of ^{56}Co which de-excites to the ground state by emission of several (on average about 3) gamma-rays. ^{56}Co in turn decays to ^{56}Fe by electron capture or by positron emission plus electron capture. The energy from radioactive decay per unit time per unit volume is given by

$$\dot{E}_{\rm rad}(t,\vec{r}) = \bar{E}_{\rm Ni} N_{\rm Ni}(\vec{r}) \frac{e^{-t/\tau_{\rm Ni}}}{\tau_{\rm Ni}} + \bar{E}_{\rm Co} N_{\rm Ni}(\vec{r}) \left(\frac{e^{-t/\tau_{\rm Ni}}}{\tau_{\rm Ni}} - \frac{e^{-t/\tau_{\rm Ni}}}{\tau_{\rm Ni}} \right), \tag{3.10}$$

where $\tau_{\rm Ni} = 8.8$ days and $\tau_{\rm Co} = 113.6$ days are the decay times, and $\bar{E}_{\rm Ni} = 1.71$ MeV and $\bar{E}_{\rm Co} = 3.76$ MeV the average energy per decay of ^{56}Ni and ^{56}Co, respectively. $N_{\rm Ni}$ is the number density of ^{56}Ni immediately following the explosion. The emitted gamma-rays emerge in one of several possible lines, all around 1 MeV. About 3.5% of the energy from ^{56}Co decay emerges as the kinetic energy of emitted positrons. We make the usual assumption that the charged positrons are trapped by residual magnetic fields, and deposit their kinetic energy locally in the ejecta before annihilating to create two 511 keV photons.

The gamma-ray packets are all initially assigned to have equal energy E_γ, given by

$$E_\gamma = \frac{\Delta T}{N_\gamma} L_\gamma, \tag{3.11}$$

where L_γ is the total energy per second released in gamma-rays, N_γ is the total number of packets used in the simulation, and ΔT is the time step covered by the MC simulation (as it cancels out of all expressions used, ΔT does not need to be explicitly specified). Because equal energy packets are used, packets of different wavelengths represent a different number of photons.

The important opacities for gamma-rays are Compton scattering and photoelectric absorption (the additional opacity due to pair-production is typically very small and will be ignored). Because the gamma-ray energies are much greater than the atomic binding energies, all electrons in an atom (bound and free) contribute to the Compton opacity

$$\alpha_{\rm c} = \sigma_{\rm T} N K(x) \sum_i X_i Z_i, \tag{3.12}$$

where $x = E/m_e c^2$, $\sigma_T = 0.6 \times 10^{-24}$ is the Thomson cross-section, and N is the total number density. The sum runs over all elements with abundance fraction by number X_i and atomic number Z_i. The dimensionless quantity $K(x)$ is the Klein-Nishina correction to the cross-section

$$K(x) = \frac{3}{4}\left[\frac{1+x}{x^3}\left(\frac{2x(1+x)}{1+2x} - \ln(1+2x)\right) + \frac{1}{2x}\ln(1+2x) - \frac{1+3x}{(1+2x)^2}\right]. \tag{3.13}$$

$K(x)$ is always less than one and decreases with increasing x.

Typically Compton opacity dominates for $E \gtrsim 50$ keV, while photoelectric absorption dominates for lower energies. The photoelectric extinction coefficient is dominated by the two K-shell electrons, and is calculated in the Born approximation

$$\alpha_{\rm p} = \sigma_{\rm T}\alpha^4 8\sqrt{2}x^{-7/2}N\sum_i Z_i^5 X_i, \tag{3.14}$$

where α is the fine-structure constant.

Gamma-ray packets are moved through the atmosphere in small steps of velocity length Δv (physical distance $\Delta v\ t_{\rm exp}$). The optical depth along the path is integrated until it reaches a value randomly chosen by Equation 3.7. At this point an interaction occurs and another random number z is chosen to determine the subsequent packet fate. If $z < \alpha_{\rm c}/(\alpha_{\rm c} + \alpha_{\rm p})$ the gamma-ray is Compton scattered, otherwise it is photo-absorbed.

In a Compton scattering, a new direction for the gamma-ray is sampled from the anisotropic differential cross-section

$$\frac{d\sigma}{d\Omega} = \frac{3\sigma_T}{16\pi}f(x,\Theta)^2\left(f(x,\Theta) + f(x,\Theta)^{-1} - \sin^2\Theta\right), \tag{3.15}$$

where Θ is the angle between incoming and outgoing gamma-ray directions and $f(x,\Theta)$ is the ratio of incoming to outgoing gamma-ray energy,

$$f(x,\Theta) = \frac{E_{in}}{E_{out}} = \frac{1}{1+x(1-\cos\Theta)}. \tag{3.16}$$

The average energy lost in an interaction is given by

$$F(x) = 1 - \frac{1}{4\pi}\oint d\mu d\phi \frac{d\sigma}{d\Omega}f(x,\mu). \tag{3.17}$$

For a 1 MeV gamma-ray, $F(x) \approx 0.6$. Thus a gamma-ray loses almost all of its energy after just a few Compton scatterings, after which it will be destroyed by photo-absorption. The lost gamma-ray energy becomes the kinetic energy of the fast, scattered electrons, which are quickly thermalized locally through electron-electron collisions.

In previous GRMC codes, the rate of energy deposition $\dot{E}^i_{\rm dep}$ is estimated by tallying up the gamma-ray energy lost during each scattering or absorption in cell i. In this case, enough packets must be used such that many interactions occur in *every* cell. On a 3-D grid, this requires a very large number of packets, especially at later times when gamma-rays begin to escape the atmosphere and interaction events become infrequent. Fortunately, following ideas in Lucy (1999a), we can derive a better estimator of $\dot{E}^i_{\rm dep}$ by considering the analytic expression for the absorbed energy,

$$\dot{E}^i_{\rm dep} = \oint \int \alpha_{\rm abs} I_\lambda d\lambda d\Omega = 4\pi \int J_\lambda [\alpha_{\rm c}(x) F(x) + \alpha_{\rm p}(x)] d\lambda. \tag{3.18}$$

The mean intensity of the radiation field J_λ can always be better estimated than $\dot{E}_{\rm dep}$ itself, because every packet passing through a cell contributes, regardless of whether an interaction occurs. To derive the needed estimator, we begin with the relationship between J_λ and the monochromatic energy density u_λ (Mihalas, 1978),

$$u_\lambda d\lambda = \frac{4\pi}{c} J_\lambda d\lambda. \tag{3.19}$$

When a packet possessing a fraction E/E_γ of its initial energy takes a step of size Δv in a cell, its contribution to u_λ is

$$du_\lambda = \frac{E_\gamma}{V_i} \left(\frac{E}{E_\gamma} \right) \left(\frac{\delta t}{\Delta T} \right) \frac{1}{d\lambda}, \tag{3.20}$$

where $\delta t = \Delta v \; t_{\rm exp}/c$ is the time taken for the step. The size of the wavelength bin $d\lambda$ does not need to be specified, as we integrate over wavelength in Equation 3.18 anyway, giving finally

$$\dot{E}^i_{\rm dep} = \frac{L_\gamma}{N_\gamma V_c} (\Delta v \; t_{\rm exp}) \sum_j \frac{E}{E_\gamma} \Big[\alpha_{\rm c}(x) F(x) + \alpha_{\rm p}(x) \Big], \tag{3.21}$$

where the sum runs over every packet step that occurs inside the cell.

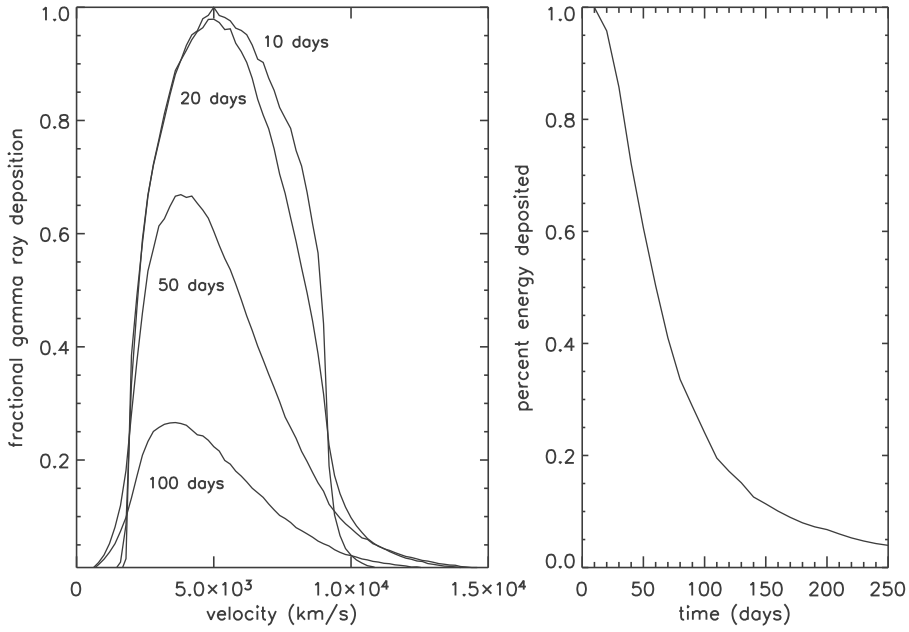

Figure 3.2 Gamma-ray energy deposition for a spherical SN Ia at different times. Left: The distribution of energy deposition as a function of velocity. Right: The fraction of gamma-ray deposited in the ejecta as a function of time.

Figure 3.2 shows some results from a GRMC calculation. Here the atmosphere is a spherical SN Ia with an exponential density profile and ^{56}Ni located between 2000 and 9000 km s^{-1}. At early times ($t_{\rm exp} \lesssim 20$ days) essentially all the gamma-rays are trapped locally. At later times the gamma-rays begin to escape, and the energy deposition spreads into the outer layers.

Escaping gamma-ray packets can be collected to produce the theoretical gamma-ray spectrum of the supernova; an example is shown in Figure 3.3. Gamma-ray spectra are potentially very powerful probes of the geometry and composition of the ejecta (Hungerford et al., 2003; Höflich, 2002). In fact, the gamma-ray lines detected in SN 1987A have been used to infer the presence of large-scale mixing of ^{56}Ni into the outer ejecta layers

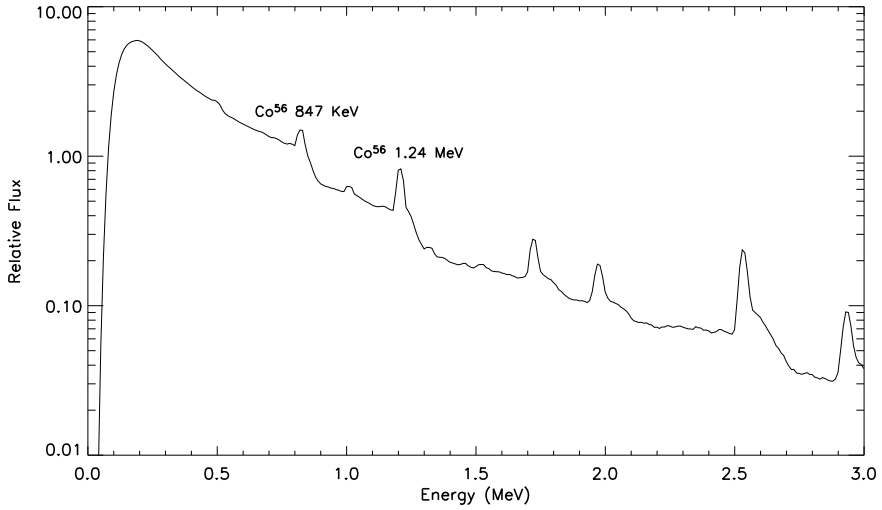

Figure 3.3 Gamma-ray spectrum of a spherical SN Ia near optical maximum light.

(Sutherland et al., 1988). Unfortunately, the large distance to most supernovae make such observations difficult, and so far SN 1987A is the only supernova for which there has been a clear gamma-ray detection.

3.3.2 Opacities

At optical wavelengths, the important opacities in supernovae are electron scattering and bound-bound line transitions and, to a lesser extent, bound-free and free-free opacities. The opacity depends upon the ionization and excitation state of the gas. When collisions dominate the atomic transition rates, the atmosphere is in local thermodynamic equilibrium (LTE). In this case the atomic level populations follow the Saha-Boltzmann equations and the opacity is a function only of the local density, composition, and temperature: $\alpha_\lambda = \alpha_\lambda(\rho, X_i, T)$. More generally, one most also take into account radiative excitation/ionization by optical photons as well as collisions with the fast non-thermal electrons created in the Compton scattering of gamma-rays. In this case of non-local thermodynamic equilibrium (NLTE), the opacities also depend upon J_λ and $\dot{E}^i_{\rm dep}$.

In the calculations of this thesis, we always assume LTE. Unfortunately, the densities in rarefied supernova atmospheres are not high enough for the conditions of LTE to be met. Nevertheless, NLTE effects should for the most part cause quantitative, not qualitative differences in the emergent spectra, and will not obscure the primarily geometrical effects we are interested in exploring. In SN Ia atmospheres, the deviation from LTE is in fact found to be small (Baron et al., 1996b; Pinto & Eastman, 2000b); however, in SN II atmospheres, NLTE corrections for hydrogen can significantly affect the entire atmospheric structure. In the future, a solution to the NLTE rate equations for selected species will be incorporated into the MC approach (see Li & McCray, 1993; Zhang & Wang, 1996).

In LTE, the number density $N_{i,j}$ of element i in ionization stage j is given by the Saha formula

$$\frac{N_{i,j}}{N_{i,j+1}} = \left(\frac{2.0hm_e}{kT}\right)^{1.5} \frac{z_j}{z_{j+1}} N_e \exp(-\Phi/kT), \tag{3.22}$$

where z is the partition function and Φ is the ionization energy. The electron density N_e is determined from the charge conservation equation:

$$\sum_i \sum_j j N_{i,j} = N_e. \tag{3.23}$$

This is a non-linear equation for N_e, which is easily solved with standard numerical techniques. With the ionization known, the population density $N_{i,j,k}$ of a level k is given by the Boltzmann equation

$$N_{i,j,k} = N_{i,j} \frac{g_k \exp(-\chi_k/kT)}{\sum_m g_m \exp(-\chi_m/kT)}, \tag{3.24}$$

where χ_k is the excitation energy and g_k the statistical weight of level k.

The extinction coefficient due to electron scattering is simply $\alpha_{es} = N_e \sigma_T$, while the extinction coefficient for a bound-bound line transition is written

$$\alpha_{bb} = K_\lambda \phi(\lambda). \tag{3.25}$$

Here K is the integrated line strength, which depends upon N_l, the number density of atoms in the lower level of the transition

$$K_\lambda = \left(\frac{\pi e^2}{m_e c}\right) f N_l (\lambda_0^2/c), \left(1 - \frac{g_1}{g_2} e^{-h\nu/kT}\right), \tag{3.26}$$

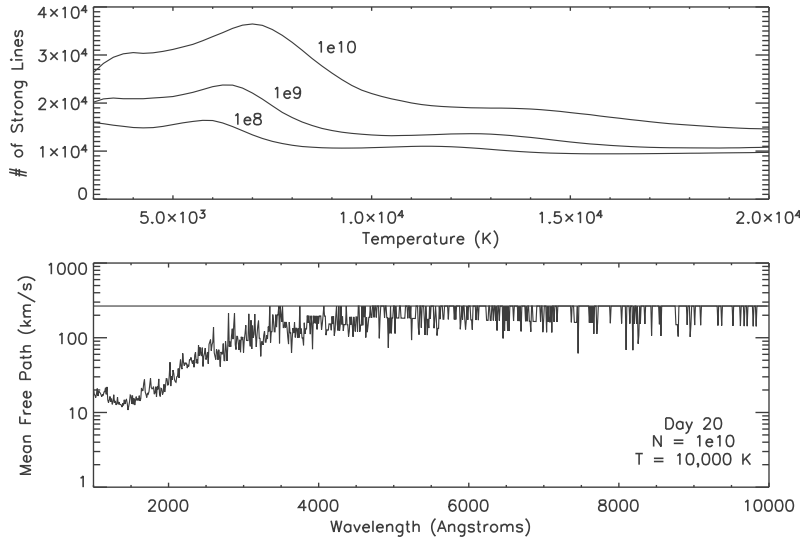

Figure 3.4 Opacities in a SN Ia atmosphere near maximum light. Top: The number of strong lines between 1000 Å and 10,000 Å versus temperature for various number densities (marked on the figure). Bottom: The photon mean free path (in km/s). Lines dominate the opacity blueward of 4000 Å, while electron scattering (straight solid line) dominates redward.

where f is the oscillator strength of the transition and λ_0 the line center wavelength. The last term in parentheses is the correction for stimulated emission evaluated in LTE.

As we will see in §3.3.3, the quantity that is needed in the MC transfer is the line Sobolev optical depth τ,

$$\tau = \frac{K_\lambda c t_{\rm exp}}{\lambda_0}. \tag{3.27}$$

This gives the total optical depth traversed as a photon redshifts completely through a line. Note that Equation 3.27 only holds for atmospheres in homologous expansion; for other velocity laws τ will depend upon the direction the photon is traveling.

Figure 3.4 shows the mean free path of a photon as a function of wavelength for the conditions expected in the inner layers of a SN Ia near maximum light. The bound-bound

opacity strongly dominates in the blue and UV ($\lambda \lesssim 4000$ Å), where there is a high density of lines from iron-peak elements. At these wavelengths, the mean free path is basically given by the velocity spacing of strong lines. Because bound-free and free-free opacities (not shown in the figure) are typically small compared to bound-bound and electron scattering, we will ignore them in the present calculations.

3.3.3 Monte Carlo Radiative Transfer

With the opacities and source geometry determined, we can begin the main optical photon MC routine. The optical photon packets used in our MC simulation are monochromatic, *equal energy* packets. Every packet has energy E_p and represents a collection of $N_p = E_p\lambda/hc$ photons of wavelength λ. The benefit of using equal energy, rather than equal photon number packets, has been emphasized by Lucy (1999a). In the course of the MC simulation, a packet may get absorbed and immediately remitted at a different wavelength. Using equal energy packets assures that energy is conserved in this interaction and thus the radiation field is naturally divergenceless at all points. This allows for a rapid convergence to the correct temperature structure when the condition of radiative equilibrium is imposed (§3.3.4).

When no inner boundary surface is used, every photon packet that is emitted somewhere in the atmosphere eventually escapes, although perhaps after experiencing several absorption/re-emission events. If we use N_p packets in our simulation, the energy E_p of each packet is

$$L_0 = N_p E_p / \Delta T. \tag{3.28}$$

Photon packets are emitted from cells throughout the atmosphere, with the probability of a packet being emitted from cell i given by

$$p_i = \frac{\dot{E}^i_{\rm dep}}{\sum_i \dot{E}^i_{\rm dep}}. \tag{3.29}$$

Equation 3.29 is sampled using the cummulative distribution function approach; within the cell, the packet emission point is determined by uniformly sampling the cell volume. The

emission of the photon is isotropic in the local frame, so the direction angles $\mu = \cos\theta$ and ϕ are chosen by

$$\mu = 1 - 2z_1, \tag{3.30}$$

$$\phi = 2\pi z_2, \tag{3.31}$$

where z_1 and z_2 are random numbers. Because the detailed NLTE source function of the material is not calculated, the packet wavelengths are sampled from a blackbody distribution with characteristic temperature T_{bb}. We choose T_{bb} so as to reproduce the continuum in the red end of the observed spectrum; the blue end of the spectrum shows very little dependence on T_{bb}, as packets with $\lambda \lesssim 5000$ Å are absorbed and re-emitted in lines.

Packets are moved in small velocity steps Δv, corresponding to a physical distance $\Delta v\ t_{\rm exp}$. Ideally Δv will be chosen smaller than both the photon mean free path and the cell size of the atmospheric grid. The continuum optical depth is integrated along the packet path until it exceeds a randomly chosen value τ_r (Equation 3.7), at which point a scattering occurs. If electron scattering is considered to be isotropic, a new packet direction is chosen using Equations 3.31. However, in the next section, we discuss how the anisotropic redistribution of electron scattering becomes important when polarization is considered.

In taking a step, the wavelength of the photon packet is also redshifted with respect to the local co-moving frame by an amount $\Delta\lambda/\lambda = \Delta v/c$. A photon comes into resonance with a line when its co-moving wavelength redshifts to the line center wavelength. At this point, the probability of the photon interacting with the line is $1 - \exp(-\tau)$, where τ is the Sobolev optical depth (Equation 3.27). If an interaction does occur, the photon is reprocessed according to the local line source function. In our calculations we use an equivalent two-level atom (ETLA) formulation for the source function

$$S_\lambda = (1 - \epsilon)\bar{J}_\lambda + \epsilon B_\lambda(T). \tag{3.32}$$

This function includes both the possibility of line scattering (first term on the right-hand side) and absorption/re-emission (second term). The dimensionless quantity ϵ is the probability of absorption (i.e., thermalization) in the line. In principle, each line transition has

a different value of ϵ that can be calculated from the atomic transition rates. However, for simplicity we make ϵ a free parameter which is the same for all lines. Detailed NLTE calculations find that a value of $\epsilon \approx 0.01 - 0.1$ is appropriate for supernova atmospheres (Baron et al., 1996b; Höflich et al., 1996; Nugent et al., 1997).

One complication in line interactions is that photons multiply scatter in optically thick lines before redshifting past them. On average, a photon scatters $1/\beta$ times, where the escape probability β is given by the Sobolev formalism

$$\beta = \frac{1 - e^{-\tau}}{\tau}. \tag{3.33}$$

Because of this trapping effect, the mean intensity $\bar{J}_\lambda$ appearing in Equation 3.32 can be thought of as containing two terms,

$$\bar{J}_\lambda = \bar{J}_\lambda^{\rm ext} + \bar{J}_\lambda^{\rm ms}, \tag{3.34}$$

where $\bar{J}_\lambda^{\rm ext}$ represents external radiation impinging on the line, while $\bar{J}_\lambda^{\rm ms}$ represents trapped radiation multiply scattering in the resonance region. Instead of having to consider the multiple scattering explicitly, the Sobolev formalism allows us to solve analytically for S_λ in terms of $\bar{J}_\lambda^{\rm ext}$ only,

$$S_\lambda = (1 - \bar{\epsilon})\bar{J_\lambda^{ext}} + \bar{\epsilon} B_\lambda(T), \tag{3.35}$$

where

$$\bar{\epsilon} = \frac{\epsilon}{\epsilon + (1 - \epsilon)\beta}. \tag{3.36}$$

The effective probability of thermalization in a line is thus $\bar{\epsilon}$, *not* ϵ. For optically thin lines $\bar{\epsilon} \approx \epsilon$ but for very optically thick lines $\bar{\epsilon} \to 1$. As expected, the multiple line scattering increases the probability that a photon will be thermalized.

To determine the fate of a interacting photon, we choose a random number z. If $z < \bar{\epsilon}$ the photon is absorbed, otherwise it is scattered. If scattered, the photon is redirected isotropically but its co-moving wavelength remains unchanged. If absorbed, the packet will be similarly redirected, but will be remitted at a different wavelength. Because line opacity

is the only absorptive opacity used in the calculation, the packet will be remitted in another line. The thermal line emissivity of line i with wavelength λ_i is

$$\eta_i = \frac{\lambda_i}{ct}(1 - e^{-\tau_i})\bar{\epsilon}B(T, \lambda_i). \tag{3.37}$$

A new packet wavelength is chosen by sampling η_i using the CDF method. Note that while the packet wavelength changes in this interaction, the total packet energy remains unchanged. Thus the rate of absorption will naturally balance the rate of emission at all points in the atmosphere.

In using an ETLA source function (Equation 3.32), we formally neglect the possibility of line fluorescence. This is actually a very important process in supernovae, allowing UV photons to more easily escape the atmosphere by fluorescing to longer wavelengths (Pinto & Eastman, 2000a). Our parameterized ETLA accomplishes rather the same effect through the absorption and re-emission of packets; however, fluorescence can be treated more exactly using a first-order branching procedure (Lucy, 1999b): a packet that excites an atom to level i will be re-emitted by de-excitation to level j by sampling the probability function

$$p_{ij} = \frac{A_{ij}\beta_{ij}}{\sum_k A_{ik}\beta_{ik}}, \tag{3.38}$$

where A_{ij} is the Einstein spontaneous decay coefficient and β_{ij} the escape probability of the transition $i \rightarrow j$. This procedure can be improved to include the effect of atoms cascading down several transitions, such that the exact NLTE source function is reproduced (Lucy, 2003). For the present, however, we will not apply any branching methods.

Polarization Calculations

The treatment of polarization requires only small modifications to the MC code. Each photon packet is now assigned a Stokes vector which describes the intensity of light along different axes. In choosing a polarization reference axis for a packet moving in direction $\vec{D}$, we use the following convention: consider the plane defined by $\vec{D}$ and the z-axis; the reference axis is chosen to lie in this plane, perpendicular to $\vec{D}$. To transform the Stokes

vector to another reference axis rotated by an angle ψ, one applies the rotation matrix (Chandrasekhar, 1960)

$$R(\psi) = \begin{pmatrix} 1 & 0 & 0 \\ 0 & \cos 2\psi & \sin 2\psi \\ 0 & -\sin 2\psi & \cos 2\psi \end{pmatrix}. \tag{3.39}$$

Photon packets are initially emitted unpolarized and with their Stokes vector normalized to unity: $\mathbf{I} = (1, 0, 0)$. The effect of an electron scattering on the Stokes vector is described by the Rayleigh phase matrix; however, the simple matrix given in Equation 2.20 only applies when the Stokes vectors are referred to the plane of scattering. The effect on a packet Stokes vector is actually given by

$$S_{\rm out} = R(\pi - i_2)P(\Theta)R(i_1)S_{\rm in}. \tag{3.40}$$

The rotation matrix $R(i)$ rotates the incoming packet Stokes vector onto the scattering plane, while $R(\pi - i_2)$ rotates the outgoing packet Stokes vector back into our conventional reference axis. The rotation angles i_1 and i_2 can be determined from the geometry, however Chandrasekhar (1960) provides a useful expression for Equation 3.40 in terms of the incoming and outgoing packet direction angles; as it is quite long, we do not repeat it here.

When polarization is taken into account, the total intensity of radiation scattered by an electron is not isotropic, but depends upon the incoming polarization (Code & Whitney, 1995):

$$I_{\rm out} = \frac{1}{2}(1 + \cos^2\Theta)I_{\rm in} + \frac{1}{2}(1 - \cos^2\Theta)\cos 2i_1 Q_{\rm in} + \frac{1}{2}(1 - \cos^2\Theta)\sin 2i_1 U_{\rm in}. \tag{3.41}$$

After each scatter we choose new direction angles by sampling the anisotropic redistribution Equation 3.41; the total intensity of the scattered packet Stokes vector is thus always set to unity. An alternative approach would be to scatter packets isotropically, but re-weight the total intensity according to Equation 3.41. This simpler approach, however, is found to be unstable for problems with large optical depths – after a large number of scatters, the intensity of most packets tends to zero, and the radiation becomes concentrated in a small number of very high intensity packets.

As discussed in §2.3.3, we assume line scattered light is unpolarized, so we set $\mathbf{I} = (1, 0, 0)$ after every line interaction.

3.3.4 Calculating the Temperature Structure

We have seen that the temperature of the atmosphere is essential in determining the opacity and emissivity of the supernova material. Here we describe how the temperature can be calculated self-consistently using an iterative approach that imposes radiative equilibrium. The technique for calculating radiative equilibrium in a MC code was first developed by Lucy (1999a) for static, plane-parallel atmospheres. Here we generalize the formalism for 3-D atmospheres in rapid expansion under the Sobolev approximation.

The evolution of the energy E in a volume V is governed by first law of thermodynamics,

$$\frac{\partial E}{\partial t} = V(\dot{A}_{\rm ph} - \dot{E}_{\rm ph} + \dot{E}_{\rm dep}) - P\frac{\partial V}{\partial t}, \tag{3.42}$$

where $\dot{A}_{\rm ph}$ is the optical/UV photon energy absorbed per unit time per unit volume, $\dot{E}_{\rm ph}$ is the corresponding photon energy emitted, and $\dot{E}_{\rm dep}$ is the rate of heating from the decay of radioactive isotopes (all quantities in ergs s^{-1} cm^{-3}). The $P\frac{\partial V}{\partial t}$ term represents the rate of cooling by expansion. As long as the photon diffusion time is significantly less than the expansion time, a steady state will be reached whereby the time derivatives in Equation 3.42 can be ignored. Conceptually, the photons zip around the ejecta and establish the temperature structure before there has been time for significant expansion. Thus, in this quasi-static approximation discussed in §3.2.2, Equation 3.42 becomes

$$\dot{A}_{\rm ph} - \dot{E}_{\rm ph} + \dot{E}_{\rm dep} = 0. \tag{3.43}$$

Actually, the $P\frac{\partial V}{\partial t}$ term can be kept as well without increased difficulty, but we ignore it for now. Equation 3.43 says that at each point in the atmosphere, cooling by photon emission precisely balances the heating from photon absorption plus gamma-ray deposition. Equation 3.43 is commonly called the equation of *radiative equilibrium* (although, strictly speaking, radiative equilibrium requires that $\dot{E}_{\rm dep} = 0$ as well, but we retain the moniker anyway).

Deriving the Equation of Radiative Equilibrium

Because $\dot{E}_{\rm ph}$ depends upon temperature through the Planck function B_λ, Equation 3.43 implicitly determines the temperature at each point in the atmosphere when the other two quantities are known. We now make this temperature dependence explicit. As previously discussed (§3.3.1), it is more efficient to estimate $\dot{A}_{\rm ph}$ from the mean intensity of the radiation field, rather than counting the number of absorbed packets (which may be small if the absorptive opacity is small). The absorption and emission rates can be determined by integrating the radiative transfer Equation 3.2 over wavelength and angle,

$$\dot{A}_{\rm ph} = \oint \int_0^\infty d\lambda d\Omega \alpha_\lambda I_\lambda, \tag{3.44}$$

$$\dot{E}_{\rm ph} = \oint \int_0^\infty d\lambda d\Omega \alpha_\lambda S_\lambda. \tag{3.45}$$

We only consider the case where the absorptive opacity is from a number of non-overlapping bound-bound lines transitions, in which case the radiative equilibrium equation is

$$\sum_i K_i \oint \int_0^\infty d\lambda d\Omega \phi_i \lambda (I_\lambda - S_\lambda) + \dot{E}_{dep} = 0, \tag{3.46}$$

where the sum runs over all lines. From the Sobolev formalism, we have the following expression for the specific intensity I_λ within the line:

$$I_\lambda = e^{-H(\lambda)\tau} I_\lambda^{\rm ext} + (1 - e^{-H(\lambda)\tau}) S, \tag{3.47}$$

where $I_\lambda^{\rm ext}$ is the external specific intensity incident on the line. The function H describes how much of the line profile has been traversed at wavelength λ,

$$H(\lambda) = \int_0^\lambda \phi(\lambda') d\lambda'. \tag{3.48}$$

Consequently $dH = \phi(\lambda) d\lambda$. The equation of radiative equilibrium can now be written

$$\sum_i K_i \oint \int d\Omega dH (I_\lambda^{\rm ext} e^{-H\tau_i} - S_\lambda e^{-H\tau_i}) + \dot{E}_{dep} = 0, \tag{3.49}$$

which is integrated to yield

$$4\pi \sum_i K_i(\bar{J}_\lambda^{\rm ext}\beta_i - S_\lambda\beta_i) + \dot{E}_{dep} = 0. \tag{3.50}$$

Using the expressions for K_i and S_λ in Equations 3.27 and 3.35, we arrive at the desired equation of radiative equilibrium

$$\frac{4\pi}{ct_{\rm exp}} \sum_i \lambda_i\omega_i \Big[J_i^{ext}(\vec{r}) - B(\lambda_i, T(\vec{r})) \Big] + \dot{E}_{dep} = 0, \tag{3.51}$$

where

$$\omega_i = \bar{\epsilon}(1 - e^{-\tau}). \tag{3.52}$$

Here ω_i is a number between 0 and 1 which we call the line weight, as it describes the importance of a line in the radiative equilibrium equation. For optically thin lines $\omega_i \to \epsilon\tau$, whereas for very optically thick lines $\omega_i \to 1$.

The quantity $\bar{J}_\lambda^{\rm ext}$ can be estimated from the MC transfer much as was described for gamma-ray deposition in §3.3.1, by counting the number of photons that redshift into the range $(\lambda, \lambda + d\lambda)$ within a certain volume and time. Upon coming into resonance with a line, a photon packet with energy E contributes to the monochromatic energy density

$$du_\lambda d\lambda = \frac{E_p}{V_c}\frac{E}{E_p}\frac{dt}{\Delta t}. \tag{3.53}$$

In this case, dt is the time the photon spent with a wavelength within $(\lambda, \lambda + d\lambda)$, which from the Doppler shift formula is $dt = t_{\rm exp} d\lambda/\lambda$. Using this and Equation 3.20 gives

$$J_\lambda = \frac{1}{4\pi}\frac{L_0}{V_c N_{esc}}\frac{ct_{\rm exp}}{\lambda}\sum_j \frac{E}{E_p}, \tag{3.54}$$

where the sum runs over all photons that come into resonance with the line at wavelength λ. Plugging this into Equation 3.51 gives us the equation for the temperature T in a given cell

$$\frac{4\pi}{ct_{\rm exp}} \sum_i \lambda_i\omega_i B(\lambda_i, T) = \dot{E}_{dep} - \frac{L_0}{V_c N_p}\sum_i \omega_i \left(\sum_j \frac{E_j}{E_p} \right). \tag{3.55}$$

The sum over i runs over all lines, and the sum j over all packets that come into resonance with a line at wavelength λ_i. Equation 3.55 is a nonlinear equation for T which is readily solved numerically. The temperature determined in this way is of course subject to random noise, and so the MC simulation must be continued long enough such that a large number of packets pass through every cell. However, because every packet passing through a cell contributes to Equation 3.55, the number of packets needed to determine the temperature structure is typically much less than that needed to calculate the emergent spectrum.

The temperature computed by solving Equation 3.55 will generally differ from the temperature used initially to compute the opacities and thermal emissivity. Therefore we must iterate the procedure, recomputing the opacities and re-running the MC transfer until the model becomes self-consistent.

3.4 Some Example Calculations

A MC transfer code implementing the above ideas was written in C++, and parallelized using a hybrid of MPI and openMP. The code has been run on as many as 2048 processors at once on the IBM SP supercomputer Seaborg at NERSC. Numerous verification tests have been performed. The formation of a single unblended P-Cygni line profile from a sharp photosphere has been matched to the semi-analytic formula of Equation 2.5. For the case of blended lines in the absence of continuous opacity, output spectra have be compared to those from the formal integral code SYNOW (Branch et al., 1985; Fisher et al., 1997). Continuum polarization calculations have been tested against the analytical formulae of Brown & McLean (1977) in the optically thin case, and the results of Hillier (1994) and Chandrasekhar (1960) in the optically thick case. Temperature structure calculations have been tested in the analytically solvable case of widely separated lines. In addition, detailed output of the code was compared to a very similar code developed by Thomas (2003). Although the radiative transfer methods were developed in collaboration, the two codes were written completely independently, providing a very powerful check for bugs.

The example models shown in this section were calculated on a 3-D grid of 10^6 cells.

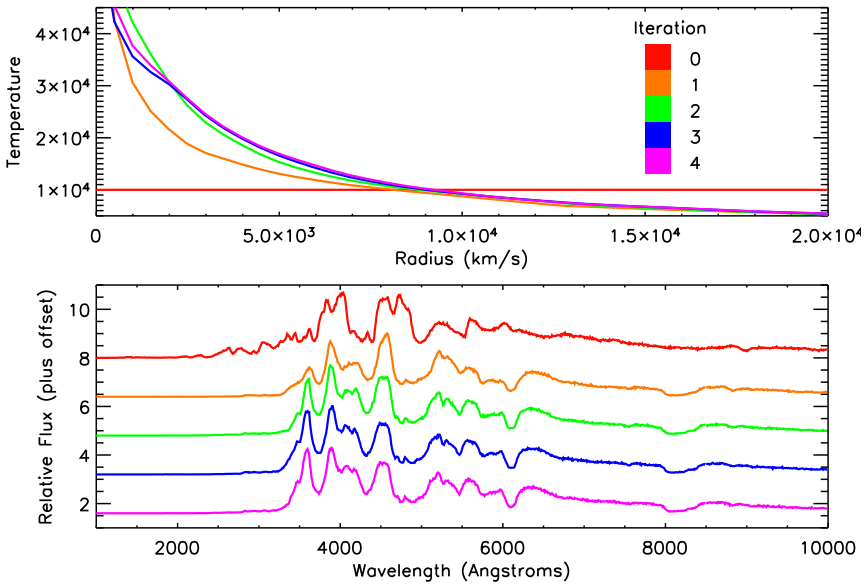

Figure 3.5 Convergence of a spherical SN Ia model, using the W7 compositions shown in Figure 2.2.

We use a line list from Kurucz (1993) containing about 500,000 transitions. In practice, storing the opacity of all these lines on a 3-D grid poses an impossible memory requirement. Thus we typically bin all lines within a width of 50 km s^{-1}, and keep only those bins with summed optical depth greater than $\tau_{\rm min} = 0.01$. We assured ourselves that the spatial and wavelength griding were acceptable by confirming that the output did not change as the resolution was increased.

3.4.1 Convergence Tests

Figure 3.5 shows MC radiative transfer calculations for the spherical SN Ia explosion model W7 (Nomoto et al., 1984). Beginning with an isothermal atmosphere, the convergence of the temperature structure is remarkably fast, with the spectrum and temperature changing negligibly after just three iterations. In general, the speed of convergence

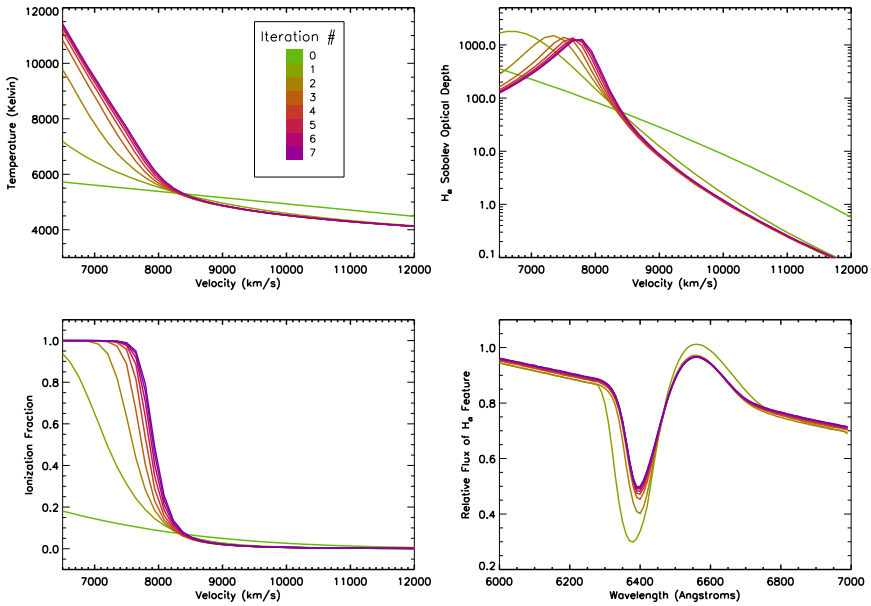

Figure 3.6 Convergence of a spherical hydrogen atmosphere model. The ionization front is seen in the bottom-left plot.

of a model depends upon how much $\bar{J}_\lambda^{\rm ext}$ and ω_i vary from one iteration to the next. The rapid convergence seen in Figure 3.5 is the result of two factors: (1) the weights ω_i saturate at 1 for $\tau \gg 1$, and are therefore insensitive to the exact optical depth of strong lines; (2) the temperature dependence of the opacity in SNe Ia is rather weak, thus the variation of $\bar{J}_\lambda^{\rm ext}$ with iteration is small.

An opposite situation occurs in a pure hydrogen atmosphere, where the opacity changes very suddenly at the hydrogen ionization temperature. Figure 3.6 shows the formation of an ionization front in a spherical, pure hydrogen atmosphere. The supernova photosphere forms near this front due to the increased opacity of electron scattering in ionized hydrogen. Interior to the front, the trapping of photons leads to a sharp rise in temperature, while outside the temperature structure flattens. Despite the sharp temperature dependence, convergence remains stable and relatively fast.

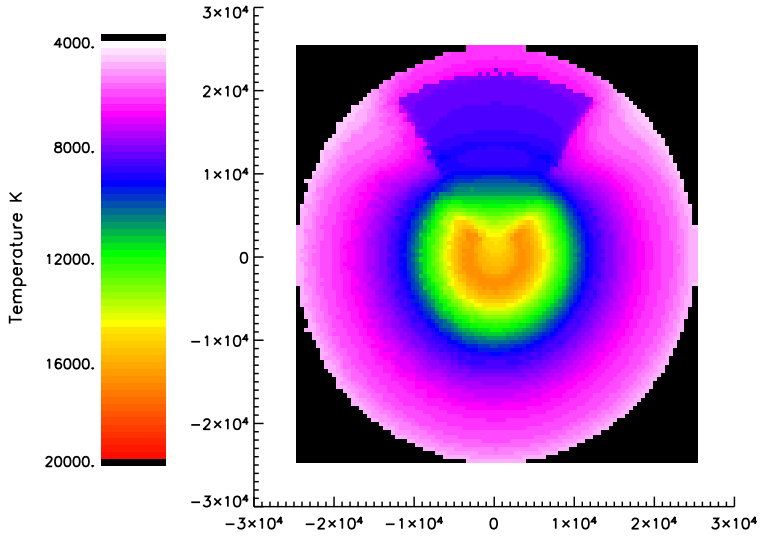

Figure 3.7 Converged temperature structure of a SN Ia that has had a conical hole carved out of it (see Chapter 5). In the inner optically thick layers, the lower opacities in the hole enhance radiative cooling, and the material is colder than the surroundings. In the outer optically thin layers, the material in the hole is exposed to bluer and more intense radiation from below, and so is hotter than the surroundings.

The beauty of the MC approach is that these favorable convergence properties do not depend upon any symmetry of the problem. Because photon packets sample every possible trajectory, the coupling of distant points in the atmosphere is handled naturally. The primary factor affecting convergence is that already mentioned, namely the temperature dependence of the opacity. Figure 3.7 shows the converged temperature structure for a SN Ia with a conical hole carved out, which will be the focus of our discussion in Chapter 5. The aspherical model converged in four iterations, as quickly as the spherical case.

Chapter 4

SN 2001el and the Geometry of High Velocity Material in SNe Ia

4.1 Introduction

SN 2001el was the first normal Type Ia supernova observed with a significant intrinsic polarization signal (Wang et al., 2003a). Most previous observations of SNe Ia had shown no obvious polarization given the signal-to-noise ratio of the observations (Wang et al., 1996b). The one exception was the subluminous and spectroscopically peculiar SN Ia 1999by, which showed an intrinsic continuum polarization of about 0.7% (Howell et al., 2001). Chemical inhomogeneities were also suggested to explain the rather noisy polarization data of SN 1996X (Wang et al., 1997). The breakthrough of the SN 2001el detection was in part due to the brightness of this nearby object, which allowed for early observations with high signal-to-noise ratio.

The polarization of SN 2001el provided the first definitive evidence that some normal SNe Ia are aspherical. But the supernova showed another interesting peculiarity as well – during the epochs prior to maximum light, SN 2001el displayed an unusual Ca II IR triplet absorption profile that indicated some ejecta were moving very fast, about twice

the velocity of the photosphere. The polarization of the high velocity calcium feature was interesting – the level of polarization was high, and the polarization angle distinct from the rest of the spectrum. This suggests that the geometry of the high velocity material differed from the bulk of the ejecta.

The relatively high signal-to-noise ratio and spectral resolution of the SN 2001el observations allow us to model the polarization over the unusual high-velocity line feature. In this chapter we take an empirical approach, fitting the data with hand-tailored, parameterized 3-D configurations by trial and error. A unique 3-D reconstruction of the geometry is not possible, however, by restricting our attention to the parameterized systems, we can draw some general conclusions about the viability of different scenarios. In particular, we examine the case where the inner ejecta layers are ellipsoidal, and the outer, high-velocity structure is one of four possibilities: a spherical shell, an ellipsoidal shell, a clumped shell, or a toroid. The calculations help us understand the generic polarization signatures arising in these relevant geometries.

4.2 Supernova SN 2001el and High Velocity Material

4.2.1 Flux Spectrum

SN 2001el was a nearby, bright supernova ($m_B \approx 12$ mag at peak) discovered in NGC 1448 (Monard, 2001). Spectropolarimetric observations were taken on Sept 25, Sept 30, Oct 9 and Nov 9 of 2001; descriptions of the observations and data reduction are given in Wang et al. (2003a).

Figure 4.1a shows the flux spectrum of SN 2001el from the earliest (Sept 25) observations. The spectrum resembles that of the normal SN Ia 1994D at about 7 days before maximum light, with the expected P-Cygni features due to Si II, S II, Ca II, and Fe II (see, e.g., Branch et al., 1993). The blueshifts of the minima of these features can be used to estimate the photospheric velocities of SN 2001el, which for all features are found to be $v_{ph} \approx 10,000$ km s^{-1}.

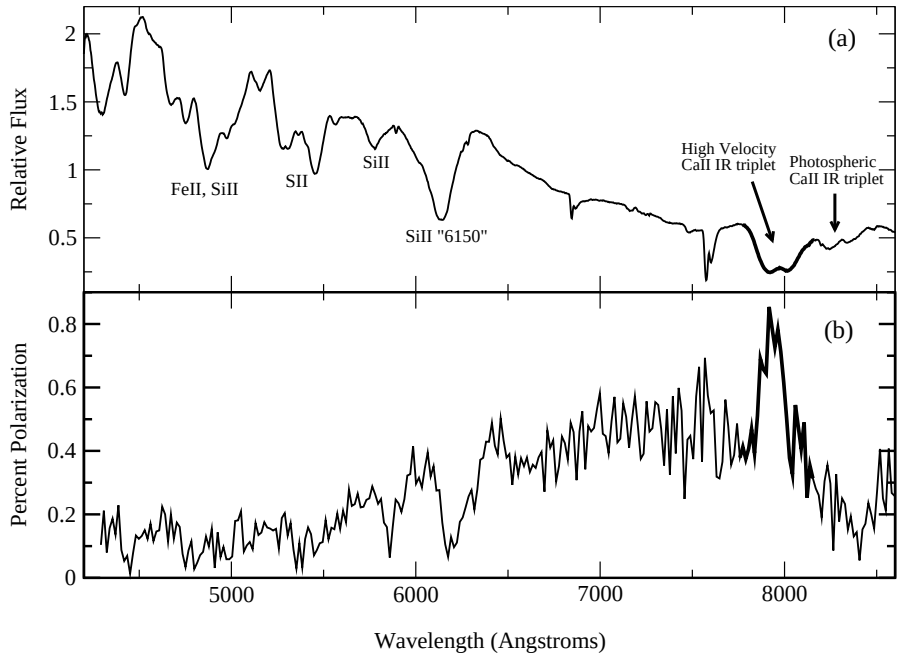

Figure 4.1 Flux and polarization spectrum of SN 2001el taken on Sept 25. The HVM feature is shown in bold lines. The minima of the HVM feature are at 7920 Å and 8015 Å, while the two minima of the photospheric IR triplet feature are at 8240 Å and 8340 Å. The polarization spectrum has had ISP subtracted, as discussed in the text.

The only truly unusual feature of the SN 2001el spectrum is a strong absorption near 8000 Å. The absorption has a "double-dipped" profile, consisting of two partially blended minima, one at 7920 Å and another at 8015 Å. It seems to be a pure absorption feature with no obvious emission component to the red. The feature is still strong on Sept 30, but has weakened considerably by Oct 9. By the Nov 9 observations, the 8000 Å feature has virtually disappeared.

Hatano et al. (1999) identified a much weaker 8000 Å feature in SN 1994D as a highly blueshifted Ca II IR triplet. The double-dipped profile clearly visible in SN 2001el strongly supports this conclusion. The red-most line of the triplet (λ8662) produces the red-side minimum while the two other triplet lines (λ8542 & λ8498) blend to produce the

blue-side minimum (the synthetic spectra to be presented in §4.4 will confirm that the IR triplet can reproduce the shape of the double minimum). We have investigated all other potential lines that might have caused the 8000 Å feature, but found none able to reproduce the feature without also producing an unobserved line signature somewhere else in the spectrum.

Adopting the IR triplet identification for the 8000 Å feature, the implied calcium line of sight velocities span the range $18,000 - 25,000$ km s^{-1}. This should be contrasted with the photospheric velocity of 10,000 km s^{-1} as measured from the normal SN Ia features. We therefore make the distinction between the *photospheric material*, which gives rise to a seemingly normal spectrum (hereafter, the "photospheric spectrum"), and the *high velocity material* (HVM), which produces the unusual 8000 Å feature. As velocity is proportional to radius in supernova atmospheres, the HVM corresponds to a detached structure at the outer edge of the supernova ejecta. Figure 4.2 illustrates how such a two-component CaII IR triplet feature would be formed. Although the HVM is illustrated as a spherical shell in the figure, its geometry is precisely what we want to explore below.

A high velocity Ca II IR triplet feature has been observed in other SNe Ia, albeit rarely and never as strong. The pre-maximum spectra of SN 1994D (Patat et al., 1996; Meikle et al., 1996; Filippenko, 1997), show a similar, but much weaker absorption. The Si II and Fe II lines of these spectra also suggest some material is moving faster than 25,000 km s^{-1} (Hatano et al., 1999). The earliest spectrum of SN 1990N at day -14 (Leibundgut et al., 1991) has a deep, rounded 8000 Å feature, and the spectrum also showed evidence of high velocity silicon or carbon (Fisher et al., 1997). The 8000 Å feature has also been observed in the maximum light spectrum of SN 2000cx (Li et al., 2001a). In this case, the line widths are narrower and the two minima are almost completely resolved.

In SN 2001el, the only clear-cut high velocity spectral feature seems to be the 8000 Å feature – we therefore refer to it as *the* HVM feature. Unfortunately, the early-time spectra do not extend far enough to the blue to observe a corresponding high velocity component in the Ca II H&K lines. Almost certainly the HVM contains only a fractional abundance of calcium, but the densities are apparently low enough that only the intrinsically

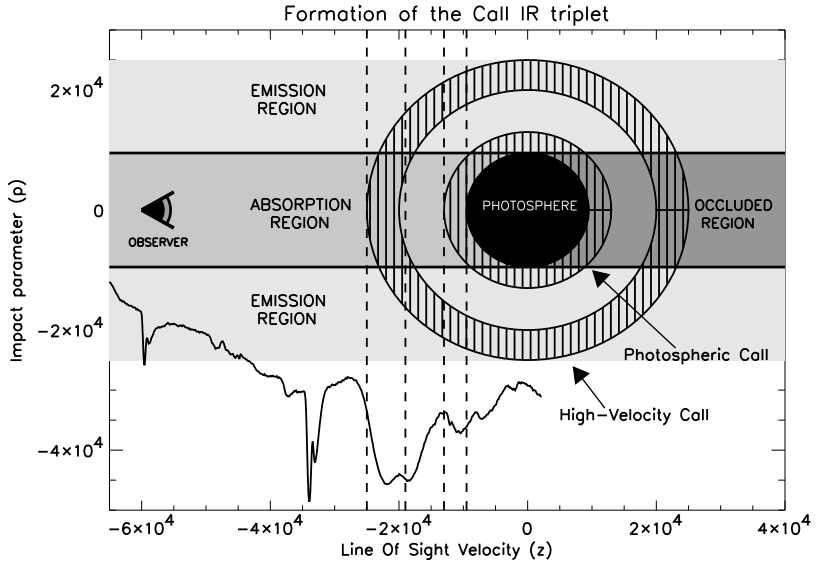

Figure 4.2 Schematic diagram of the line formation of the Ca II IR triplet feature in SN 2001el. The HVM has for illustration been shown as a spherical shell. The line profile below is the observed flux spectrum of the HVM feature. The vertical lines represent a few of the CV planes of the λ8542 line. Each CV plane corresponds to a unique wavelength in the spectrum, given in the figure by the wavelength at which they intersect the line profile.

very strong IR triplet lines are noticeable. Detached high velocity features from Ti II and Fe II, in addition to Ca II, have in fact been observed in SN 2000cx (Branch et al., 2004).

4.2.2 Polarization Spectrum

The polarization data for SN 2001el are shown in the $q - u$ plot of Figure 4.3. In order to study the intrinsic supernova polarization, we must first subtract off the interstellar polarization (ISP), caused by the scattering of the radiation off aspherical dust grains along the observer's line of sight. The ISP has a very weak wavelength dependence (Serkowski et al., 1975), and therefore choosing the magnitude and direction of the ISP is basically

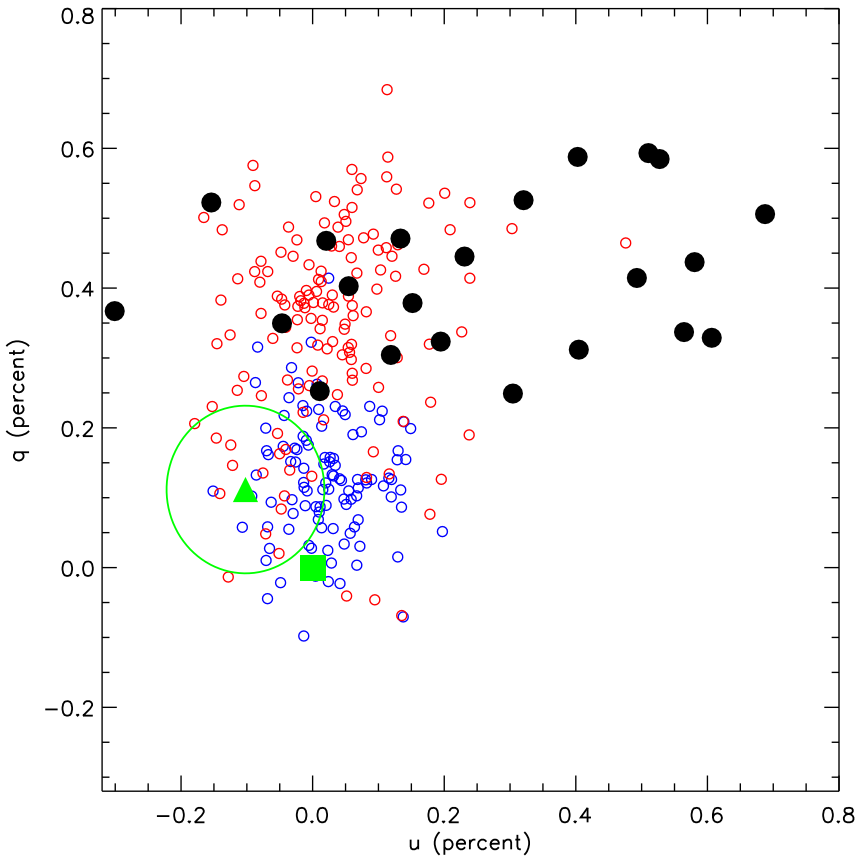

Figure 4.3 q-u plot of SN 2001el on Sept 25. The large filled circles correspond to the wavelengths of the HVM feature (7800-8100 Å) while the small open circles are from the photospheric spectrum (blue circles represent 4000-6000 Å, and red circles 6000-8500 Å). The green square at the origin represents the ISP choice used in this chapter, while the green triangle is the ISP suggested by later time observations. (Note that the original data have been rotated such that the photospheric spectrum lies along the q-axis).

equivalent to choosing the zero-point of the intrinsic supernova polarization in the q-u plane. The particular choice of ISP can dramatically affect the theoretical interpretation of the polarization data (see Leonard et al., 2000a; Howell et al., 2001). In SN 2001el, the choice of the ISP that leads to the simplest theoretical description is shown as the green square in Figure 4.3. In this case, the photospheric portion of the spectrum (open circles) draws out a straight line in the q-u plane – i.e. apart from some scatter, the degree of polarization changes across the photospheric spectrum, but the polarization angle remains fairly constant. This would be the case if all of the photospheric material obeyed a nearly axial symmetry.

Although the square in Figure 4.3 is favored by simplicity arguments, it is preferable to make a direct measurement of the ISP, if possible. At late epochs it is believed that the supernova ejecta become optically thin to electron scattering. The intrinsic supernova continuum polarization would then be zero, and the observed polarization would be due only to the ISP. Wang et al. (2003a) estimated the ISP in this way, using observations taken on Nov 9. Assuming the intrinsic supernova polarization is zero at this time, the determined ISP (with an estimated error contour) is shown as the green triangle in Figure 4.3. Although the ISP thus determined is not grossly inconsistent with the simplest choice, it seems to indicate that the polarization zero-point lies off the photospheric q-u line (open circles). If this is true, the angle across the photospheric spectrum is no longer constant. The photospheric material approximates an axial symmetry, but an off-axis, sub-dominant component (e.g. a photospheric clump) must exist to account for the offset from the q-u line.

Because the main purpose of this chapter is to explore the geometry of the HVM, not the photosphere, we will simplify our discussion by ignoring any off-axis photospheric components. We will assume the polarization zero-point of the axially symmetric component is given by the square and that the photosphere can be approximately modeled as an ellipsoid. Although the particular ISP choice has important implications for the geometry of the photospheric material, it does not greatly affect our analysis of the HVM feature.

The intrinsic polarization spectrum of SN 2001el using our choice of ISP is shown

in Figure 4.1b. The degree of polarization rises from blue to red, as expected in ellipsoidal models due to the higher line opacity in the blue (Howell et al., 2001). The level of continuum polarization in the red is about 0.4%, which in an ellipsoidal model would correspond to an asymmetry of 10% (Höflich, 1991). The HVM flux absorption feature is associated with a large polarization peak, but the noise and the low spectral resolution of the polarization spectrum do not permit identification of individual peaks associated with each line of the CaII IR triplet.

In Figure 4.3, the wavelengths corresponding to the HVM feature are shown with closed circles. The HVM polarization angle deviates from the photospheric one, pointing instead mostly in the u-direction. The HVM feature also shows an interesting looping structure – as the wavelength is increased, the polarization moves counter-clockwise in the q-u plane. Such "q-u loops" have been observed previously in the Hα feature of SN 1987A (Cropper et al., 1988).

The different polarization angle of the HVM feature means that the geometry of SN 2001el cannot be completely axially symmetric. This follows from symmetry arguments alone – the Stokes u parameter changes sign upon reflecting the system about the polarization reference axis, and therefore must be zero for any system with a reflective symmetry. A natural explanation of the relatively large degree of polarization and change of polarization angle of the HVM feature is partial obscuration of polarized photospheric light, somewhat like Figure 2.8d discussed in §2.3.2. Here the asymmetrical distribution of HVM optical depth preferentially blocks the right-diagonally polarized photosphere light, causing a more incomplete cancellation of the polarization. In the next section we describe a technique for calculating partial obscuration that allows us to test our interpretation by comparing synthetic polarization spectra to the data. We will find in §4.4 that partial obscuration can indeed account for the degree and angle of polarization of the HVM feature, including the q-u loop behavior.

4.3 A Two-Component Model

For the problem at hand, we can take a simplified approach to the radiative transfer problem. Assuming that the electron densities in the HVM regime are $\lesssim 10^8$ cm^{-3}, the optical depth to electron scattering through the HVM shell is $\tau_{es} = n_e \sigma_t R_{sh} < 10^{-2}$. Therefore one can ignore electron scattering in the HVM, and the radiative transfer problem separates naturally into the two regimes of photosphere and HVM. The photosphere acts as a source of polarized light illuminating a region of pure line optical depth in the HVM. Assuming the lines are depolarizing, the only effect of the HVM is to obscure some of the polarized photospheric light and re-emit some unpolarized light into the observer's line of sight.

The geometry used in the models is shown in Figure 4.4. We use a cylindrical coordinate system (p, ϕ, z) where the observer line of sight is the z axis with z decreasing toward the observer (i.e. the observer is at negative infinity). The polarization reference axis is chosen to lie along the $\phi = 0$ direction, which is also the photosphere symmetry axis.

To calculate line formation, we use the Sobolev formalism described in §2.2.1. In the case of a monotonically expanding atmosphere with more than one line, a beam of radiation will come into resonance with each line one at a time, starting with the bluest line and moving to the red. In this case, Equation 2.4 for the specific intensity reaching an observer is readily generalized to include polarization and multiple lines,

$$\mathbf{I}(\lambda, p, \phi) = \mathbf{I_0}(\lambda, p, \phi) \exp\left(- \sum_{i=1}^{N} \tau_i \right) + \sum_{i=1}^{N} \mathbf{S_i}(\lambda, p, \phi)[1 - e^{\tau_i}] \exp\left(- \sum_{j=1}^{i-1} \tau_j \right), \qquad (4.1)$$

where the indices i and j run over the lines from red to blue. Here $\mathbf{I_0}$ is the Stokes specific intensity emerging from the photosphere, and is assumed to be known (see next section). $\mathbf{S}$ is the line Stokes source function, and τ its Sobolev optical depth. The 3-D distribution of τ will be varied through trial and error to attempt to find a geometry appropriate to SN 2001el.

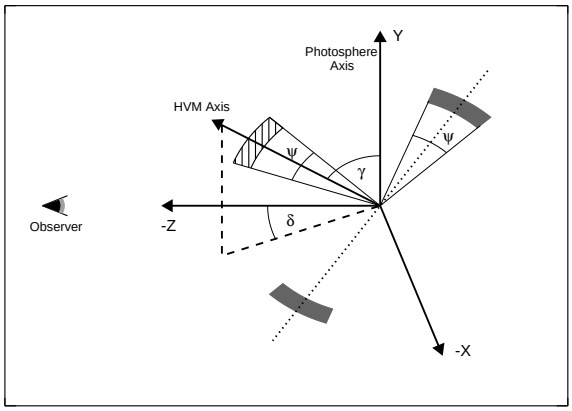

Figure 4.4 Geometry used in the models. The line of sight is in the negative z-direction. The y-axis is both the polarization reference direction and the photosphere symmetry axis. The angles γ and δ define the orientation of the HVM symmetry axis, where γ is the angle between the y-axis and the HVM axis, and δ is the angle between the line of sight and the projection of the HVM axis onto the $z-x$ plane. ψ denotes the opening angle of the clump (hashed arc) and the toroid (solid arc). The two structures are generated by spinning the arcs about the HVM axis.

4.3.1 The Photospheric Intensity

We model the photospheric region as an inner unpolarized boundary surface (the inner core), surrounded by a pure electron scattering envelope with a power law electron density $\rho \propto r^{-n}$. We choose $n = 7$, a density law motivated by SN Ia explosion models and one that has been often used in direct spectral analysis (Nomoto et al., 1984; Branch et al., 1985). The optical depth (in the radial direction) from the inner boundary surface to infinity is set at $\tau_{in} = 3$. The assumption of a pure electron scattering atmosphere should be a good one for the wavelength range we are interested in. The photons that redshift into resonance with the high velocity IR triplet are those with wavelengths from 8000-8500 Å, and there are no strong lines or absorptive opacities in this region of the spectrum (see Pinto

& Eastman, 2000a). The wavelength dependence of the photospheric intensity is assumed to follow a blackbody distribution with a temperature $T_{bb} = 9000$ K, chosen to fit the slope of the red continuum. We do not attach any physical significance to the value of T_{bb}, but consider it only a convenient fit parameter.

We have used the Monte Carlo techniques described in Chapter 3 to calculate the polarized specific intensity emergent from the photosphere. To begin, we consider the case of spherical geometry. From the circular symmetry, the intensity and degree of polarization of a specific intensity beam only depends upon the impact parameter p and not on ϕ. Let $I_z(p)$ represent the specific intensity in the $\hat{z}$ direction at p, and $P_z(p)$ the degree of polarization of this beam. The intensity and polarization emergent from the photosphere are shown in Figure 4.5 for several values of n and τ_{in}. Here p is given in units of the photosphere radius, defined as the radius at which the optical depth to electron scattering equals unity. Note that the photospheric specific intensity does not terminate sharply at the photospheric radius as often assumed in Sobolev models; rather, a significant amount of light is scattered into the line of sight out to $p \approx 1.4$. Since this limb light is highly polarized (up to 40%) it is important to include it in our calculations. $I_z(p)$ has become negligible out at the HVM distances of $p \approx 2$, which confirms that we can make a clear separation between the photospheric and HVM regimes. We also see that the photospheric light does not depend strongly on our choice of n or τ_{in}.

For $\phi = 0$, the polarization points in the horizontal, or negative Q direction – i.e., $Q(p, \phi = 0) = -I_z(p)P_z(p)$ while $U(p, \phi = 0) = 0$. The Q and U components at arbitrary ϕ are derived by rotating this expression by ϕ using the rotation matrix Equation 3.39,

$$\mathbf{I_0}(p, \phi) = \begin{pmatrix} I_0 \\ Q_0 \\ U_0 \end{pmatrix} = \begin{pmatrix} I_z(p) \\ -P_z(p) I_z(p) \cos(2\phi) \\ -P_z(p) I_z(p) \sin(2\phi) \end{pmatrix}. \tag{4.2}$$

To take into account the asphericity of the photosphere in SN 2001el, we use the fact that the small degree of polarization suggests a rather small ($\sim 10\%$) deviation from sphericity. It should therefore not be a bad approximation to apply the spherically

symmetric specific intensities to a slightly distorted photosphere (see Shapiro & Sutherland, 1982; McCall, 1984; Jeffrey, 1991; Cassinelli & Haisch, 1974). In our models we will only consider the case of an oblate ellipsoidal atmosphere with axis ratio E and viewed edge-on. We define an ellipsoidal coordinate

$$\eta = p\sqrt{1 + (E^2 - 1)\sin^2\phi}. \tag{4.3}$$

Our approximation is that the emergent Stokes intensity from a position (η, ϕ) is given by Equation 4.2 with $I_z(p = \eta, \phi = \phi)$ and $P_z(p = \eta, \phi = \phi)$. In this case we find an axis ratio of $E \approx 0.9$ is necessary to produce the 0.4% polarization observed in the red continuum of SN 2001el. The result agrees with previous, 2-D calculations (Jeffrey, 1991; Höflich, 1991).

While the above photospheric model provides a simple and rather general description of an axially symmetric photosphere, there is no easy way to assure ourselves that this photospheric model is unique. The actual specific intensity emergent from an ellipsoidal atmosphere can depend on the depth and shape of the inner boundary surface, as well as on the inclination of the system. Moreover, the polarization of the photospheric spectrum of SN 2001el could arise from a different kind of asphericity altogether, for instance an off-center Ni^{56} source, or a clumpy atmosphere. In the absence of a single preferred photospheric model, we proceed with the above model, but reiterate that it remains just one of many possible scenarios. Other choices of $I_z(p, \phi)$ and $P_z(p, \phi)$ must be investigated on a case by case basis.

4.3.2 The Line Optical Depth and Source Function

In our synthetic spectrum fits, we take the optical depth of the λ8542 line as a free parameter τ_1. The optical depths of the other two lines (λ8662, λ8498) are derived from τ_1. All three triplet lines come from nearly degenerate lower levels, so in LTE the relative strength of each line depends only upon the weighted oscillator strength gf of the atomic transition. Even if the level populations deviate from LTE, one expects the deviation to affect each of the nearly degenerate levels in a similar way. The λ8542 line has the largest gf value; λ8662 is 1.8 times weaker, and λ8498 is 10 times weaker.

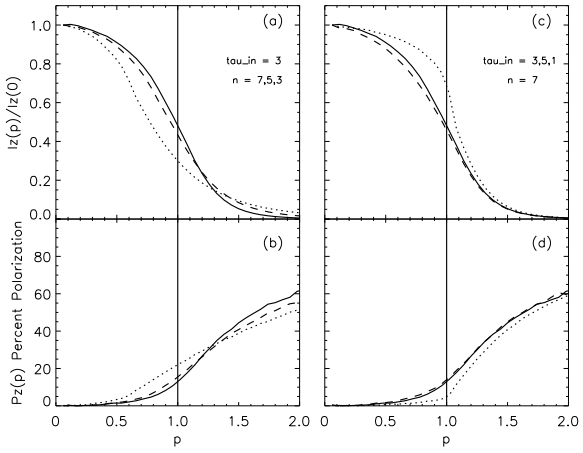

Figure 4.5 The intensity and polarization of specific intensity beams emerging from the spherical electron scattering photosphere. The impact parameter p is given in units of the photospheric radius, defined as continuum optical depth of one. The solid lines are the values used in this chapter and the others lines show comparisons with slightly different models. Panels (a,b) show the dependence on the power law index n assuming $\tau_{in} = 3$; solid line: $n = 7$, dashed line: n=5, dotted line: $n = 3$. Panels (c,d) show the dependence on inner optical depth τ_{in} assuming $n = 7$; solid line: $\tau_{in} = 3$,dashed line: $\tau_{in} = 5$, dotted line: $\tau_{in} = 1$.

For the reasons discussed in §2.3.3, we assume light scattered or created in a line is unpolarized. For the present case, this is further justified by the facts that the polarizability factor for the IR triplet lines is almost zero for $\lambda 8542$ ($W_2 = 0.02$) and exactly zero for $\lambda 8662$. According to the Hamilton prescription, only the $\lambda 8498$ line has a moderate polarizing effect ($W_2 = 0.32$), but this line is by far the weakest of the three. On the basis of the spectral fits of §4.4, we will argue that the lines of the IR triplet are saturated ($\tau_1 \gtrsim 5$) for the HVM in front of the photosphere; therefore multiple scattering within the line will also tend to make the scattered light isotropic and unpolarized.

For an isotropic, unpolarized source function, the Stokes vector is $\mathbf{S} = (S_0, 0, 0)$.

For S_0 we use the parametrized two-level equivalent atom source function given by Equation 3.32. The incident radiation from the photosphere is geometrically diluted by a factor of roughly $\pi r_{ph}^2/4\pi r_{HVM}^2 \approx 1/16$. Thus for a pure scattering line ($\bar{\epsilon} = 0$), the intensity of the line source function is about 16 times weaker than the average photospheric intensity. At the other extreme, for a thermalized line ($\bar{\epsilon} = 1$) and an HVM temperature of 5500 K, the line source function is about 4 times weaker than the average photospheric intensity. Because the line source function light is unpolarized and relatively weak, we find in the end that it has little effect on the synthetic line profiles. The exact value of ϵ is thus not of great importance. In our models, we use $\epsilon = 0.01$.

4.3.3 The Integrated Spectrum

To obtain the observed Stokes fluxes at a certain wavelength one must integrate the specific intensity over the CV planes of each line. For those CV planes behind the photosphere, we must also account for the attenuation of the line source function light due to scattering off electrons as the beam passes through the photospheric region. If we define $\tau_{es}(p, \phi, z)$ as the electron scattering optical depth along the z-direction from the point (p, ϕ, z) to the observer, then a fraction $(1 - e^{-\tau_{es}})$ of photons will be scattered out of the line of sight on their way to the observer. We assume these photons are simply removed from the beam and are not subsequently re-scattered into the line of sight.

For a single line atmosphere, the integrated Stokes fluxes at wavelength λ are given by integrating Equation 4.1 over the correspond CV plane at z_r:

$$F_I(\lambda) = \int\int \left[I_z(\eta, \phi) e^{-\tau} + (1 - e^{-\tau}) S_0(p, \phi, z_r) e^{-\tau_{es}} \right] p dp d\phi, \tag{4.4}$$

$$F_Q(\lambda) = \int\int P_z(\eta, \phi) I_z(\eta, \phi) \cos(2\phi) e^{-\tau} p dp d\phi, \tag{4.5}$$

$$F_U(\lambda) = \int\int P_z(\eta, \phi) I_z(\eta, \phi) \sin(2\phi) e^{-\tau} p dp d\phi. \tag{4.6}$$

The integrals can be easily generalized to the case of multiple lines.

Given our scenario of how the high velocity Ca II polarization is formed by partial obscuration, Equations 4.6 give us some insight into what extent the HVM geometry is

constrained by the polarization measurements. For simplicity, consider the formation of a single, unblended line, above a spherical photosphere, and suppose we are trying to reconstruct the distribution of Sobolev line optical depth $\tau(p, \phi, z)$ over the entire ejecta volume. The Stokes flux at a certain wavelength gives us information about τ over the corresponding CV plane at z_r. As Equations 4.4-4.6 demonstrate, we obviously will not be able to uniquely reconstruct the distribution of τ over this plane, because all of the information gets integrated over to give the three quantities we measure: $F_I(\lambda), F_Q(\lambda)$, and $F_U(\lambda)$. What we do measure can be thought of as certain "moments" of the τ distribution over each CV plane. F_I is a type of "zeroth moment," which depends mostly upon how much material is covering the photosphere, with little dependence on its geometrical distribution. On the other hand the F_Q and F_U, because of the $\cos 2\phi$ and $\sin 2\phi$ factors, behave somewhat like "first moments," and are sensitive to how τ is distributed over the photosphere. Because the angle factors are rather low-frequency, smaller scale structures will be averaged out over the integrals, and the polarization measurements will only constrain the large scale structures in the HVM.

4.4 The Geometry of the High Velocity Material

The speed of the two-component model allows us to explore many different configurations for the HVM. We report on four possibilities here, each of which may approximate a structure that is the result of a different physical mechanism: (1) a spherically symmetric shell, (2) an ellipsoidal shell, (3) a clumped spherical shell, and (4) a toroidal structure. 3-D visualizations of the clump and toroid are shown in Figures 4.6 and 4.7, respectively. The value of using highly idealized models is that they provide general insight into the observable signatures arising in different geometries.

The detailed geometrical structure of the models is shown in Figure 4.4. The photosphere symmetry axis is the $\phi = 0$ axis, which is also chosen as the polarization reference direction. The HVM follows a distinct axis of symmetry defined by the two angles γ and δ. The velocities v_1 and v_2 denote the inner and outer radial boundaries of the

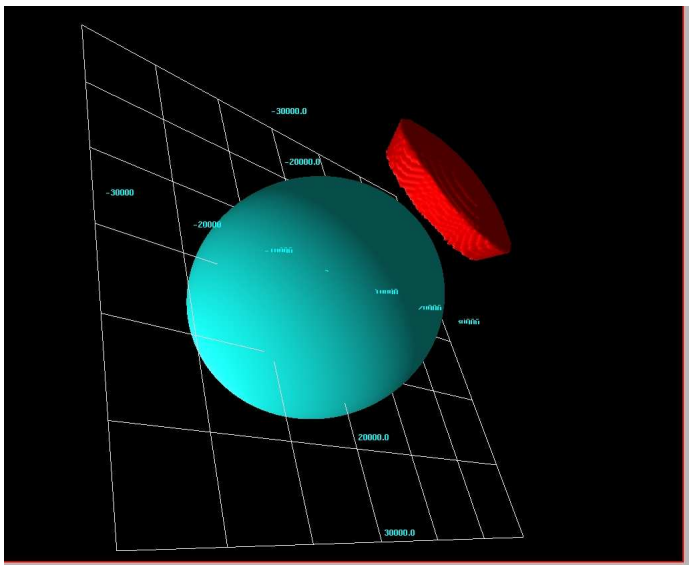

Figure 4.6 Visualization of the clump geometry for SN 2001el.

HVM, while ψ is the opening angle. The reference optical depth τ_1 of the λ8542 line is assumed constant throughout the defined structure boundaries. Table 4.1 summarizes the fitted parameters of each HVM geometry considered in the sections to follow.

Before examining the specific models, we first discuss the general constraints that must be met by any model.

4.4.1 General Constraints

Because the HVM polarization feature is caused by partial obscuration, practically all of our information on the geometry of HVM concerns the material in front of the photosphere (the absorption region). We will thus have very little information as to the amount and distribution of material in the emission and occluded regions. For a spherical shell HVM, about 5% of the material is in the absorption region, 5% is in the occluded region, and 90% is in the emission region. Thus we only probe a small portion of the potential HVM.

Table 4.1. Fitted parameters for HVM models

Name	v_1[a]	v_2[a]	E[b]	τ_1[c]	ψ[d]	γ[e]	δ[e]	fit-figure
spherical shell	20,200	25,300	1.0	0.83	-	-	-	4.9
ellipsoidal shell	21,200	24,800	0.91	1.20	-	25°	90°	4.12
clumped shell	20,600	24,300	1.0	5.0	23°	83.5°	4.2°	4.13
edge-on toroid	20,900	24,500	1.0	5.0	30°	45°	90°	4.14
inclined toroid	20,500	24,700	1.0	5.0	35°	45°	43°	4.16

[a] v_1, v_2: inner/outer radial or semi-major boundary in km s^{-1}

[b] E: Axis ratio

[c] τ_1: optical depth of reference line (λ8542)

[d] ψ: opening angle (see Figure 4.4)

[e] γ, δ: angles defining orientation of HVM symmetry axis (see Figure 4.4)

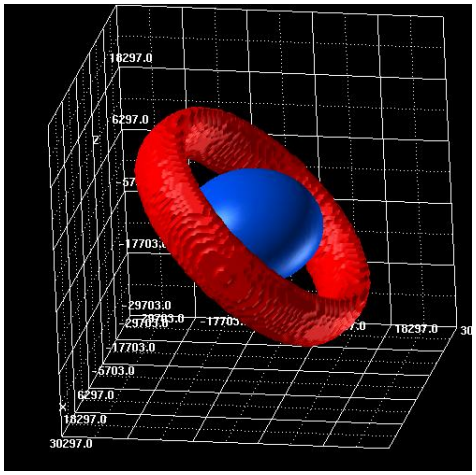

Figure 4.7 Visualization of the toroid geometry for SN 2001el.

The observed HVM feature does not have a noticeable emission feature, but this does not provide any strong constraint on the emission region material, as such a feature is predicted to be very broad and weak (see Figure 4.8). To make matters worse, the HVM emission feature overlaps with the photospheric triplet absorption and emission, making it difficult to separate the two contributions. In our models, we do not attempt to fit the region redward of 8200 Å, where this blending occurs. The best way to constrain the amount of emission region material is by line of sight variations (see §4.5). The material in the emission region from one line of sight, becomes material in the absorption region from another. With a larger sample of supernovae one may be able to piece together a picture of the entire volume of high velocity ejecta.

As for the absorption region material, we can list four general constraints directly deducible from the spectra:

(1) The width of the HVM flux absorption feature constrains τ_1 to be non-zero only over the line-of-sight velocity range $18,000 - 25,000$ km s^{-1}. τ_1 is thus confined to a relatively thin region that is significantly detached from the photosphere. The edges of the flux feature are sharp and persist over time, suggesting that the boundaries of the HVM

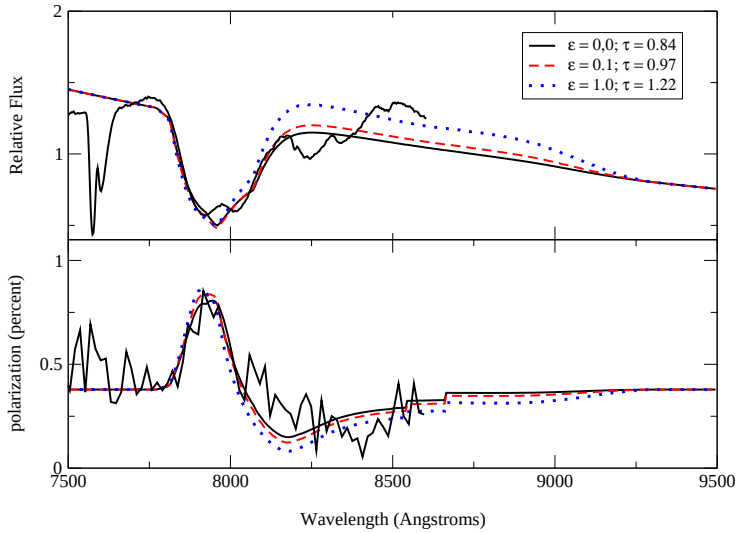

Figure 4.8 The effect of emission region material from a spherical shell at a temperature $T = 5500$ K. A pure scattering line ($\epsilon = 0$; solid line) does not produce a visible emission feature. A thermalized line ($\epsilon = 1$; dotted line) produces an emission, but because this will be blended with the photospheric triplet absorption and emission, it may still be difficult to detect.

are well-defined.

(2) At the minimum of the HVM absorption the flux has decreased by 43% from the continuum level. For geometries where the HVM covers the entire photosphere, the optical depth implied is $\tau \approx 0.8$. On the other hand, some geometries may have higher optical depths and smaller covering factors, the minimal covering factor being $f_{min} = 43\%$ for when the lines are completely opaque. (Note that in this context the term "covering factor" denotes the percent of the photospheric area obscured by the slice of HVM on a CV plane. Since this differs from the traditional usage of the term, we hereafter call this the *z-plane* covering factor.)

We can use the double-dipped flux profile to constrain the z-plane covering factor of the HVM. Because the λ8542 blue triplet line is intrinsically stronger than the λ8662

red triplet line (with a gf value 1.8 times larger), the blue minima of the IR triplet feature will be about twice as deep as the red one *unless* both lines are saturated. Because the minima in the HVM feature are of about equal depth, we conclude that the two lines are indeed saturated (i.e., $\tau_1 > 5$) and the z-plane covering factor is in fact the minimal one, $f_{min} = 43\%$.

(3) The shape of the flux profile may also constrain the value τ_1. If all three triplet lines are saturated, the blue minima will tend to be wider than the red, due to the blending of the λ8498 with the λ8542 line. The fact that both minima have roughly equal width suggests that the λ8498 line is weak while the other two lines are strong, a situation that occurs when $\tau_1 \approx 5$.

(4) Finally, the HVM polarization feature points primarily in the u-direction. This means the distribution of the HVM is weighted along the 45° line to the photosphere symmetry axis.

4.4.2 Spherical Shell

The first HVM geometry we consider is a spherically symmetric shell. The boundaries of the spherical shell must be $v_1 = 20,200$ km s^{-1} and $v_2 = 25,300$ km s^{-1} to reproduce the line width. The z-plane covering factor is found to be ~ 1, and the optical depth necessary to fit the line depth $\tau_1 = 0.77$. In Figure 4.9 we compare the synthetic spectra to the observed data. While the overall fit of the flux feature is decent, the red-side minimum is not well reproduced. We will find better fits to the double-dipped profile using non-spherical geometries with smaller z-plane covering factors and saturated lines. Thus the flux spectrum alone suggests a deviation from spherical symmetry, although the evidence is rather subtle.

The effect of the spherical shell on the polarization is demonstrated by the slice plots of Figure 4.10. At the blue end of the absorption feature (slice a), the line obscures the weakly polarized, central light, allowing highly polarized, edge light to reach the observer. This creates a peak in the polarization spectrum. Further to the red of the feature (slice b),

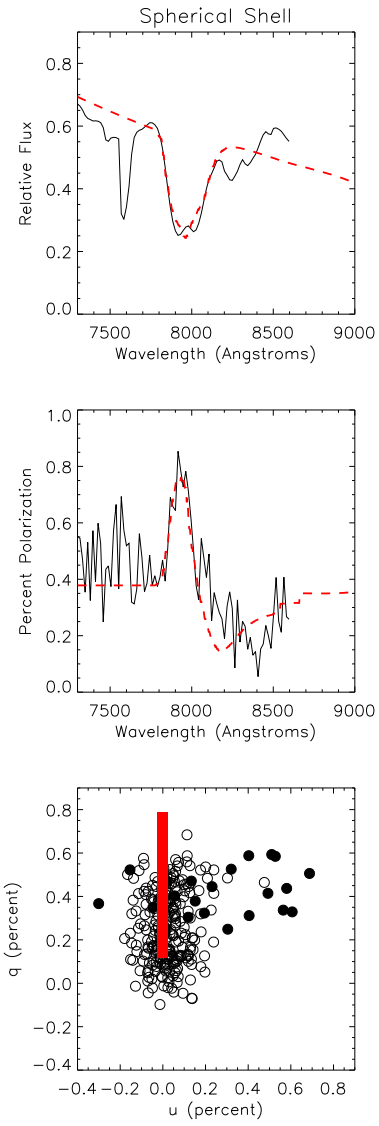

Figure 4.9 Synthetic spectrum fits to the observed HVM feature using the spherical shell model. In the top two plots, the solid black line is the observed data, and the dashed red line the fit. In the bottom q-u plot, the black circles are the data and the red squares the fit. The open circles indicate wavelengths corresponding to the photospheric spectrum and the solid circles to the HVM feature.

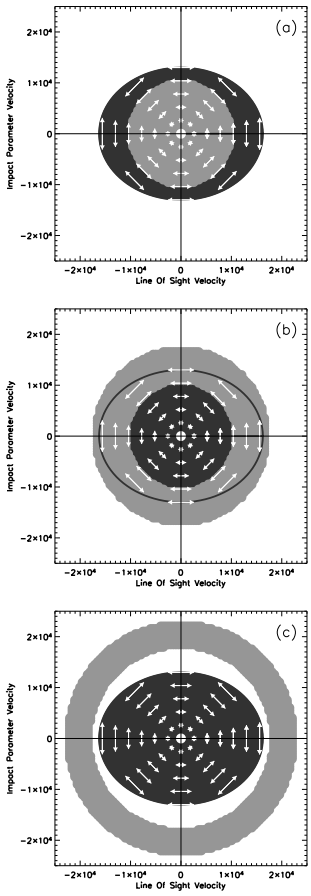

Figure 4.10 Three slices through the spherical shell HVM, which demonstrate how a detached spherical shell affects the polarization at three different wavelengths. Each slice in grey is the HVM cross-section on a plane perpendicular to the z (line of sight) axis, corresponding to a CV surface for the λ8542 line at a particular wavelength. *top*: $v_z = -22,500$ km s^{-1}$\rightarrow$ $\lambda = 7900$ Å; the line obscures the lowly polarized central light, leading to a polarization peak *middle*: $v_z = -15,500$ km s^{-1}$\rightarrow$ $\lambda = 8100$ Å; the line obscures the highly polarized edge light, leading to a depolarization of the spectrum *bottom*: $v_z = -5000$ km s^{-1}$\rightarrow$ $\lambda = 8400$ Å; the line does not obscure the photosphere, but the addition of unpolarized line source function light slightly depolarizes the spectrum. Note: the photospheric axis-ratio has been exaggerated ($E = 0.8$ rather than $E = 0.91$) to clarify the asymmetry.

the line obscures the edge light and thus depolarizes the spectrum. Even further to the red (slice *c*), the line no longer obscures the photosphere, but the emission region material emits unpolarized line source function light into the line of sight, and a small level of depolarization continues. This polarization feature resembles an inverted P-Cygni profile, as discussed in §2.3.3.

In Figure 4.9b we see that the spherical shell naturally reproduces the correct shape and size of the HVM polarization peak. The fact that the synthetic polarization feature has only a single peak is the result of a line blending effect: the red-side depolarization of the λ8542 feature suppresses the peak due to the λ8662 line. Note that while the observed depolarization minimum near 8400 Å is not well fit, this is not necessarily a weakness of the model, as the feature at these wavelengths is produced mostly by the calcium near the photosphere, which has not been included in the model. In any case, the spherical shell, which follows the axial symmetry of the photosphere, does not change the polarization position angle in the observed manner (Figure 4.9c). This rules it out as a viable model for the HVM.

4.4.3 Rotated Ellipsoidal Shell

The good fit to the polarization level in Figure 4.9 suggests that a shell-like structure may be a viable candidate for the HVM, as long as the shell is somehow distorted from perfect spherical symmetry to account for the rotation of the HVM polarization angle. The simplest scenario is one where the HVM layers of the ejecta are ellipsoidal with the same oblateness as the photospheric layers, but with a rotated axis of symmetry. A case similar to this may arise, for example, if the HVM comes from swept-up circumstellar material from the asymmetric wind of a companion star (e.g., Hamuy et al., 2003; Gerardy et al., 2003).

The effect of the rotated ellipsoidal shell on the polarization spectrum is demonstrated in the slice plots of Figure 4.11. The slices closely resemble those of the spherical shell (Figure 4.10) except that now the cross-sections of the HVM are ellipses. The shape

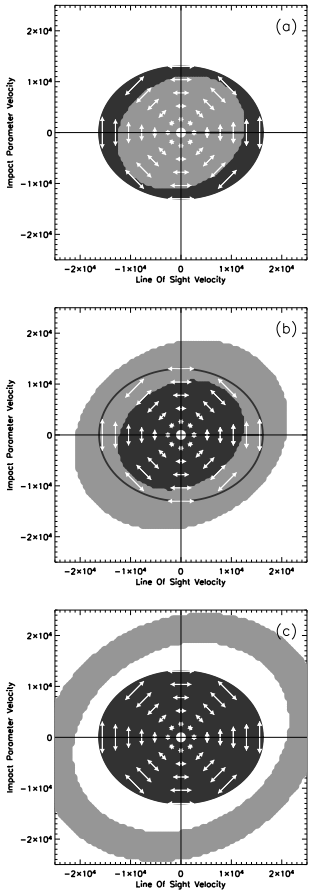

Figure 4.11 Three slices through the rotated ellipsoidal HVM. Panels are the same as in Figure 4.10. Because the rotated ellipsoidal shell preferentially obscures diagonal light, it will produce a polarization feature with a non-zero u-component. The axis ratio of both the photosphere and HVM shell are exaggerated ($E = 0.8$ rather than 0.91) in order to clarify the asymmetries.

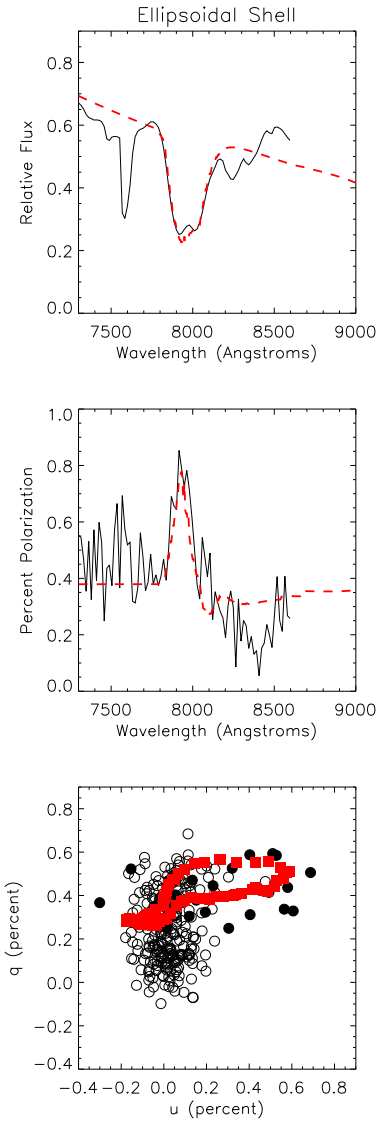

Figure 4.12 Synthetic spectrum fits using the ellipsoidal shell geometry. The panels are the same as in figure 4.9. The fits to the flux and polarization spectra are similar to the spherical shell, but now the HVM feature is polarized primarily in the u-direction. The synthetic feature draws a loop in the q-u plane, similar to that in the observed data.

and size of the flux and polarization features are thus very similar to the spherical case. For $\gamma = 0$ (HVM and photosphere axis aligned) the system is axially symmetric and the HVM polarization feature points in the q-direction. As γ is increased, the ellipses begin to absorb diagonally polarized light and the HVM polarization feature rotates into the u-direction.

The synthetic spectra for $\gamma = 25°, \tau_1 = 0.77$ are shown in Figure 4.12. The ellipsoidal shell, like the spherical one, fails to reproduce the double-dipped flux profile. On the other hand, it is able to fit the polarization peak and the change of polarization angle. Even more interestingly, the ellipsoidal shell produces a q-u loop similar to that observed in the data. In our models, we find that a q-u loop is a common signature of partial obscuration in two-axis systems. The absorption of the photospheric light typically produces a peak in both the q and u polarization. The partial obscuration effect on the q and u polarizations is distinct, so that in general these features do not peak at the same wavelength, but rather are out of phase. When plotted in the q-u plane, this phase offset makes a loop.

4.4.4 Clumped Shell

We parameterize a clumped shell as the section of the spherical shell lying within a cone of an opening angle ψ (a "bowl"-shaped structure, see Figure 4.4). A single clump like this could perhaps arise if the calcium in the HVM was produced by nuclear burning that occurred along a preferential axis. The clumped shell could also represent one piece of a shell broken into numerous clumps, a possibility discussed in more detail at the end of this section.

In deciding on the appropriate values for the clump parameters, we are guided by the constraints listed in §4.4.1. The opening angle is constrained to $\psi \approx 25°$, so as to achieve the minimal z-plane covering factor. The orientation of the clump axis is chosen so that the clump lies in between the observer and the photosphere, obscuring the photosphere's diagonal.

Through trial and error, a reasonable fit to the data was found for $\psi = 24°, \tau_1 =$

$5, \gamma = 83.5°$, and $\delta = 4.2°$ The synthetic spectra are shown in Figure 4.13. Because the lines are now saturated, the clump is able to reproduce the two equal minima of the flux absorption. The clumped shell also reproduces the important features of the polarization spectrum – i.e., the level of polarization, the polarization angle, and the q-u loop. On the other hand, the red edges of the synthetic flux and polarization spectra do not quite match those observed. In the polarization spectrum, the peak due to the λ8662 feature is not suppressed by blending as it was in the shell models. This suggests that our parameterized clump geometry may be too simple, and a more realistic model may involve a complicated superposition of clumps and shell.

Although our clumped shell model consists of only a single clump, it is possible that many more clumps exist in the emission region of the shell. The extra clumps would leave no obvious signature on the flux spectra (see §4.4.1). Clumpiness in a shell could be caused by instabilities in the burning front, such have been found in 3-D deflagration models of SNe Ia (Reinecke et al., 2002; Gamezo et al., 2003). Alternatively, if the HVM is the result of swept-up circumstellar material, the clumpiness could arise from the Rayleigh-Taylor instabilities that are expected to arise (Chevalier & Klein, 1978). The exact scale of the clumpiness is unknown – as we noted in reference to Equation 4.6, the polarization feature due to partial obscuration is not sensitive to small scale structure, giving rather the integrated "moments" of the optical depth distribution. The clump distribution is, however, constrained in two ways: (1) Whatever the size of the clumps, their angular distribution must be weighted along the clump axis defined above. If the clumps were instead small structures distributed uniformly over the shell, when integrated up they would average out to the uniform spherical shell analyzed in the previous section, which did not show a rotation of the polarization angle. (2) This weighted angular distribution of the clumps cannot vary in the radial direction. If it did, the polarization angle of the HVM feature – which is set by the distribution of the randomly placed clumps over the photosphere – would vary randomly across the HVM feature rather than forming a q-u loop oriented in the u-direction. Both of these suggest that the scale of the clumpiness is not much smaller than the single clump used in the model.

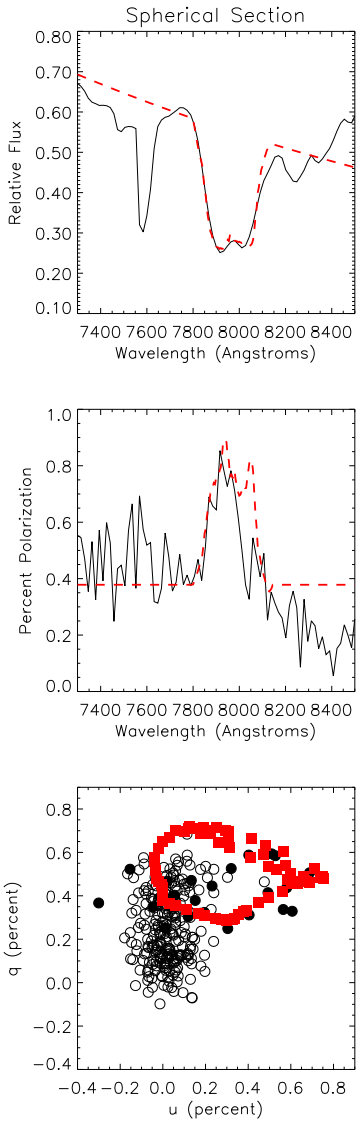

Figure 4.13 Synthetic spectrum fits using the clumped shell geometry. Panels are the same as in Figure 4.9

4.4.5 Toroid

A toroid would be an especially interesting structure to find in the ejecta of a SN Ia, as it might give a hint as to the binary nature of the progenitor system. In the currently preferred progenitor scenarios (see Branch et al., 1995), SNe Ia are the result of a white dwarf accreting material either from the Roche-lobe overflow of a companion star or the coalescence with another C-O white dwarf. The orientation of the accretion disk axis naturally suggests an independent orientation of the outer ejecta layers.

Whether an accretion disk could be swept up into a toroidal structure after the supernova explosion can only be addressed by multi-dimensional explosion modeling. Here we can calculate what effect such a structure would have on the flux and polarization spectrum, and whether it could possibly account for the HVM feature in SN 2001el. We parameterize the toroid as the ring of a spherical shell lying within opening angle ψ (see Figure 4.4).

We first consider a system where the toroid is observed edge-on. We set $\psi = 30^\circ$, giving the minimal z-plane covering factor, and $\tau_1 = 5$. We orient the torus axis at $\gamma = 45^\circ$ to preferentially absorb the diagonal light. The results are shown in Figure 4.14. The flux feature is a good match to the double-dipped profile, but the polarization peak at 5% is much too large. The reason is clear from the slice plot in Figure 4.15 – the edge-on toroid, which occludes opposite sides of the photosphere, is very effective at blocking light of a particular polarization.

A good fit to the polarization feature can still be sought by changing the inclination of the toroid. As the inclination is increased, the toroid rotates off the photodisk and both the flux and polarization feature decrease. The boundaries of the toroid and the opening angle must then be readjusted to properly fit the flux feature. In the present model a perfect fit cannot be found for any inclination. For all cases where the flux feature is well fit, the polarization feature is too strong – a compromise fit is shown in Figure 4.16.

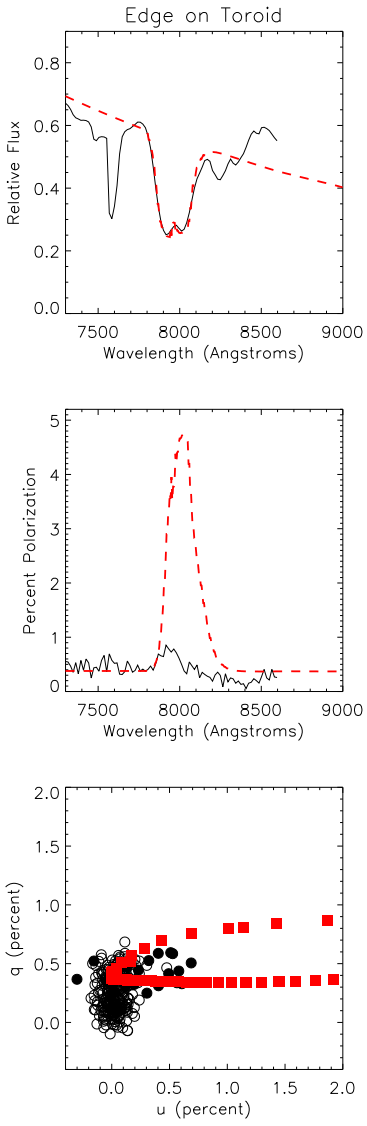

Figure 4.14 Synthetic spectrum fits to the HVM feature using the edge-on toroid geometry. Panels are the same as in figure 4.9. The polarization feature is much too strong.

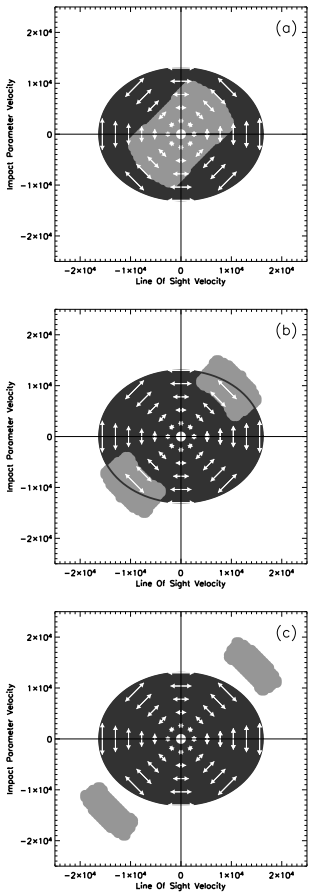

Figure 4.15 Three slices through the edge-on toroid HVM. Panels are the same as in Figure 4.10. Because the toroid is very effective in blocking light of a particular polarization, it will lead to large polarization peaks.

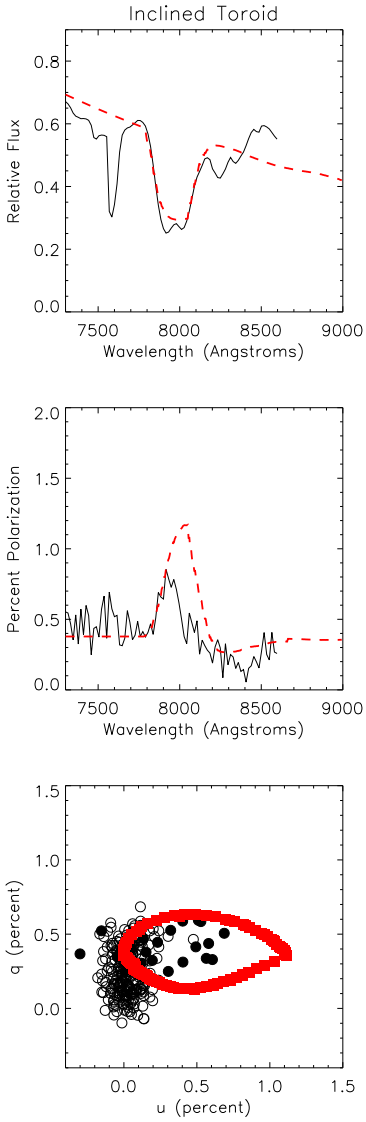

Figure 4.16 Synthetic spectrum fits to the HVM feature using the inclined toroid geometry. Panels are the same as in Figure 4.9. The polarization feature is still too strong, while the flux absorption is too weak.

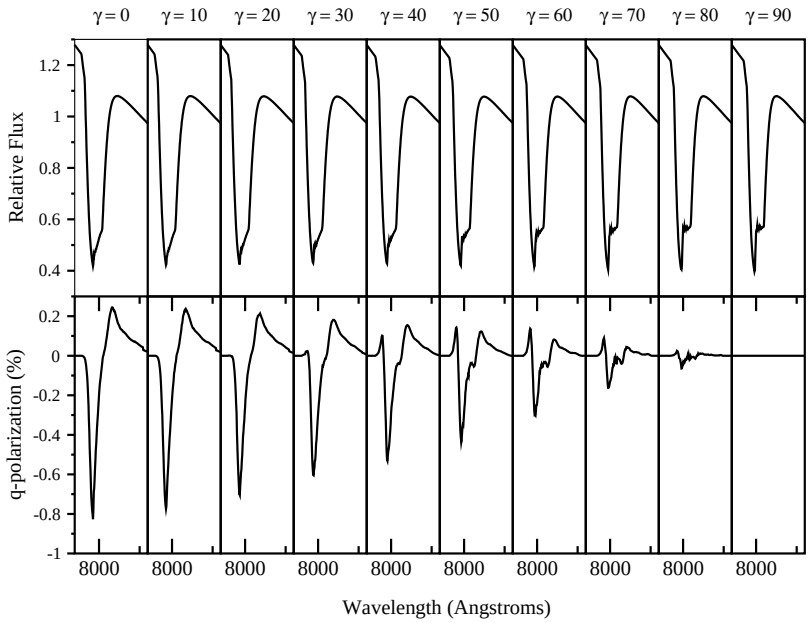

Figure 4.17 Line profile of the ellipsoidal shell model from various lines of sight. Positive (negative) q-polarization indicates vertically (horizontally) polarized light. An absorption feature is visible from all lines of sight.

4.5 The High Velocity Material from Other Lines of Sight

Our previous discussions have made it clear that several geometrical configurations are capable of providing reasonable fits to both the flux and polarization HVM features. The degeneracy problem is two-fold: (1) Different distributions of absorbing material in front of the photosphere can lead to similar polarization features (see the discussion in §4.3.3). (2) There is no strong diagnostic of the amount and distribution of material in the emission and occluded regions (§4.4.1). In this section we consider how the degeneracy problem can be overcome by future SN Ia observations that may probe the HVM from different lines of sight.

One difficulty in exploring line of sight variations is that the number of possible configurations in a two-axis system is enormous. Even holding the boundaries of the HVM

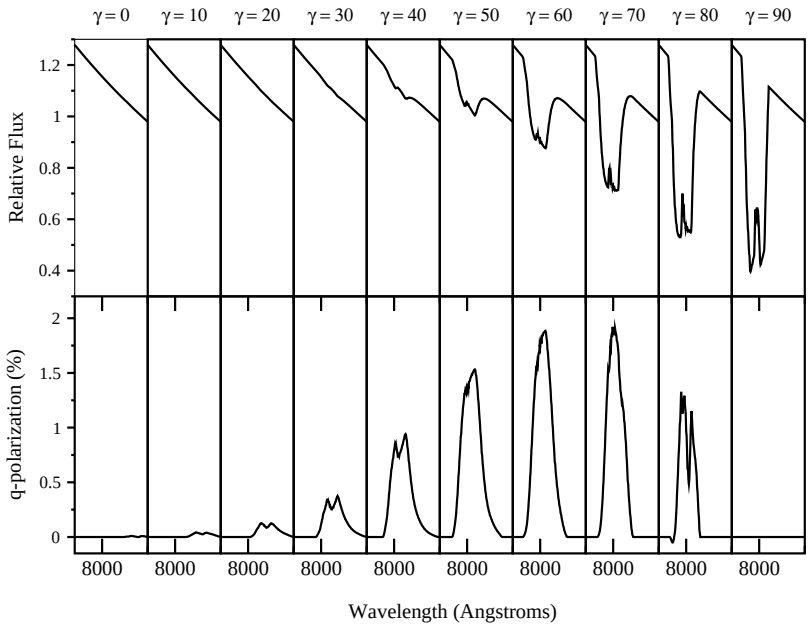

Figure 4.18 Line profile of the clumped shell model from various lines of sight. As the section moves to the edge of the disk, it blocks lower intensity, highly polarized edge light. The flux feature thus gets weaker while the polarization gets stronger. Note that for $\gamma = 40°$ the flux absorption is hardly visible while the polarization feature is strong.

fixed, we still have as free parameters the angle between the photosphere and HVM symmetry axis and two angles specifying the line of sight. There is no easy way to catalog all the possibilities. Therefore to keep the discussion simple and general, in the following calculations we choose the underlying photosphere to be spherical. The HVM axis can then be aligned in the $z - y$ plane (i.e., $\delta = 0°$), leaving as the only free parameter the inclination γ. The polarization is then in the q direction; we use the convention that a positive q-polarization indicates the net flux is vertically polarized, while a negative q-polarization indicates it is horizontally polarized.

The ellipsoidal shell shows only subtle variations with inclination (Figure 4.17). A flux absorption is visible from all lines of sight, with the absorption profile barely changing

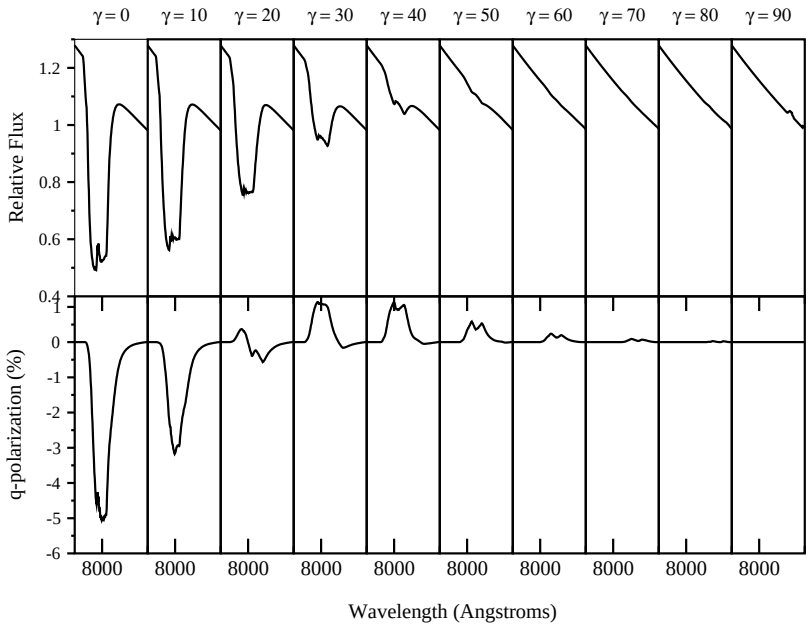

Figure 4.19 Line profile of the toroid model from various lines of sight.

with inclination. The only effect on the profile is a small shift of the minimum to the red as the short (i.e., slow) end of the shell moves into the line of sight. For $\gamma = 0°$ (shell viewed edge-on) the polarization is a maximum at 0.8%; this level is comparable to the HVM feature of SN 2001el. As γ is increased, the polarization feature decreases monotonically. For $\gamma = 90°$ (shell viewed pole-on) circular symmetry is recovered and the polarization is zero.

The clumped shell, on the other hand, shows strong variations with inclination (Figure 4.18). The flux absorption is deepest for $\gamma = 90°$, when the clump is viewed top-on, directly in between the photosphere and observer. At this inclination, the system is circularly symmetric and the polarization cancels (the *perfect* cancellation is of course the unnatural result of our simple "bowl-like" clump parameterization; a more irregularly shaped clump would show a small polarization feature). As γ is decreased, the clump moves to the edge of the photodisk, where it covers lower intensity, more highly polarized light. As

a result, the flux absorption gets weaker while the polarization feature becomes stronger. A strict inverse relationship holds for the inclinations $90^\circ - 70^\circ$ and provides an important signature for the single clump model. For inclinations smaller than 60° the polarization begins to decrease, but still remains much stronger than the flux feature. An especially striking signature occurs for the line of sight $\gamma = 40^\circ$. Here the flux feature is barely visible while the polarization feature is strong ($\sim 1\%$). The observation of this type of feature would clearly rule out an ellipsoidal shell and favor a single clump HVM geometry.

The variety of possible flux profiles from the clumped shell model corresponds nicely to the variety of profiles that have already been observed in some other supernovae. As the inclination is decreased from 90°, the clump extends further in the z-direction – the two lines therefore become broader and the two minima more blended. When the clump is viewed directly on ($\gamma = 90^\circ$), the two minima are largely resolved, which is not unlike the feature in SN 2000cx (Li et al., 2001a). At slightly smaller inclinations ($\gamma \approx 80^\circ$) we found the best fits to the partially blended minima of SN 2001el. For $\gamma = 40^\circ$ the feature is weaker and the two minima are almost completely blended, resembling the rounded feature of SN 1990N. For $\gamma = 20^\circ$, the feature is very weak and about the depth that it was observed in SN 1994D. Thus the clumped shell may be a single model capable of reproducing the full range of available observations of the HVM flux feature. More observations are necessary, however, to determine if the variety of flux profiles is indeed a line of sight effect or rather represents individual differences in the high velocity ejecta.

The most obvious signature of the toroidal geometry (Figure 4.19) is the high levels of polarization ($\sim 5\%$) when viewed near edge-on ($\gamma = 0^\circ$). An edge-on toroid occludes vertically polarized light from the edges of the photosphere, giving a polarization feature with $q < 0$. As the toroid is inclined, the structure rotates off the photodisk and both the flux absorption and polarization peak weaken (in contrast to the clumped shell model). At inclinations greater than 20°, the toroid begins to occlude the horizontally polarized light from the bottom of the photosphere;q then flips sign and becomes positive.

4.6 Summary and Conclusions

The investigations presented in this chapter are some of the first to explore fully 3-D supernova geometries in detail, and to use the polarized line features to constrain the geometry of different components of the ejecta. They begin to hint at the sort of detailed geometrical information that may be extracted from high quality spectropolarimetric observations. Interpreting the polarization observations through modeling turns out to be a difficult endeavor, however, largely because of the the enormous number of configurations available in arbitrary 3-D geometries. A parameterized approach is therefore useful in understanding the general polarization signatures arising from different geometrical structures.

The models computed in this chapter highlight the wide range of spectropolarimetric features possible when aspherical geometries are considered. Depolarizing line opacity in the supernova atmosphere does not in general produce simple depolarization features in the polarization spectrum. Asymmetrically distributed line opacity often creates a polarization peak by partially obscuring the underlying photosphere. In systems where the line opacity follows a different axis of symmetry from the electron scattering medium, the resulting polarization feature generally creates a loop in the q-u plane. The two-component model described in this chapter provides a convenient approach for quickly calculating and gaining intuition into the types polarization features arising from partial obscuration.

For the case of the high velocity material in SNe Ia, partial obscuration is the dominant effect on the line polarization features, resulting in significant polarization peaks for practically any geometry considered. We have therefore explored to what extent partial obscuration alone can explain the Ca II IR triplet polarization peak in SN 2001el. Although a unique reconstruction of the ejecta geometry is not possible, we can rule out a spherical shell and find good fits with a clumpy structure.

In addition, we have shown how different HVM geometries can be clearly discriminated by observing them from varying lines of sight. Depending upon the HVM geometry, a flux absorption similar to that of SN 2001el will be observed in SNe Ia with different frequency. For a shell-like model, the flux signature will be observed from all lines of sight,

while for the toroid and clump, only a fraction of the lines of sight produce the signature absorption. Under the assumption that the HVM has a similar structure in all (or at least a known subset) of SNe Ia, it may be possible to constrain the geometry with a statistical sample of early flux spectra. Because the different models leave even more dramatic signatures on the polarization spectra, only a few well-observed supernovae like SN 2001el are needed to discriminate among the various scenarios (see §4.5).

Although more observations are necessary to pin down the exact geometry of the HVM, one can begin to speculate about its origin. Two questions in particular must be addressed: Why is the HVM feature geometrically detached from the photospheric material? Why does the HVM deviate from the dominant axis of symmetry of the photospheric material?

The detachment of the HVM indicates that the atmospheric conditions change rather suddenly at high velocity. Three possible changes (or a combination thereof) could result in an HVM feature (see Hatano et al., 1999): (1) A spike in the overall density in the HVM. (2) A spike in the calcium abundance. (3) A sudden change in the ionization/excitation of the calcium. The last of these may result from the decreasing temperatures in the outer layers of ejecta, which cause an increased recombination of Ca III to Ca II. However, it seems unlikely in this case that this optical depth spike would have sharp geometrical boundaries that persisted over several epochs of observations, as found for SN 2001el.

The distinct orientation of the HVM as compared to the photospheric material could be (1) the result of random processes in the explosion physics/hydrodynamics such as large scale clumpiness due to Rayleigh-Taylor instabilities, or a clumpy Ni^{56} distribution causing an irregular ionization of calcium, or (2) an indication of a preferred direction in the progenitor system; for example, the photospheric dominant axis could represent the rotation direction of the white dwarf, while the HVM axis could represent the orientation of an accretion disk.

A tantalizing possibility is that the HVM is related to a binary companion star, and that we may actually be seeing direct signatures of the SN Ia progenitor system. This

possibility has been explored by Gerardy et al. (2003) in their analysis of a similar Ca II IR triplet feature in SN 2003du. They show that in running into a low-density circumstellar environment, the outer layers of the supernova ejecta are decelerated into a dense outer shell, which can produce a HVM feature. Another possibility is that the supernova ejecta may strip some material as it impacts the companion star. According to the models of Marietta et al. (2000), some stripped material is ejected at high velocity, and is distributed primarily in the forward direction.

In addition to being a possible signature of a progenitor system, the HVM is an important source of observational diversity in SNe Ia. The high-velocity Ca II IR triplet absorption feature seen in SN 2001el decreases the observed I-band magnitude by $\sim$0.2 mag. In SN 2000cx, additional high-velocity features of Ti II and Fe II occurred in the middle of the B-band, leading Branch et al. (2004) to suggest that a gradual thinning of a high-velocity clump in SN 2000cx may explain the unusual, lopsided B-band light curve of this object. Note that the effect of the HVM on photometric measurements is closely tied to its geometry – for a spherical, pure scattering atmosphere, the flux absent in the P-Cygni absorption component exactly equals the added flux in the emission feature. Observed broad-band magnitudes should thus be relatively unchanged unless the HVM aspherical, in which case flux missing in the absorption feature will be lost to another line of sight. An increased understanding of the geometry of the high-velocity material is therefore relevant for the use of SNe Ia in cosmology.

Chapter 5

Could There Be a Hole in Type Ia Supernovae?

5.1 Introduction

Having discussed in Chapter 4 the geometry of the high velocity material in SNe Ia, we turn now to the shape of the bulk of the ejecta. We know that in SN 2001el and several other SNe Ia, the ejecta obeyed a nearly axial symmetry, as the polarization angle was fairly constant over the entire spectral range. Previous attempts at modeling the spectropolarimetry have been confined to ellipsoidal geometries (Jeffrey, 1991; Höflich, 1991; Wang et al., 1997; Howell et al., 2001). This shape might arise, for example, if the progenitor white dwarf was rapidly rotating.

Another potential cause of asymmetry in SNe Ia is the binary nature of the progenitor system. In the favored progenitor scenario (the *single-degenerate scenario*; see Branch et al. (1995) and references therein), SNe Ia arise from a white dwarf accreting material from a non-degenerate companion star. The companion may be either a main-sequence star, a red-giant, or a subgiant; as it is close enough to be in Roche-lobe overflow, it subtends a substantial solid angle from the perspective of the white dwarf. The supernova explosion

occurs when the white dwarf has accreted enough matter that the densities and temperatures at the center are sufficient to ignite carbon, just below the Chandrasekhar limit. The ejected supernova material moves at a few percent of the speed of light and soon after the explosion (from minutes to hours) engulfs the companion star. In the impact it would not be surprising if a substantial asymmetry were imprinted on the supernova ejecta.

The ejecta-companion interaction has been studied with two-dimensional hydrodynamical models by Fryxell & Arnett (1981), Livne et al. (1992), and most recently and extensively by Marietta et al. (2000). These studies were primarily concerned with the fate of the companion star, in particular how much hydrogen gets stripped from its outer envelope. Stripped hydrogen may appear as narrow Balmer emission lines in the supernova spectrum, which if observed might provide direct evidence of a binary progenitor system. With the advance of spectropolarimetric observations, however, the nature of SN Ia asphericity becomes another relevant test of the single-degenerate progenitor scenario. In their hydrodynamical models, Marietta et al. (2000) find that the impact with the companion star carves out a conical hole in the supernova ejecta. The opening angle of the hole is 30°-40°, and because the ejecta are moving supersonically, the authors claim that the hole does not close with time. The final configuration is axially symmetric, as was seen in the polarization observations of SN 2001el.

In this chapter we use radiative transfer calculations to address the possibility of SNe Ia having an ejecta hole asymmetry. We calculate the variation of the spectrum, luminosity, and polarization with viewing angle for the aspherical supernova near maximum light. In contrast to the ellipsoidal models, the angular variations in an ejecta-hole geometry can be rather extreme, especially when one looks near the hole itself. These variations would necessarily introduce some diversity into the observed properties of SNe Ia. The question is, exactly what sort of diversity arises in the ejecta-hole geometry, and does this fit in with the diversity already known to exist in SNe Ia?

While SNe Ia are considered to be a rather homogeneous class of objects, they do show some variety in their spectral and photometric properties. The observed peak magnitudes of SNe Ia vary by ~ 0.4 mag, and the luminosity is found to correlate with the width

of the light curve (Phillips, 1993). The spectra of SNe Ia can be classified as either normal or peculiar (Branch et al., 1993). The peculiar spectra have feature strengths at maximum light that differ from "normal" cases (such as SN 1981B), and are usually subdivided into two classes: SN 1991bg-like supernovae have a broad Ti II absorption trough not seen in the normal SNe Ia (Filippenko et al., 1992a); SN 1991T-like supernovae have weak or absent features from singly ionized species but noticeable Fe III lines (Filippenko et al., 1992b; Phillips et al., 1992; Jeffery et al., 1992). Not all supernovae fit cleanly into the classification scheme. In its pre-maximum spectra, SN 1999aa resembled SN 1991T, but by maximum light it had begun to look much more normal, with Si II and Ca II lines that were stronger than in SN 1991T but weaker than in normal SNe Ia(Li et al., 2001b). As such, SN 1999aa is considered by some to be an intermediate link between the normal and the SN 1991T-like SNe Ia. Other observations have uncovered singular objects like SN 2000cx (Li et al., 2001a) and SN 2002cx (Li et al., 2003), that while resembling SN 1991T in some ways (weak Si II, strong Fe III lines) showed other peculiarities that were unique. Additional spectral diversities include the abnormally high photospheric velocities of SN 1984A (Branch, 1987) and the detached, high velocity features seen in several supernovae (Hatano et al., 1999; Wang et al., 2003a; Thomas et al., 2004). The diversity of SNe Ia is thus multi-faceted, a point we return to in the conclusion.

5.2 The Ejecta-Hole Model

The ejecta model used in the calculations is based on the spherical W7 explosion model (Nomoto et al., 1984), which has often been used in spherical radiative transfer calculations to model the spectra of normal SNe Ia (Lentz et al., 2001; Jeffery et al., 1992; Nugent et al., 1997). The composition structure of W7 consists of an inner ^{56}Ni zone ($3000 < v < 9000$ km s^{-1}), a middle zone of intermediate-mass elements (9000 km s^{-1}$< v <$ 15,000 km s^{-1}), and an outer unburned region of carbon-oxygen rich material ($v > 15,000$ km s^{-1}). In our calculations we found it necessary to make one adjustment to the compositions: to reproduce the depth and width of the Ca II H&K feature in a normal SN Ia, we needed to

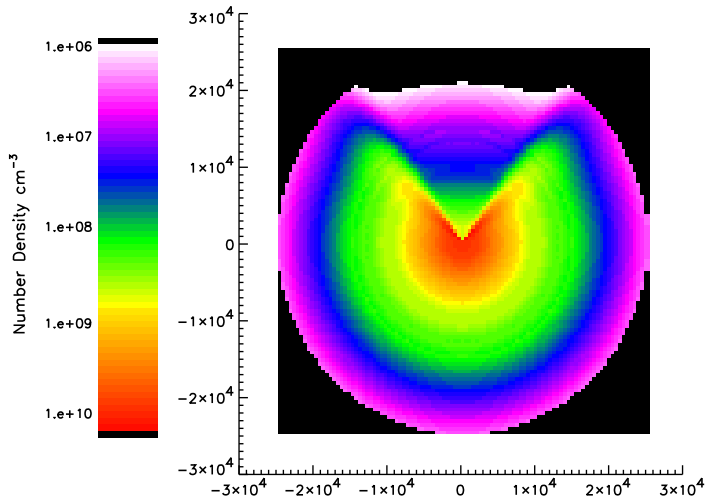

Figure 5.1 Density structure of the ejecta-hole model near maximum light (20 days after explosion).

increase the calcium abundance by a factor of 10 in the outer C-O region. The difficulty W7 has in fitting the Ca II H&K feature has already been noted by Lentz et al. (2001) in the context of detailed NLTE models. The lack of burned material above 15,000 km s^{-1} may indicate a weakness of the parameterized deflagration explosion model used.

To introduce an ejecta hole into the spherical model, we describe the density structure by an analytic function that in the radial direction well reproduces W7:

$$\rho(v, \theta) = \rho_0 \exp(-v/v_e) F(\theta), \tag{5.1}$$

where $v_e = 2,500$ km s^{-1} and ρ_0 is set by the condition that the total mass of the ejecta equals a Chandrasekhar mass. $F(\theta)$ is an angular density variation function which would equal unity in a spherical model. For the ejecta-hole model, we use a constructed function which resembles the structure seen in the interaction models of Marietta et al. (2000). The conical hole has a half opening angle of $\theta_H = 40°$ and the density in the hole is a factor $f_H = 0.05$ less than in the surrounding material. The material that is displaced from the

hole gets piled up into a density peak just outside the hole edge, with angular size $\theta_P = 20°$. The function invented to reproduce these features is

$$F(\theta) = f_H + (1 - f_H)\left(\frac{x^n}{1+x^n}\right)\left(1 + Ae^{-\left(\frac{\mu-\mu_H}{\mu_P}\right)^2}\right) \tag{5.2}$$

with

$$x = \frac{1-\mu}{\mu_H} \tag{5.3}$$

where $\mu = \cos\theta$ and $n = 8$. The constant A is set by the condition that the mass within a shell is equal to that in the spherical model (i.e., the integral of $F(\theta)$ over solid angle is equal to 4π). The density structure is shown in Figure 5.1.

This analytic function does not capture all the complexity present in a hydrodynamical model; for example, Marietta et al. (2000) point out that the opening angle of the hole is slightly smaller at high velocities than at low velocities ($\sim 30° - 35°$ as opposed to $40°$). Of course, the benefit of using a simple analytic function is that it isolates the essential geometrical consequences of a hole asymmetry; in addition, it allows us to test in a parameterized way how varying the ejecta-hole structure affects the observable signatures. Once the general ideas are understood, one can perform more specific calculations using hydrodynamical models spanning a wide range of initial progenitor conditions.

In the ejecta/companion interaction, as much as 0.1-0.5 $M_\odot$ of hydrogen rich material can be stripped and ejected from the companion star (Wheeler et al., 1975; Marietta et al., 2000). This material is not included in our calculations. The vast majority of the stripped material has low velocity ($v < 1000$ km s^{-1}) and sits at the center of the ejecta, where it will not affect the spectrum or polarization near maximum light. A small amount of stripped material may be ejected at high velocities, and could be related to the high-velocity spectral features discussed in Chapter 4.

5.3 Results

We have computed the gamma-ray deposition, optical spectrum, relative luminosity, and polarization of the ejecta-hole model near maximum light (20 days after the

explosion) as a function of the viewing angle θ. The models were calculated on a 2-D Cartesian grid of 10^4 cells using the Monte-Carlo code described in § 3. Because the current code is not time-dependent, we leave for future work the effect of the asymmetry on the light curve. For the maximum light model, the total luminosity used is $L = 1.4 \times 10^{43}$ ergs and the emission temperature $T_{bb} = 11,000$ K. We discuss the various results in turn.

5.3.1 Gamma-Ray Deposition

In the W7 explosion models, $\sim 0.6 M_\odot$ of radioactive ^{56}Ni is synthesized and will power the supernova luminosity. The majority of the decay energy from ^{56}Ni and its daughter ^{56}Co is released as gamma rays, which deposit their energy in the supernova ejecta primarily through Compton scattering. It takes only a few Compton scatterings for a gamma-ray to give up the majority of its energy to fast electrons, which are in turn assumed to be thermalized locally. We compute the gamma-ray energy deposition with a MC transfer routine that includes Compton and photo-electric opacities and also produces gamma-ray spectra.

In a spherical SN Ia model, the gamma-ray trapping is very effective at maximum light. In the inner ^{56}Ni zone, the mean free path to Compton scattering is only ∼300 km s^{-1} and so gamma-rays deposit energy nearly coincident to where they are created; only about 4% of the gamma-ray energy escapes the atmosphere. Inside an ejecta hole, on the other hand, the mean free path is 20 times greater due to the lower density. gamma-rays generated in the hole can therefore escape the atmosphere, at least those that are emitted in the outward direction. This energy loss is not very significant, however, as the hole is largely evacuated and contains less then 1% of the total ^{56}Ni mass. The material that has been displaced from the hole (containing ∼11% of the total ^{56}Ni mass) is piled up around the hole edges, where the density is high, and the gamma-ray trapping is even more efficient than in a spherical model. Thus we find the perhaps unexpected result that the ejecta hole actually slightly enhances the gamma-ray trapping at maximum light, from 96% to 97%.

Using "Arnett's law" as a rough rule of thumb (Arnett, 1982), the luminosity

of a SN Ia at maximum light should be comparable to the instantaneous rate of energy deposition. One therefore expects that in the ejecta-hole model the total luminosity at peak will be close to (perhaps slightly greater than) a spherical model. In other words, although the aspherical supernova will appear significantly dimmer or brighter depending upon the viewing angle (as we will see in § 5.3.4), the specific luminosity integrated over *all* viewing angles will not be entirely different from the spherical case. However, time-dependent calculations are needed to properly address this question, and so we leave it for future work.

5.3.2 The P-Cygni Profile

Line opacity in a spherical, expanding SN atmosphere gives rise to the well known P-Cygni profile – i.e., a blueshifted absorption trough with a redshifted emission peak. An ejecta-hole asymmetry dramatically alters the line profile from some lines of sight, as shown in Figure 5.2. The major effects are readily apparent: in the typical P-Cygni formation, material in front of the photosphere obscures the light below and gives rise to the blueshifted absorption feature. When one looks down the ejecta hole ($\theta < \theta_H$), the density of this obscuring material is much lower and the line absorption features are thus much weaker. There is little change, however, in the redshifted emission component. Thomas et al. (2002) have pointed out that asymmetries have the most dramatic effect on absorption features, as the absorption depth is related directly to how much of the photosphere is covered by line opacity.

As one looks away from the hole, the line absorption depth increases rapidly, until for $\theta > \theta_H$ the depth is equal to that of the spherical model. For side-on views ($\theta \approx 90°$), the hole is in the emission region – because some emitting material is then lacking one expects the P-Cygni emission feature to be depressed near the line wavelength center. The missing material, however, amounts to only 11% of the total emitting area, so the effect is hardly noticeable. For $\theta > \theta_H$, the line profile changes very little with viewing angle.

The minima of the absorption features are also less blueshifted when viewed down

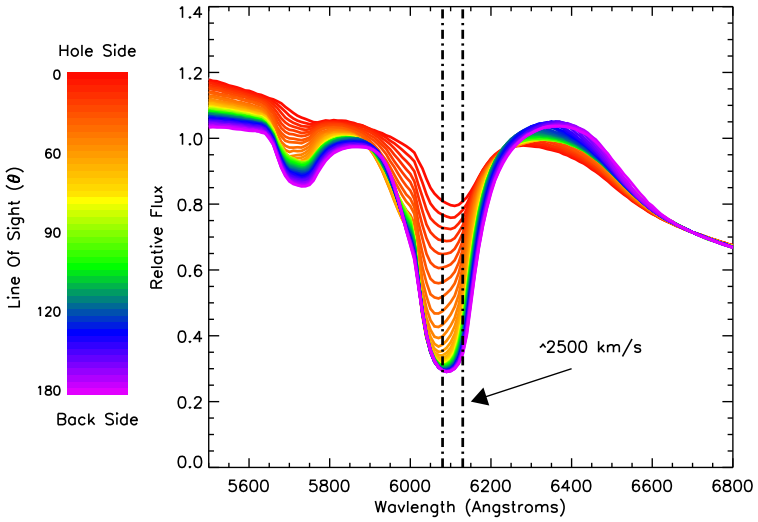

Figure 5.2 Flux profile of the Si II 6150 line (at maximum light) from various viewing angles (the view down the hole is the top-most spectrum). When viewed down the hole ($\theta = 0°$) the absorption trough is weaker and has a lower velocity by $\sim 2,500$ km s^{-1}. Silicon is the only species included in this calculation.

the hole, by about 2000-3000 km s^{-1}. This is because the hole allows one to see relatively deeper into the ejecta. In a spherical model, P-Cygni features are formed primarily by material at or above the supernova photosphere, while layers below will not be visible until the expanding supernova thins out and the photosphere recedes. For views down the ejecta hole, however, the electron scattering photosphere has an odd shape, resembling the conical hole of Figure 5.1. As radiation streams radially out of the hole, absorption features are caused by relatively deeper layers of ejecta. This deeper material will tend to be hotter, more ionized and perhaps of a different composition than the material in the outer layers. One therefore expects that the features of more highly ionized species will be relatively more prominent when the supernova is viewed down the hole. The exact line strengths depend, of course, upon the temperature and ionization structure in the 2-D atmosphere, which are

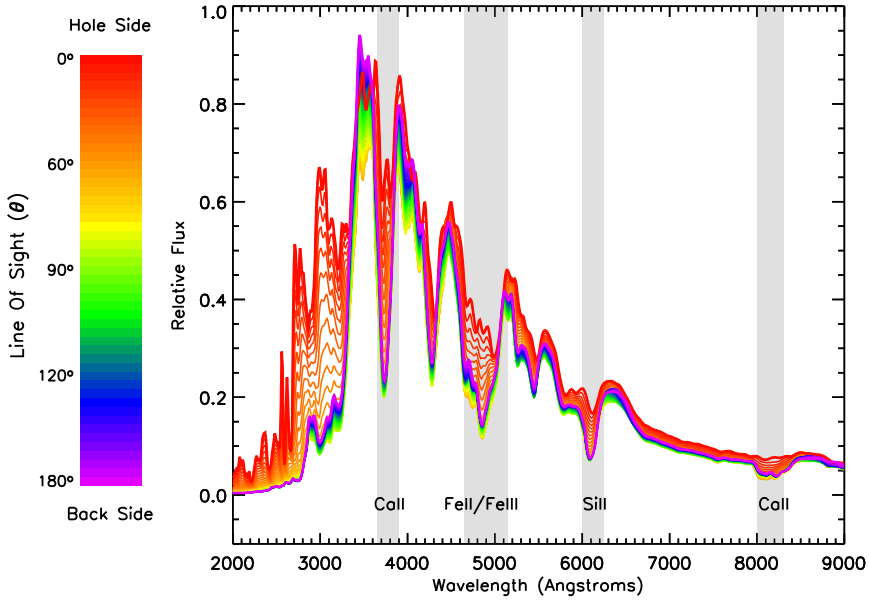

Figure 5.3 Spectrum of the ejecta-hole model near maximum light from various viewing angles (the view down the hole is the top-most spectrum). Some important line features are highlighted.

calculated self-consistently in LTE in our models.

5.3.3 Spectrum Near Maximum Light

In sum, the spectrum in the ejecta-hole model will look the same as in a spherical model for all lines of sight *except* when one looks almost directly down the hole ($\theta < \theta_H$). In the latter case, one sees a peculiar spectrum characterized by more highly ionized species, weaker absorption features, and lower absorption velocities. We show the variation of the maximum light spectrum with viewing angle in Figure 5.3. Notice in particular the dramatic effect the hole has on the Si II and Ca II features, the iron blend near 5000 Å, and the UV region of the spectrum ($\lambda < 3500$ Å).

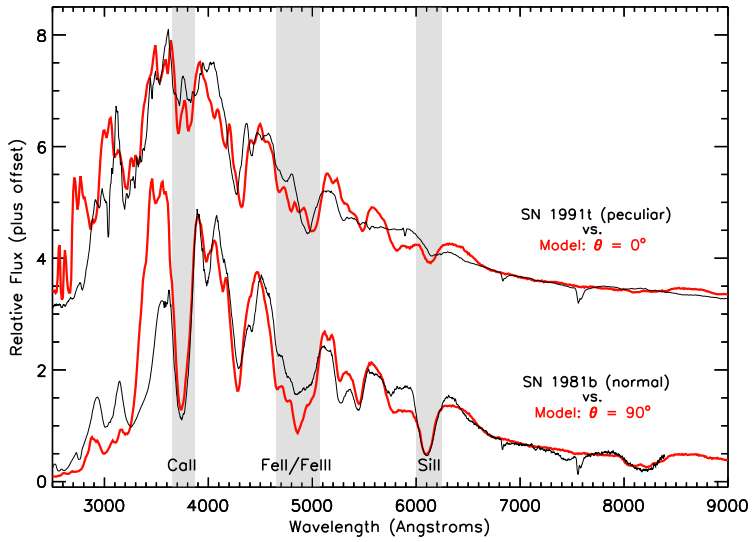

Figure 5.4 The maximum light spectra of the ejecta-hole model (thick red lines) from two different viewing angles are compared to two observed SNe Ia (thin black lines). Bottom: the view from the side ($\theta = 90°$) compared to the normal SN 1981B. Top: the view down the hole ($\theta = 0°$) compared to the peculiar SN 1991T.

Figure 5.4 compares the model spectra to two well-known SNe Ia. The view away from the hole ($\theta = 90°$) resembles the normal Type Ia SN 1981B. The model reproduces most of the major spectral features, although there are a few discrepancies. The most obvious is that the flux peak near 3500 Å is much too large in the model. Because the opacity at this wavelength is largely due to Co II lines, models which mix some ^{56}Ni out to higher velocities can suppress the peak (Branch et al., 1985; Jeffery et al., 1992). The poor match is also likely in part due to the approximate treatment of wavelength redistribution in our calculations (a constant $\epsilon = 0.05$, two-level atom).

The spectrum down the hole ($\theta = 0°$) is clearly very different from a normal SN Ia. We compare it to the peculiar SN 1991T, which it resembles in the following ways: (1) the Si II absorption near 6150 Å is weak and has an unusually low velocity ($v \approx 10,000$ km s^{-1});

in addition, the Si II absorption at 4000 Å is absent. (2) The Ca II H&K feature is weak and shows a "split" into two lines (due to Ca II H&K and Si II λ3858; Nugent et al. (1997)); in addition, the Ca II IR triplet absorption is absent. (3) In the iron blend near 5000 Å, the broad Fe II absorption is weak while the sharper Fe III feature to the red is prominent. (4) The ultraviolet portion of the spectrum (2500 Å$< \lambda <$ 3500 Å) is much brighter down the hole, due to the decreased line blocking.

For now, the comparison of Figure 5.4 is meant only to illustrate that the spectrum emanating from the hole would be categorized as having so-called SN 1991T-like peculiarities. What connection, if any, the hole asymmetry may have to SN 1991T itself will be discussed further in the conclusions. Note that there are also apparent differences between SN 1991T and the model, among them: (1) The S II "W-feature" near 5500 Å is weak but visible in the model, whereas no clear feature is seen in SN 1991T; (2) The model has too much emission in the Si II 6150 and Ca II IR triplet features. (3) The velocities of the Fe III lines are too low in the model, by about 2000 km s^{-1}. The Fe III lines are forming just at the edge of the exposed iron/nickel core, so an explosion model that had a slightly larger ^{56}Ni zone than W7 might provide a better match to SN 1991T.

As can be seen in Figure 5.3, the spectrum changes continuously from peculiar to normal as the viewing angle is increased from zero. Some degree of peculiarity is seen for $\theta < \theta_H$, but the farther the viewing angle is from 0°, the less intense the peculiarities. For a viewing angle of $\theta_H \approx 30°$, for instance, the depths of the Si II and Ca II features are about half that of the normal case, and the iron blend near 5000 Å is dominated by Fe II rather than Fe III. One might rather compare the model from this viewing angle to SN 1999aa, which near maximum light was in many ways intermediate between SN 1991T and a normal SN Ia.

We have also experimented with varying the density structure of the ejecta hole. As can be expected, increasing the density in the hole or decreasing the hole opening angle tames the asymmetry and produces spectra with less intense peculiarities. A slight modification of these parameters (e.g., decreasing θ_H to 35° or doubling f_H to 0.1) has little effect on the flux spectra. However, if the hole opening angle is reduced below $\theta_H \lesssim 20°$

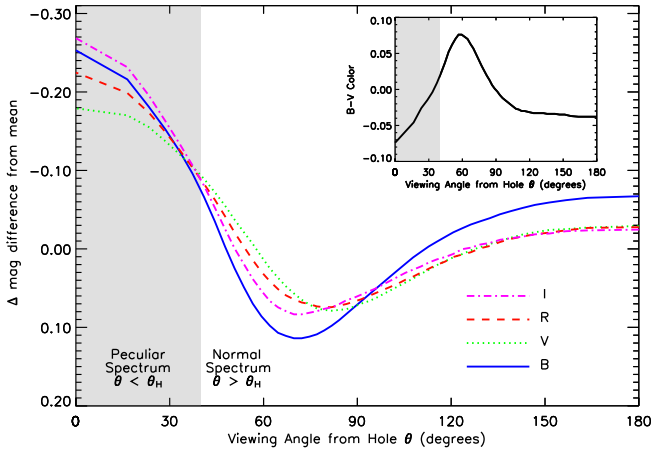

Figure 5.5 Variation with viewing angle of the B, V, R and I-band magnitudes of the ejecta-hole model near maximum light. The magnitudes are plotted relative to the mean magnitude averaged over all viewing angles. The inset shows the variation of the B-V color.

or the relative density in the hole increased above $f_H \gtrsim 0.3$, the spectral peculiarities begin to disappear and the spectrum shows very little variation with viewing angle. In the hydrodynamical models of Marietta et al. (2000), the hole opening angle is 40° in the low-velocity layers, and $30° - 35°$ in the outer high-velocity layers, depending upon the nature of the companion star. The hole used in Figures 5.3 and 5.4 ($\theta_H = 40°$ in all layers) thus represents the extreme end of what one might expect from their calculations.

5.3.4 Peak Magnitudes

In the ejecta-hole model, the observed luminosity depends upon the viewing angle (Figure 5.5). When viewed down the hole, the supernova is brighter by up to 0.25 mag in B. This is because photons more readily escape out of the hole due to the lower opacities. On the other hand, the supernova is dimmer than average when viewed from the side ($\theta \approx 90°$) because from this angle the supernova is lacking a "wedge" of scattering material

(see Figure 5.8a). Radiation that would normally have been scattered into the 90° view now flows straight out the hole and goes into making the view down the hole brighter.

It is widely believed that observed SN 1991T-like supernovae are in general overluminous, although the degree and regularity of this overluminosity can be questioned (Saha et al., 2001). While Figure 5.5 suggests a similar relationship, keep in mind that the total luminosity is a fixed parameter in this calculation – the figure only shows how this fixed luminosity gets distributed among the various viewing angles. In general, one expects the total luminosity to depend predominately on the amount of ^{56}Ni synthesized in the explosion, which will vary from supernova to supernova. If a certain SN Ia has a very small ^{56}Ni mass, for example, then although the view down the hole is the brightest of all possible viewing angles, the supernova would still appear underluminous compared to a SN Ia with normal ^{56}Ni production.

The total dispersion about the mean in the ejecta hole model is ~ 0.1 mag in V and R, and somewhat larger in B (~ 0.2 mag) as a result of the B-band's greater sensitivity to line opacity. The observed dispersion in SN Ia peak magnitudes is around 0.4 mag in the B-band, and the brightness is found to correlate with the width of the light curve (Phillips, 1993). These variations are believed to be largely the result of varying amounts of ^{56}Ni synthesized in the explosion. After correction for the width-luminosity relation and dust extinction (using the B-V color), the observed dispersion is reduced to $\sim 0.15 - 0.2$ mag (Riess et al., 1995, 1996; Hamuy et al., 1996). Some of this so-called intrinsic dispersion is likely due to an asymmetry of some sort; Figure 5.5 suggests that in the particular case of an ejecta-hole geometry, the asymmetry may in fact be the dominant effect. Note, however, that in the model the B-V color roughly correlates with peak magnitude – thus correcting for dust extinction with a B-V color will tend to correct for the asymmetry also. The angular variation of the luminosity is also sensitive to the details of the hole structure – decreasing the hole size to $\theta_H = 30°$, for example, decreases the B-band dispersion to $\sim$0.1 mag.

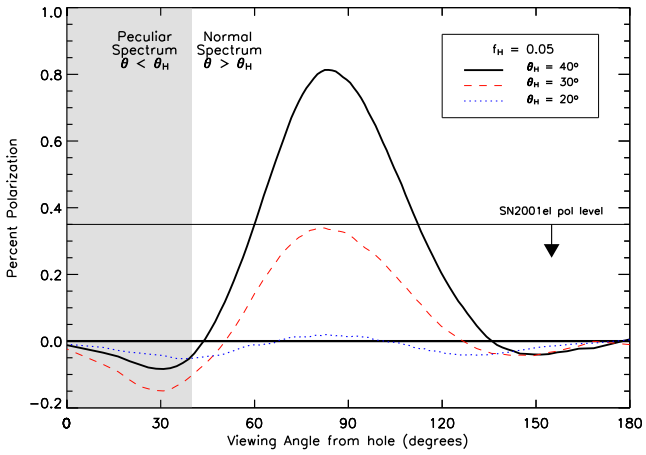

Figure 5.6 Continuum polarization of the ejecta-hole model near maximum light as a function of viewing angle. The solid line is the model used throughout the chapter, while the dashed and dotted lines are models where the hole opening angle has been reduced to 30° and 20°, respectively. The density of the hole is $f_H = 0.05$ in all cases.

5.3.5 Continuum Polarization

The polarization is the most direct indication of asymmetry in the ejecta. Because a spherically symmetric atmosphere has no preferred direction, the polarization integrated over the projected supernova surface must cancel. In an axially symmetric geometry, the net polarization can be non-zero and will align either parallel or perpendicular to the axis of symmetry. We use the convention that positive (negative) polarization designates a polarization oriented parallel (perpendicular) to the axis of symmetry. SN 2001el had a well-defined polarization angle over most of the spectral features, which indicates that the bulk of the ejecta obeyed a near axial symmetry (in addition, SN 2001el showed an unusual high velocity Ca II IR triple feature with a distinct polarization angle, corresponding to a detached "clump" of material that deviated from the dominant axis of symmetry, see Chapter 4).

Light becomes polarized in supernova atmospheres due to electron scattering; other

sources of opacity, such as bound-bound line transitions, are usually considered to be depolarizing. We define the continuum polarization as the polarization computed using only electron scattering opacity – this is most closely realized in the red end of a supernova spectrum (say, near 7000 Å), where there is not much line opacity. However this may not be the maximum polarization level in the spectrum, as line opacity may partially obscure the underlying photosphere and lead to a less effective cancellation of the polarization in the line features; see § 5.3.6 and Kasen et al. (2003b). Höflich (1991) computes the continuum polarization in ellipsoidal and other axially symmetric geometries.

Figure 5.6 shows the continuum polarization of the ejecta-hole model as a function of viewing angle. When viewed directly down the hole ($\theta = 0°$) the projection of the supernova atmosphere is circularly symmetric and the polarization cancels. As the viewing angle is inclined, the polarization increases, reaching a maximum when the supernova is viewed nearly side-on ($\theta \approx 90°$). The origin of the non-zero polarization is clear from Figure 5.8a. At inclinations near 90°, the hole removes a "wedge" of scatterers from the top of the atmosphere, which decreases the horizontally polarized flux coming from this region. The vertically polarized flux thus exceeds the horizontal; the net polarization is non-zero and aligned with the symmetry axis of the system (positive according to our convention).

To determine the level of intrinsic continuum polarization in an observed supernova, one must wrestle with the issue of subtracting the interstellar polarization (Howell et al., 2001; Leonard et al., 2000a). Once this is done, the observed levels are found to be rather small: the polarization of SN 2001el near maximum light was ∼0.3%; the polarization of the subluminous SN 1999by was ∼ 0.7%. For several other SNe Ia, no polarization signal was detected, but upper limits of 0.3-0.5% can be derived (Wang et al., 1996a,b). In the ejecta-hole model, the continuum polarization can be as large as 0.8%, while the polarization at the line features can be even larger (see next section). The hole asymmetry therefore produces polarization levels in the right range, though perhaps generally too high compared to the current published observations.

The polarization in the ejecta-hole model, however, is rather sensitive to the size and density of the hole. To demonstrate this we have over-plotted in Figure 5.6 the con-

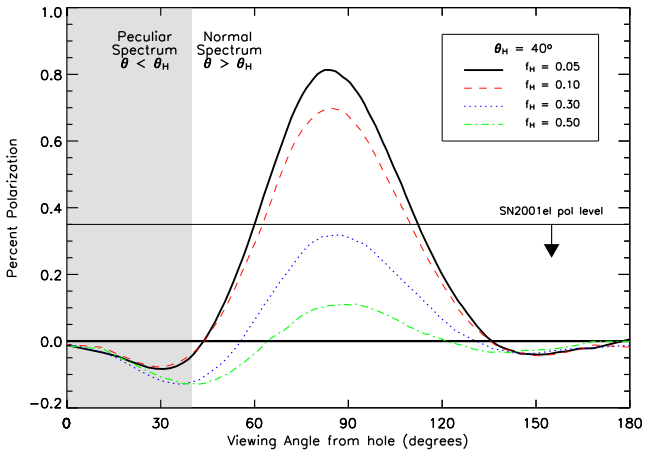

Figure 5.7 Dependence of the continuum polarization on the ratio of the density in the hole to that of the surrounding atmosphere. The solid black line is the model used throughout the chapter ($f_H = 0.05$), while the other lines show the effect of an increased relative density in the hole.

tinuum polarization of a model with a smaller opening angle ($\theta_H = 30°$). This tames the asymmetry and decreases the continuum polarization by more than a factor of two. If the hole size is decreased further to $\theta_H < 20°$, the continuum polarization level is uninterestingly small ($\lesssim 0.1\%$) from all inclinations. Figure 5.7 shows that the polarization also decreases as the relative density in the hole is increased, becoming uninterestingly small for $f_H > 0.5$. Thus the exact polarization level will depend upon the hole structure, which in turn depends upon the details of the progenitor system and hydrodynamics. In general, the more extreme the asymmetry of the hole (i.e., the larger and more evacuated it is), the higher the average polarization level. A larger sample of SN Ia spectropolarimetry could therefore put constraints on the size of a putative hole. Current observations may already constrain the hole to have $\theta_H \lesssim 40°$.

One correlation to keep in mind is that the continuum polarization is always relatively small ($\lesssim 0.1\%$) for views near the hole where the spectrum looks peculiar. For views

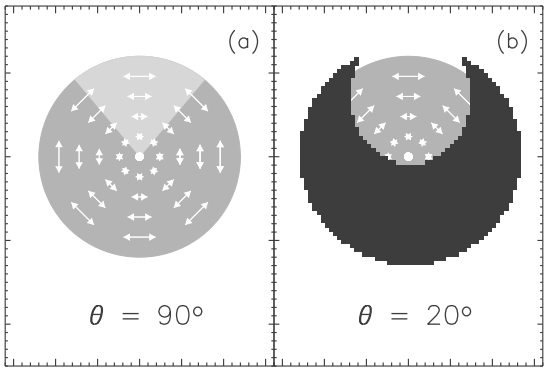

Figure 5.8 Schematic diagram which helps explain the polarization in the ejecta-hole model. (a) When viewed from the side ($\theta \approx 90°$) the top of the atmosphere is lacking a wedge of scatterers. The vertically polarized flux thus exceeds the horizontal and the continuum polarization is positive. (b) When viewed just off the hole axis ($\theta \approx 20°$), the line opacity on the planar surface corresponding to a certain line of sight blueshift (shown in black) only partially covers the photosphere. Because of the hole, horizontally polarized flux from the top of the atmosphere is relatively unobscured by the line and will cause the negatively polarized line peaks.

away from the hole, the continuum polarization may be either small or large. However, the continuum polarization is not the whole story, and as we will see in the next section, the polarization over the line features can be substantial even for $\theta < \theta_H$.

5.3.6 Polarization Spectrum

The continuum polarization level actually provides very little information about the nature of the ejecta asymmetry, as very different configurations can give the same numerical value. Line features in the polarization spectrum, on the other hand, contain more potential information about the specific geometry. We find that the ejecta-hole model has

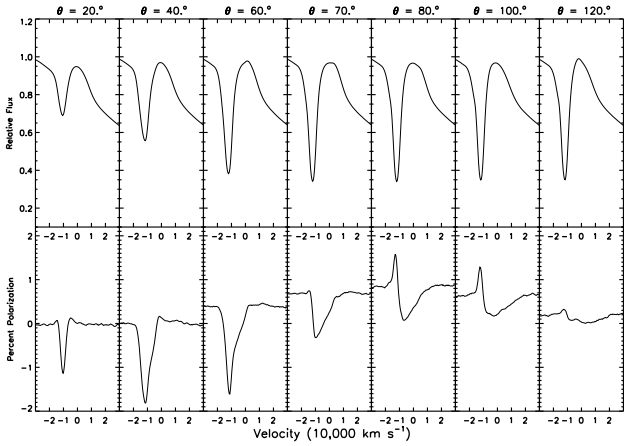

Figure 5.9 Flux and polarization profiles of a single unblended line in the ejecta-hole geometry from various viewing angles. The polarization feature is a negative (i.e., horizontally polarized) peak for ($10^\circ < \theta < 60^\circ$) and an inverted P-Cygni profile for ($\theta > 80^\circ$).

spectropolarimetric signatures that distinguish it from, for example, an ellipsoidal geometry.

The polarization spectrum in the ellipsoidal geometry has been studied in detail (Jeffrey, 1989; Höflich et al., 1996). In ellipsoidal models, the polarization level generally increases from blue to red due to the greater amount of depolarizing line opacity in the blue. Individual lines create "inverted P-Cygni" profiles in the polarization spectrum, i.e. a blueshifted polarization peak with a redshifted depolarization trough. The blueshifted peak is a result of the line opacity preferentially blocking the lowly polarized central photospheric light, while the redshifted trough is the result of unpolarized line emission light diluting the continuum polarization. The polarized line profiles look fairly similar from all viewing angles.

The line polarization profile in the ejecta-hole model shows an interesting variation with inclination (Figure 5.9). For views far enough away from the hole ($\theta \gtrsim 80^\circ$), the profile is an inverted P-Cygni, just as in an ellipsoidal model, and for essentially the same reason. For views closer to the hole, however, the blueshifted line absorption gives rise to a

large polarization peak (recall the negative sign indicates that the polarization direction is perpendicular to the symmetry axis of the system). Figure 5.8b helps explain the origin of the peak. From viewing angles near the hole axis, the projected electron scattering medium is fairly symmetric and the continuum polarization integrated over the ejecta surface nearly cancels. The line opacity, however, only partially obscures the underlying light. Because of the hole, horizontally polarized flux from the top of the atmosphere is relatively unobscured, whereas the vertically polarized light from the sides of the atmosphere is effectively screened by the line. The polarization over the line therefore does not cancel, but will be large and oriented perpendicular to the axis of symmetry (negative according to our convention). Note that if the hole opening angle is narrowed to $\theta = 30^\circ$, the line is even more effective in screening off all but the horizontally polarized light. The line polarization peak is therefore *larger*. Thus, while the continuum polarization decreases with decreasing hole size, the line polarization from certain viewing angles will be relatively large ($\gtrsim 1.0\%$) regardless of how big the hole is.

Figure 5.10 shows the entire ejecta-hole polarization spectrum from two lines of sight. For a view near the hole ($\theta = 20^\circ$) the spectrum is "line peak-dominated" – the continuum polarization is rather low, but large polarization peaks are associated with the blueshifted line absorption features (in particular the Si II 6150 Å feature and the Ca II IR triplet). This spectrum is qualitatively different from what is expected in an ellipsoidal geometry. For views away from the hole ($\theta = 90^\circ$), on the other hand, the polarization spectrum would be very hard to distinguish from the ellipsoidal case. The level of polarization rises from blue to red and the line features due to Si II 6150 Å feature and Ca II IR triplet have the "inverted P-Cygni" profile. The shape of the polarization spectrum from these angles resembles that of SN 2001el, although the polarization level is too high unless $\theta \gtrsim 110^\circ$, or unless the hole opening angle is reduced.

To discriminate between different geometries, a larger sample of polarization spectra is needed. If the asymmetry in SNe Ia is an ejecta hole, we would expect to see something like a line-peak dominated polarization spectrum for $10^\circ \lesssim \theta \lesssim 60^\circ$, or about 25% of the time. Such a polarization spectrum has not been observed as yet, but the number

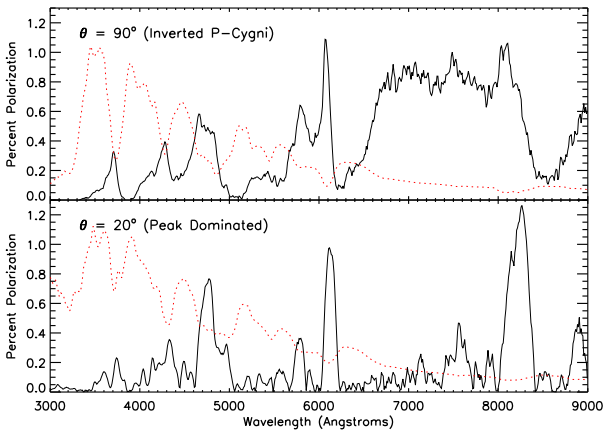

Figure 5.10 Polarization spectrum of the ejecta-hole model near maximum light for two viewing angles. We plot the absolute value of the polarization (solid lines), and for reference overlay the flux spectrum (dotted lines). The small-scale wiggles in the polarization spectrum are Monte Carlo noise, which increases to the red due to the lower fluxes. Top: for views away from the hole (here $\theta = 90°$) the spectrum resembles that of an ellipsoidal geometry with "inverted P-Cygni" line profiles. Bottom: for views nearer the hole (here $\theta = 20°$), the spectrum is "peak-dominated" with a low continuum polarization but substantial line peaks.

of published spectropolarimetric observations is still relatively small. Uncertainty in the interstellar polarization may make it difficult to identify the peaks, for if the zero-point of the intrinsic supernova polarization is unknown, it will be unclear whether features in the polarization spectrum are peaks or troughs. Therefore multi-epoch spectropolarimetric observations are necessary to help pin down the interstellar component. Of course, observing a line peak dominated polarization spectrum may not uniquely implicate an ejecta hole, as large line peaks could potentially occur in other geometries so far unexplored.

5.4 Conclusions

5.4.1 Asymmetry and Diversity in SNe Ia

Despite the seemingly extreme nature of an ejecta-hole asymmetry, we find that the geometry is actually consistent with what is currently known about SNe Ia, at least for the observables we have calculated. The variation of the peak magnitude with viewing angle is ~ 0.2 mag in B, comparable to the intrinsic dispersion of SNe Ia, and the level of polarization is in the range observed ($0 - 0.8\%$). The spectrum of the supernova looks peculiar when viewed near the hole, but this peculiarity may fit in with the spectral diversity already known to exist among SNe Ia. In addition, the polarization spectrum from some lines of sight is a qualitative match to that of SN 2001el.

An ejecta-hole asymmetry could therefore be one source of diversity in SNe Ia, but of course not the only one. The primary source of diversity in SNe Ia is thought to be due to variations in the amount of ^{56}Ni produced in the explosion. Because SNe Ia are powered by the radioactive decay of ^{56}Ni and its daughter ^{56}Co, different ^{56}Ni production can explain the variety in SN Ia peak magnitudes. Greater ^{56}Ni masses may lead to higher atmospheric temperatures and higher effective opacities, which may explain why brighter SNe Ia have broader light curves (Hoflich et al., 1995; Pinto & Eastman, 2000a; Nugent et al., 1997).

It has often been thought that the spectroscopic diversity of SNe Ia fits into the same one-parameter ^{56}Ni sequence (Nugent et al., 1995). In this picture, SN 1991T-like supernovae occupy the overluminous end of the sequence, where the larger ^{56}Ni mass leads to higher envelope temperatures and a higher ionization fraction. This may explain their peculiar spectral appearance (Mazzali et al., 1995; Jeffery et al., 1992). As the models in this chapter show, there could be a second, physically very different route to the same sort of spectral peculiarities – one could be peering down an ejecta hole. In this case, a high-temperature effect and a hole asymmetry may *both* be contributing to the sample of SN 1991T-like supernovae. In the ejecta-hole model, the spectrum shows some level of peculiarity for $\theta \lesssim \theta_H$ or about 12% of the time, although the peculiarities will only be

very intense for views more directly down the hole ($\theta \lesssim \theta_H/2$ or $\sim 3\%$ of the time). The observed rate of SN 1991T-like supernovae is $\sim 3-5\%$ in the samples of both Branch (2001) and Li et al. (2001b); the rate of SN 1991T/SN 1999aa-like supernovae is $20\% \pm 7\%$ in the Li et al. (2001b) sample. Therefore it is possible that a substantial percentage of these peculiar supernovae could be the result of an ejecta-hole asymmetry.

In this chapter we have chosen to compare the spectra emanating from the hole with SN 1991T only because it is the well-known prototype of a certain kind of spectral peculiarity. Whether SN 1991T itself was the result of looking down an ejecta hole is debatable. Initial estimates suggested that SN 1991T was as much as 0.7-0.8 magnitudes brighter in B than normal, which is too much to be explained by the asymmetry alone (Fisher et al., 1999). More recent Cepheid measurements of the distance to the host galaxy, however, show that SN 1991T was not really much brighter than a normal SN Ia. Saha et al. (2001) find a moderate overluminosity of 0.3 mag, although a value as high 0.6 mag cannot be ruled out due to a large uncertainty in the dust extinction. This lower value for the brightness of SN 1991T calls into question whether the peculiar spectral appearance can still be explained alone by high envelope temperatures due to a larger ^{56}Ni mass.

SN 1991T also had a rather broad light curve ($\Delta m_{15}= 0.95 \pm 0.05$ mag; Phillips et al., 1999), which is often taken as an indication of a large ^{56}Ni mass. Because we have not yet computed time-dependent models, we do not know exactly what effect an ejecta hole asymmetry will have on the light curve. Because the hole acts as an energy leak, it probably lowers the net diffusion time, and we expect that the *integrated* light curve (i.e., that summed over all viewing angles) will be narrower in an ejecta-hole model than a spherical model. But the real question relevant to SN 1991T is not how the integrated light curve compares to a spherical model, but whether the light curve viewed down the hole is broader or narrower than that from other viewing angles. In other words we need to know how Figure 5.5 – the distribution of the total luminosity among viewing angles – varies with time. This is more difficult to intuit, because as the ejecta thin out and the asymmetry and opacities evolve with time, it is hard to say off-hand whether it will become more or less easy for photons to preferentially escape out the hole. We leave the question

for future work.

In any case, although the prototype SN 1991T did have a broad light curve, it is not clear whether a general correlation between light curve width and SN 1991T-like spectral peculiarities even exists (Howell, 2004). Several SNe Ia have similar or broader light curves, and yet the spectrum is apparently normal – at least eight such supernovae with $\Delta m_{15} < 1.0$ are listed in Phillips et al. (1999), for example SN 1992bc ($\Delta m_{15} = 0.87 \pm 0.05$ mag) and SN 1994ae ($\Delta m_{15} = 0.86 \pm 0.05$ mag). SN 2001ay also had a normal spectrum but an exceptionally broad light curve ($\Delta m_{15} = 0.6$-0.7 mag; Phillips et al., 2003). Among the supernovae with SN 1991T-like spectral peculiarities, there also appears to be diversity. SN 1997br had a moderately broad light curve ($\Delta m_{15} = 1.00 \pm 0.15$ mag; Li et al., 1999), but the light curve of SN 2002cx was on the narrow side ($\Delta m_{15} = 1.30 \pm 0.09$ mag; Li et al., 2003). In another SN 1991T-like supernova the B-band light curve was lopsided – SN 2000cx brightened much faster than SN 1991T (resembling the rise of the normal SN 1994D) but the decline was slow ($\Delta m_{15} = 0.93 \pm 0.04$ mag; Li et al., 2001a). The examples make it clear that the connection between light-curve width and SN 1991T-like spectral peculiarities remains vague, and that more than one parameter of diversity needs to be identified.

The nebular spectra of SN 1991T may also suggest a large ^{56}Ni production. In the late-time spectra, the iron emission lines of SN 1991T have larger velocity widths than in most SNe Ia (Mazzali et al., 1998). Assuming the late time ionization/excitation conditions are similar in all SNe Ia, this implies that the nickel/iron core in SN 1991T is larger than normal. Confusing this conclusion, however, is the fact pointed out by Hatano et al. (2002) that the Si II velocities in the post-maximum spectra are among the *lowest* of all SNe Ia. If SN 1991T really did have a large inner ^{56}Ni zone, one naively expects the zone of silicon and other intermediate mass elements to occur at especially high velocities (as for instance in the delayed detonation models of Höflich et al., 2002). To account for the low Si II velocities, some have invoked a late-detonation model for SN 1991T, which produces a layer of intermediate mass elements sandwiched between two nickel zones (Yamaoka et al., 1992; Ruiz-Lapuente et al., 1992). Of course a lower Si II velocity is also naturally expected if

one is looking down an ejecta hole.

It is possible that SN 1991T did have a relatively large ^{56}Ni mass, rather than (or perhaps in addition to) being viewed down the ejecta hole. However, among other supernovae with SN 1991T-like peculiarities there is a good deal of diversity, and the large ^{56}Ni mass explanation will not apply in all cases. The most obvious case in point is SN 2002cx (Li et al., 2003). The spectrum of SN 2002cx resembled SN 1991T in that Si II, S II, and Ca II lines were weak, while Fe III was prominent, but the supernova was *underluminous* by ~ 2 mag. The velocities of the absorption features were also unusually low ($v \approx 7000$ km s^{-1}; Branch, 2004). The singularity of the supernova led Li et al. (2003) to consider alternative progenitor systems, although they conclude that no existing theoretical model can explain all the peculiarities. On the other hand, there is also the possibility that we are seeing multiple channels of diversity operating at once – one scenario to entertain now is that we are looking down the ejecta hole of a "weak" supernova that produced a small mass of ^{56}Ni. Such underluminous objects (e.g., SN 1991bg) typically have relatively low absorption velocities (Turatto et al., 1996; Mazzali et al., 1997; Hatano et al., 2002) which would be further reduced by looking down the hole. Despite the low luminosity, the spectrum might still appear hot and iron dominated if one is peering into the deeper layers, and (eventually) into the iron core. Of course, the chance of seeing two distinct sources of diversity operating at once would be, like SN 2002cx, a very rare occurrence.

Whatever the final explanation for SN 2002cx, its singularity highlights the fact that the diversity of SNe Ia is more complicated than a one-parameter sequence based upon ^{56}Ni. Because several observations require us to identify additional sources of variation, an ejecta hole becomes as an intriguing possibility to consider.

5.4.2 Observational Consequences of an Ejecta Hole

The results of this chapter suggest a few observational signatures of the ejecta-hole geometry. First, the continuum polarization should be low for views directly down the hole, where the spectrum looks peculiar. However, because of the partial obscuration effect, the

polarization spectrum should show large line peaks for views just away from the hole ($10^\circ < \theta < 60^\circ$), where the spectrum looks marginally peculiar or normal. For views from the side ($\theta \approx 90^\circ$), a relatively high continuum polarization should be correlated with a slightly dimmer supernova with normal spectral features and inverted P-Cygni line polarization features. Another possible signature of the ejecta hole is "lopsided" P-Cygni flux profiles – the view down the hole weakens only the absorption, not the emission feature, so one could look for a weak (or absent) absorption associated with noticeable emission. The easiest place to look would be in the Si II 6150 Å and the Ca II IR triplet features of SN 1991T-like supernova. Unfortunately the relative strength of absorption to emission depends also on the line source function, which is determined by the detailed excitation conditions in the atmosphere. In general, because we recognize that an ejecta-hole asymmetry is only one of several possible sources of diversity in SNe Ia, it may be difficult to isolate the geometrical effects from the other variations that may be operating. The only hope is to collect a large sample of supernovae with well observed light curves, spectra, and polarization, so that one might try to pull out the different trends.

In our calculations we have used a parameterized hole (half opening angle 40°) in order to explore the essential observable consequences of the geometry. The next step is to address the same questions using specific hydrodynamical models representing a wide variety of progenitor configurations. The details of the progenitor system could potentially affect the size and shape of the hole. Marietta et al. (2000) compute interactions using main-sequence, subgiant, and red giant companions and note that the variation in the hole asymmetry is not large. This is because in all cases the companion star is near enough to have undergone Roche lobe overflow and always occupies a similar solid angle (the red giant is farther away but physically larger than a main sequence companion which is smaller but much closer). However, if the ratio of companion radius to separation distance is decreased for some reason, the size of the hole also decreases. A larger sample of spectropolarimetric observations will help determine if SNe Ia really do have an ejecta-hole geometry, and could constrain the hole opening angle if one exists. While a hole smaller than $\theta < 20^\circ$ has only minor effects on the spectrum, luminosity, and continuum polarization, it will still create

substantial line peaks in the polarization spectrum when seen from some viewing angles. If such signatures of the hole are not seen in future spectropolarimetric observations, this would have interesting consequences for the progenitors of SNe Ia, or the hydrodynamics of the ejecta/companion interaction.

Chapter 6

The Narrow Iron Lines of the Type Ic Supernova SN 1999as

6.1 Introduction

Type Ic supernovae (SNe Ic) are believed to be the core collapse explosions of massive stars that have lost their outer hydrogen (and perhaps helium) envelope (Wheeler & Harkness, 1990; Filippenko, 1997; Matheson et al., 2001). SN 1994I is often considered the prototypical "normal" SN Ic (Filippenko et al., 1995). Its spectrum showed prominent features of singly ionized calcium, iron, and silicon, as well as neutral oxygen and sodium, but no hydrogen. The Doppler shift of the spectral lines show that some material was expanding at $\sim$20000 km s^{-1}, and perhaps as fast as 30000 km s^{-1} (Millard et al., 1999). Models of the light curve and spectra of SN 1994I suggest an ejected mass of $\sim$1-2 $M_{\odot}$, an explosion energy of $\sim$(1-2) $\times 10^{51}$ ergs, and an ejected ^{56}Ni mass of $\sim$0.07 $M_{\odot}$ (Iwamoto et al., 1994; Woosley & Eastman, 1997; Baron et al., 1999).

The Type Ic SN 1998bw, associated with gamma-ray burst GRB 980425, differed from the "normal" case in several ways (Galama et al., 1998; Mazzali et al., 2001). Its optical luminosity was almost ten times that of SN 1994I, and its light curve was signifi-

cantly broader. Its spectrum showed most of the same basic features as SN 1994I, but the lines were extremely broad and blended, indicating that some material was moving faster than 40000 km s^{-1}. The high implied kinetic energy has prompted so-called "hypernova" explosion models, where the explosion energy is $\sim (2-5) \times 10^{52}$ ergs and the ejected ^{56}Ni mass is $\sim 0.5\ M_{\odot}$ (Iwamoto et al., 1998; Woosley et al., 1999).

Several other SNe Ic have been discovered with spectra that closely resemble that of SN 1998bw, and sometimes they are called "hypernovae" as well. While the high blueshifts of their spectral features suggest large kinetic energy, the light curves of these supernovae may or may not be extraordinary. For example, the light curve of SN 2002ap was only marginally brighter and broader than that of SN 1994I (Gal-Yam et al., 2002; Foley et al., 2003; Leonard et al., 2002; Mazzali et al., 2002). And, while the light curve of SN 1997ef was very broad, the supernova peak luminosity was in fact dimmer than SN 1994I (Garnavich et al., 1997; Hu et al., 1997; Iwamoto et al., 2000). In terms of their radio emission, SN 1998bw was extremely bright, while the radio luminosity of SN 2002ap was ordinary (Kulkarni et al., 1998; Berger et al., 2002).

To add to the already confusing diversity of SNe Ic, we turn here to a very unusual supernova that has not been studied much to date. SN 1999as was discovered at redshift $z = 0.127$ in the 1999 search campaign of the Supernova Cosmology Project (Knop et al., 1999). The supernova was remarkable in several respects. First, with an absolute B-band magnitude of $M_B \approx -21$, SN 1999as is the brightest SN Ic ever discovered, and over 6 times brighter than SN 1998bw. Second, the light curve (which was only observed in a declining phase) follows a linear decay of ~ 0.045 mag/day, which is unusually slow for an SN Ic. Finally, in striking contrast to the high expansion velocities observed in SN 1998bw, SN 1999as showed no evidence of *any* material moving faster than 14000 km s^{-1}. The spectrum is rather distinguished by several narrow (~ 3000 km s^{-1}) Fe II absorption lines blueshifted by ~ 11000 km s^{-1}.

Some discussions of the light curve of SN 1999as have already appeared (Deng et al., 2001; Nomoto, 2003). In this chapter, we focus on what can be learned from the spectra, and in particular the narrow Fe II lines. Perhaps surprisingly, we suggest that

strong circumstellar interaction (CSI) may have played an important role in both powering the light curve and in dramatically restructuring the outer layers of supernova ejecta. This is despite the fact that over several epochs of observations, SN 1999as showed no trace of the narrow emission lines which are generally the "smoking-gun" signature of CSI.

6.2 The Peculiar Type Ic supernova SN 1999as

SN 1999as was discovered on Feb. 18, 1999, and follow-up spectroscopic observations were taken on Mar 3, Mar 15, Apr 7, and Apr 23 (Knop et al., 1999; Goobar et al., 1999). Spectra of the anonymous host galaxy give a redshift of 0.127 and suggest that SN 1999as exploded in an active star forming region. Details on the observations and data reduction will be given in Nugent et al. (2004).

6.2.1 The Light Curve of SN 1999as

SN 1999as was discovered on the decline. Unfortunately the most recent reference images are over a year old, so the date of explosion is not well constrained. The discovery point has $m_B = 18$ mag. Using a distance modulus of 39 mag gives $M_B = -21$ mag, suggesting an intrinsic luminosity, uncorrected for extinction, of order 8×10^{43} ergs s^{-1}.

In Figure 6.1a, we show the B-band light curve of SN 1999as, along with a few other supernovae. When compared to SN 1998bw, the decay of the light curve of SN 1999as is very slow (about 0.045 mag/day in the B light curve, and even slower in V and R). Moreover, out to the last observation point (90 days after discovery) the luminosity is still steadily declining, apparently never having turned over to a shallow ^{56}Co tail. In these respects, the light curve of SN 1999as actually closely resembles the Type II linear supernovae (SNe IIL, e.g., Young & Branch, 1989).

A linearly declining light curve is also typically of Type IIn supernovae (SNe IIn), believed to be supernovae interacting strongly with a dense circumstellar medium. Among the SNe IIn, the rate of decline varies significantly: SN 1984E (Henry & Branch, 1987) and SN 1998S (Li et al., 1998; Liu et al., 2000; Fassia et al., 2000) followed a decline rate very

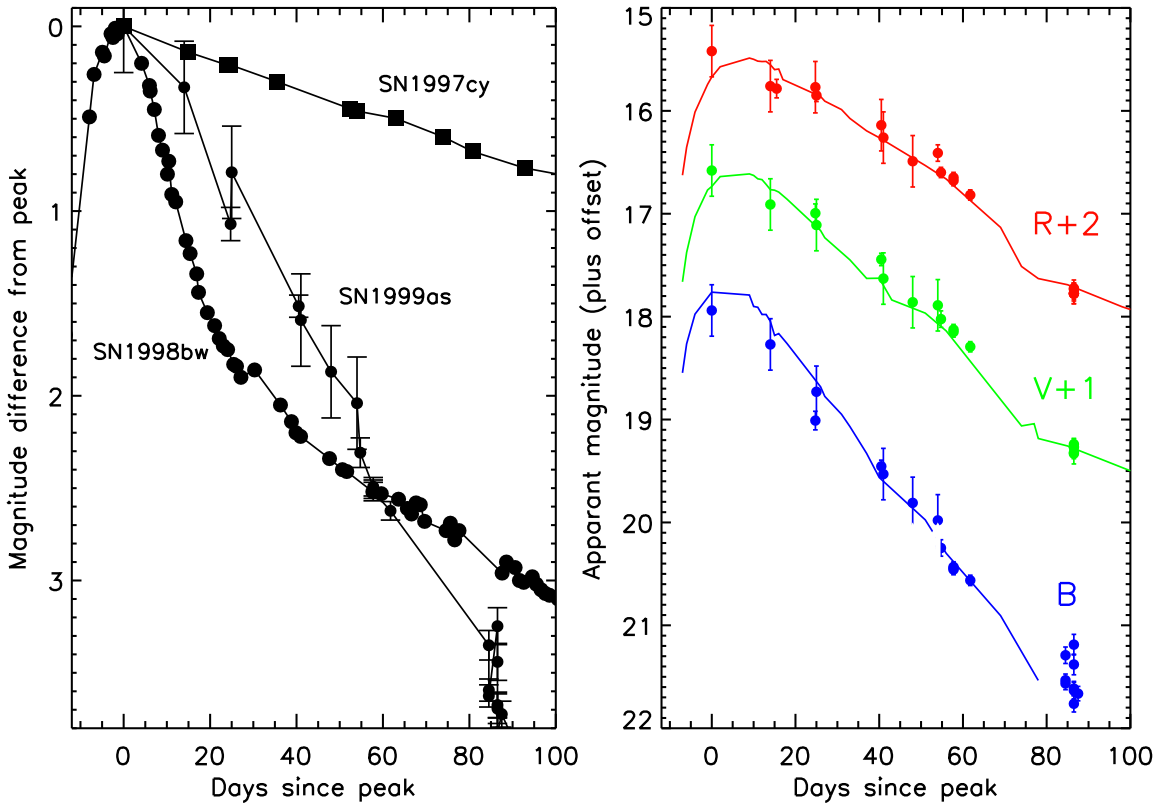

Figure 6.1 The light curve of SN 1999as. (a): B-band light curve of SN 1999as compared to SN 1998bw (Galama et al., 1998; McKenzie & Schaefer, 1999) and the Type IIn SN 1997cy (Germany et al., 2000). All light curves have been normalized at peak. (b): The B, V, and R light curve of SN 1999as (circles with error bars) compared to the light curve of SN 1998S (solid lines, from Liu et al., 2000). The same offset of 5.3 mag has been added to all of the SN 1998S light curves.

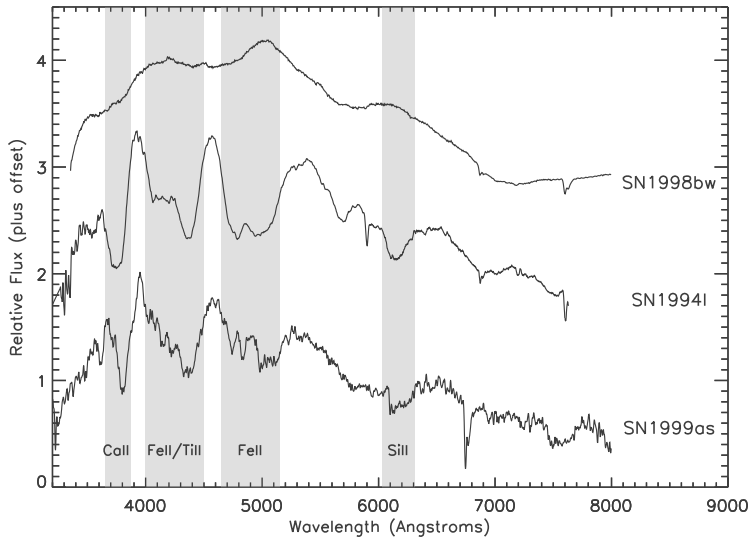

Figure 6.2 The spectrum of SN 1999as 25 days after discovery compared to SN 1998bw and SN 1994I (Filippenko et al., 1995).

similar to a typical SNe IIL, while the decline rates of SN 1997cy (Germany et al., 2000) and SN 1999E (Rigon et al., 2003) were much slower. In Figure 6.1b we show that the light curve shape and color evolution of SN 1998S and SN 1999as were remarkably similar. With an intrinsic luminosity of $M_B \approx -18.8$ mag (uncorrected for extinction, Leonard et al., 2000a), SN 1998S was also an exceptionally bright core collapse supernova, although still roughly two mag fainter than SN 1999as.

6.2.2 The Spectrum of SN 1999as

Figure 6.2 shows the SN 1999as spectrum on March 15 (25 days after discovery) compared to SN 1994I and SN 1998bw. No obvious hydrogen or helium features are visible in SN 1999as, and in general the spectrum resembles that of SN 1994I, securing a SN Ic classification. Particular to SN 1999as, however, are the numerous narrow Fe II absorption features in the region 4000-5500 Å. The most prominent of these are the three minima

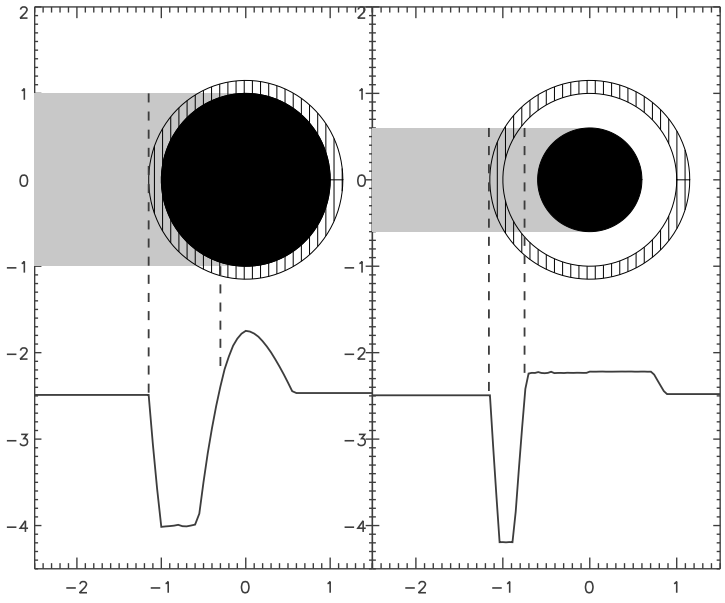

Figure 6.3 Schematic diagram showing the formation of narrow absorption lines. The width of the absorption line measures the *observer line of sight* velocities over which the photosphere is obscured. Thus, even if the line opacity is confined to a thin shell, the absorption feature will still be broad (left) unless the shell is significantly detached from the photosphere (right).

at 4745 Å, 4830 Å, and 4983 Å, due to a blueshifted Fe II triplet ($\lambda\lambda\lambda 4923, 5018, 5169$). Several additional narrow Fe II lines can be identified, and there also appear to be a few narrow Ti II absorptions.

The relatively high blueshift of the narrow Fe II lines ($v_{nl} \approx 11000$ km s^{-1}) indicates that they are formed in the supernova ejecta, and not in interstellar material or a circumstellar wind. The narrow line width ($\Delta v \approx 3000$ km s^{-1}) further suggests that these ejecta have a shell-like structure, with well-defined inner and outer boundaries. However, as Figure 6.3 shows, such a shell does not lead to narrow absorption features *unless* the shell

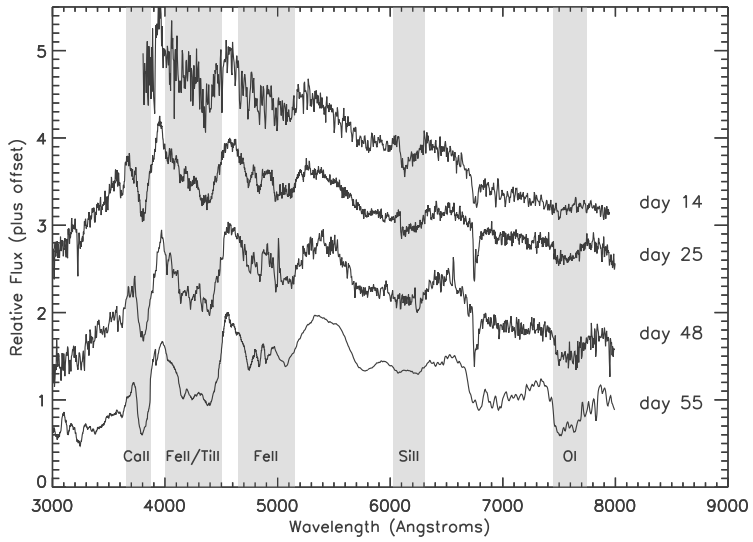

Figure 6.4 Time series of spectra of SN 1999as.

is significantly detached from the supernova photosphere. From the geometry of the figure (and assuming homologous expansion) it is clear that a thin shell of velocity thickness δv and velocity radius v_{nl} obscures the photosphere for an observer line of sight velocity range given by

$$\Delta v_{\rm obs} = \delta v + v_{nl}\left[1 - \sqrt{1 - \frac{v_{nl}^2}{v_{\rm ph}^2}}\right], \tag{6.1}$$

where $v_{\rm ph}$ is the velocity of the photosphere. To reproduce the width of the narrow Fe II triplet lines in SN 1999as, one needs a detached shell with $v_{nl} \gtrsim 1.4 v_{\rm ph}$. Because line blending will affect this simple conclusion, we explore the narrow line formation with radiative transfer calculations in §6.5.

Other features in the SN 1999as spectrum are of normal width, and can be identified as the usual features due to Ca II, Si II, and O I. In no feature, however, does the blue edge of the absorption exceed $v_{\rm max}$=14000 km s^{-1}. This property is especially striking in the Ca II H&K absorption near 3800 Å, which in SN 1994I, SN 1987M, and most other Type Ic supernovae exceeds 20,000 km s^{-1} (Filippenko, 1992; Filippenko et al., 1995;

Matheson et al., 2001). The utter lack of line absorption above $v_{\rm max}$ holds for all epochs of observation of SN 1999as. As Figure 6.4 shows, the spectral evolution is remarkably slow, such that over a period of 40 days there is hardly any change in the depth or Doppler shifts of any of the features. In addition, the Si II and O I features show rather sharp blue edges; one therefore suspects that the density structure of SN 1999as cuts off suddenly for $v > v_{\rm max}$,

In terms of the implied kinetic energy of its ejecta, SN 1999as ranks below SN 1994I and is on the opposite end of the gamut from SN 1998bw. One might therefore conclude that this was a relatively weak SN Ic explosion that failed to ejecta any material above $v_{\rm max}$. The fact that SN 1999as was also the *brightest* and broadest SN Ic, requires us to reconsider this supernova in a very different context.

6.3 Hypernova Explosion Models

One can attempt to explain the light curve SN 1999as in the usual way for Type I supernovae, as powered by ^{56}Ni synthesized in the explosion. Following Arnett (1982), the luminosity at the light curve peak L_p is roughly equal to the instantaneous rate of energy deposition from ^{56}Ni, giving the approximate expression

$$M_{Ni} = 0.38 M_\odot \left(\frac{L_p}{10^{43}\ \mathrm{ergs\ s^{-1}}}. \right) \tag{6.2}$$

Under the minimal assumption that the discovery of SN 1999as coincided with the light curve peak, the observed luminosity $L_p \gtrsim 8 \times 10^{43}$ ergs s^{-1} implies a ^{56}Ni mass greater than 3 $M_\odot$. This is over six times that of SN 1998bw, and thirty times the normal core collapse amount.

The slow, steady decline of the SN 1999as light curve also implies a large total ejected mass. In a diffusion scenario, the time of the peak should scale as

$$t_p \approx \sqrt{\frac{\kappa}{c}} M_{\rm sn}^{3/4} E_{\rm sn}^{-1/4}. \tag{6.3}$$

With a "peak" extending to at least day 90, the implied ejected mass for SN 1999as is of order 10-20 $M_\odot$.

It is clear that in a ^{56}Ni-powered scenario, SN 1999as represents a hypernova explosion of unprecedented power. Deng et al. (2001) were able to fit the light curve using a model with $M_{\rm Ni}$= 4 $M_\odot$, $M_{\rm sn}$= 10-20 $M_\odot$, and $E_{\rm sn}$= (30-100) $\times 10^{51}$ ergs. The progenitor of this explosion was presumably the carbon-oxygen core of a very massive (> 60 $M_\odot$) star, and the collapse almost certainly resulted in black-hole formation.

It is hard to reconcile these enormous energy estimates with the unusually low velocities observed in the SN 1999as spectra. In general, the density structure of core-collapse supernovae is flat in the inner layers, and follows a power law in the outer layers (Chevalier & Fransson, 1994):

$$\rho_{\rm sn}(v,t) = \frac{3(n-3)}{4\pi n}\left[\frac{3(n-3)}{5(n-5)}\right]^{\frac{1}{2}(n-3)} M_{\rm sn}^{-\frac{1}{2}(n-5)} E_{\rm sn}^{\frac{1}{2}(n-3)} t^{-3} v^{-n}. \qquad (6.4)$$

For a typical value $n = 7$, the density at a velocity v scales like $\rho \propto M_{\rm sn}^{-1} E_{\rm sn}^2$. Thus, in the hypernova models of Deng et al. (2001), the line blueshifts are expected to be much higher than normal. Figure 6.5 shows the calculated spectra of such a hypernova model 50 days after explosion. The photosphere of this model occurs at 20000 km s^{-1}, and all the line features are too broad. The narrow Fe II lines of SN 1999as are also not reproduced by the model, and in general the synthetic spectrum, not surprisingly, more closely resembles the spectrum of SN 1998bw.

Given the scaling $\rho \propto M_{\rm sn}^{-1} E_{\rm sn}^2$, it may be possible to get a better fit to SN 1999as using a hypernova model with much higher $M_{\rm sn}$ but lower $E_{\rm sn}$. It is not clear, however, how this situation might come about – if the explosion is powered by accretion onto a black hole, a more massive progenitor is expected to give higher explosion energies (Nomoto, 2003). Moreover, if we increase $M_{\rm sn}$ while keeping $E_{\rm sn}$ fixed, the light curve rise-time lengthens, so that the already improbably high ^{56}Ni mass would have to be increased even further.

We should also mention that normal energy explosion models like those used for SN 1994I will not work for SN 1999as. Besides obviously failing to reproduce the luminosity of SN 1999as, these models cannot explain the slow spectral evolution. By the time the later spectra were taken (day 55 after explosion, presumably $\sim$65 days after explosion in a low-mass model) the photosphere should have completely receded, and the spectra would

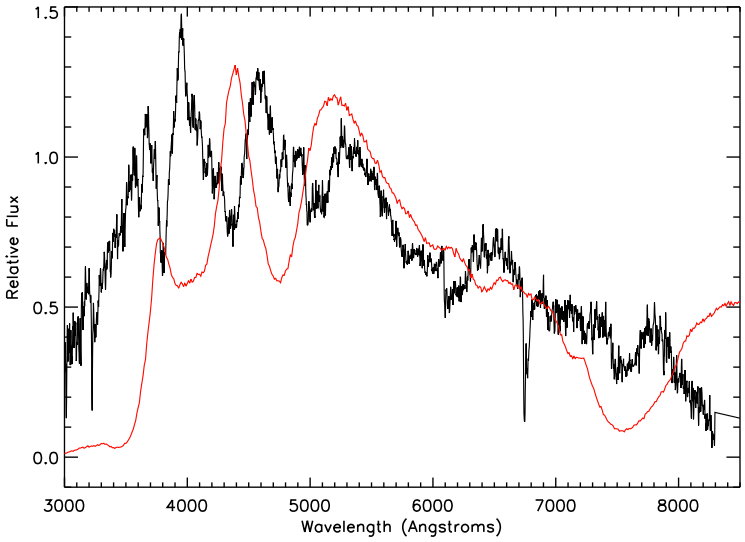

Figure 6.5 Synthetic spectrum of a "hypernova" model (thin line) compared to the March 15 SN 1999as spectrum. The model consists of carbon-oxygen rich material with a density structure given by Equation 6.4 with $n = 7$. The time since explosion is 50 days and the luminosity 4×10^{43} ergs s^{-1}. The fit is very poor.

have transitioned into the nebular phase. Another problem is that these models predict a Ca II H&K blueshift that well exceeds 14000 km s^{-1} (Baron et al., 1999).

6.4 Circumstellar Interaction Effects

Given the difficulty hypernova models have explaining the spectra of SN 1999as, we turn now to the possible effects of circumstellar interaction (CSI). The progenitors of core collapse supernovae experience heavy mass loss in their late stages of evolution, such that the vicinity around a supernova may consist of high density circumstellar material (CSM). The result of the supernova ejecta interacting with the CSM is a double-shock structure, with a forward shock propagating into the circumstellar material, and a second

reverse shock propagating back into the supernova ejecta (Chevalier, 1982). Two relatively thin shells are formed: an inner shell of decelerated supernova ejecta, and an outer shell of swept-up CSM. If the shells are adiabatic, they will be hot ($T \approx 10^7$ K for the inner shell and $\sim 10^9$ K in the outer) but they may cool radiatively or by expansion. When bremsstrahlung emission dominates, the radiation will be mostly in X-rays, which may be absorbed in the ejecta/CSM, thermalized and reprocessed into optical radiation.

There are several reasons to consider the possibility that SN 1999as experienced strong circumstellar interaction. First, because CSI converts the kinetic energy of the ejecta into radiation, extreme optical luminosities may result – the Type IIn supernovae SN 1997cy, SN 1999E, and SN 1998S were all more than 10 times brighter than average core collapse supernovae (Germany et al., 2000; Rigon et al., 2003; Fassia et al., 2001). Second, as we have already mentioned, the linear light curve and colors of SN 1999as closely resemble the Type IIn SN 1998S (Figure 6.1). Third, the swept-up CSM should decelerate the highest velocity ejecta, which provides a natural means of cutting off the expansion at $v_{\rm max}$= 14000 km s^{-1}. Finally, the interaction can lead to the formation of a thin, detached shell, which as we discussed in §6.2.2, may explain the narrow Fe II features in SN 1999as.

While the above reasons are very suggestive, the spectrum of SN 1999as lacks the "smoking-gun" signature of strong CSI. Usually, the interaction is evidenced by narrow emission lines from the hydrogen Balmer series (e.g., Filippenko, 1997), hence the spectral classification of Type IIn ("n" for narrow, Schlegel, 1990). These emission lines are centered on the line rest wavelength, and typically had both a narrow (width ∼100-200 km s^{-1}) and an intermediate (∼1000-2000 km s^{-1}) component. The lines are believed to come from the recombination of the photo-ionized and shocked hydrogen-rich CSM. Sometimes narrow emission lines from helium, carbon, nitrogen and other elements are also observed. In most cases, the ordinary supernova P-Cygni features are not seen, or at least are very weak.

No strong narrow emission lines were observed in SN 1999as, but this does not necessarily close the door on a CSI interpretation. Once again, SN 1998S provides the point of reference. The early spectra of SN 1998S showed strong hydrogen emission lines on a nearly featureless, blackbody continuum (Leonard et al., 2000a; Fassia et al., 2001). After

about two weeks, however, the narrow emission almost completely disappeared, and broad (but weak) supernova P-Cygni profiles began to be visible. In fact, Leonard et al. (2000a) remark on the similarity of the spectrum at this time to that of a SN Ic. A similar vanishing act occurred in the Type IIn SN 1984E (Henry & Branch, 1987).

In the consensus interpretation of Henry & Branch (1987), Fassia et al. (2001), Leonard et al. (2000a), and Chugai (2001), both SN 1984E and SN 1998S emitted a strong "super-wind" just 10-100 years before the explosion, creating a very dense CSM within $\sim$100 AU of the progenitor. Strong CSI occurred during the first few weeks of expansion, but after a few weeks the supernova ejecta had completely overrun the densest CSM. We might suspect that a similar thing happened in SN 1999as, and that no emission lines were seen because the dense CSM had been overrun before our earliest spectroscopic observation, 15 days after discovery.

One additional factor to consider in the case of SN 1999as is that the CSM may have been composed of helium rich material. The progenitors of SNe Ic are believed to expel their helium envelopes subsequent to expelling their hydrogen envelopes – thus the dense material immediately surrounding SN 1999as may have been composed primarily of helium, with little or no hydrogen. Interaction with a pure helium CSM was apparently observed in the Type Ic SN 1999cq, which showed narrow He I emission without any hydrogen line emission (Matheson et al., 2000). This supernova, incidentally, was also rather luminous, having an unfiltered magnitude of roughly -19.6 (with, however, a large uncertainty). No narrow helium emission was observed in SN 1999as, which may suggest again that the densest CSM had already been overrun by the time of the observations. In addition, because of the high ionization/excitation energies of helium compared to hydrogen, one expects the helium line emissivity to be much more sensitive to the density and excitation conditions. The absence of helium line emission is therefore not as robust an indication that no CSI has taken place.

6.5 Shell Models of the Spectrum of SN 1999as

To explore the CSI hypothesis for SN 1999as, we have calculated synthetic spectra using the Monte Carlo code described in Chapter 3. Assuming the phase of strong CSI occurred prior to the first spectroscopic observations, the only direct spectral evidence of the interaction we have is in the restructuring of the supernova ejecta. We use the density law of Equation 6.4, but with all material above $v_{\rm max}$ decelerated into a shell. For $n = 7$, the mass of supernova ejecta above $v_{\rm max}$ is

$$M_{\rm sn,sh} = 0.04 M_{\odot} \left(\frac{M_{\rm sn}}{M_{\odot}}\right)^{-1} \left(\frac{E_{\rm sn}}{10^{51}\ {\rm ergs}}\right)^{2} \left(\frac{v_{\rm max}}{14000\ {\rm km\ s^{-1}}}\right)^{-4}. \tag{6.5}$$

The initial momentum P_I of the ejecta above $v_{\rm max}$ can also be determined by integrating Equation 6.4. From conservation of momentum we then find the mass of the swept-up circumstellar material,

$$M_{\rm cs,sh} \approx P_I / v_{\rm max} - M_{\rm sn,sh} = \frac{1}{3} M_{\rm sn,sh}. \tag{6.6}$$

Because the interaction is Rayleigh-Taylor unstable, the material in the inner and outer shells may be mixed (Chevalier & Klein, 1978).

To give an illustrative example, we use an energetic model with $M_{\rm sn}$=5 $M_{\odot}$ and $E_{\rm sn}$=10$\times$10^{51} ergs. This leads to an outer shell mass of $\sim$0.2 $M_{\odot}$, which we assume is located between velocities 12500-14000 km s^{-1}. In addition, we assume homologous expansion, although it is not clear that this condition will be met. To compare to the March 15 SN 1999as spectrum we use a luminosity $L_0 = 4 \times 10^{43}$ ergs s^{-1} and a time since explosion $t_{\rm exp} = 40$ days. Figure 6.6 shows the model spectrum compared to the observations. The fit is very good, with many narrow Fe II and Ti II lines reproduced, including the prominent Fe II triplet. In addition, the Ca II H&K blueshifts are correct and the O I and Si II absorptions have a sharp blue edge.

Given our framing of the problem, the spectrum of SN 1999as requires a rather massive, energetic explosion like the one used in Figure 6.6. If the parameters appropriate for SN 1994I are used ($M_{\rm sn}$= 1 $M_{\odot}$, $E_{\rm sn}$=1$\times$10^{51} ergs), the resulting densities and shell

mass ($\sim 0.05 M_\odot$) are too small to reproduce the spectral features. On the other hand, an extremely energetic hypernova model doesn't seem realistic either. For parameters $M_{\rm sn}$= 20 and $E_{\rm sn}$= 50×10^{51} ergs, the shell mass exceeds 2 $M_\odot$, and is optically thick to electron scattering up to 100 days after the explosion. In this case, a pseudo-photosphere forms in the shell, and all narrow line formation is washed out.

Obviously the explosion and subsequent interaction need to be modeled self-consistently, but the relatively large shell mass and the extreme luminosity of SN 1999as suggest that the supernova explosion may have been more energetic than normal. The realization that $M_{\rm cs,sh} \approx 0.03\ M_\odot$ also constrains the mass-loss rate in the super-wind. Assuming the densest CSI was overrun by day $\sim$20, the mass-loss rate is

$$\dot{M} \approx 4 \times 10^{-3} M_\odot\ {\rm yr}^{-1} \left(\frac{M_{\rm cs,sh}}{0.03\ M_\odot} \right) \left(\frac{v_w}{100\ {\rm km\ s}^{-1}} \right) \left(\frac{v_{\rm max}}{14000\ {\rm km\ s}^{-1}} \right)^{-1} \left(\frac{t_{\rm exp}}{20\ {\rm days}} \right)^{-1}, \tag{6.7}$$

where v_w is the wind velocity. Red giant stars have wind velocities of order 10 km s^{-1}, whereas a Wolf-Rayet progenitor could have $v_w \approx 2000$ km s^{-1}. In either case, the mass loss was extreme, and occurred within 10-100 years of the supernova explosion.

Our empirical conclusion is that to fit the spectrum of SN 1999as, all material above $v_{\rm max}$=14000 km s^{-1} must be removed into a shell of mass $\sim 0.1\ M_\odot$ and thickness roughly $\Delta R/R_s \approx 0.15$. However, our model in Figure 6.6 has glossed over the details of shell formation. The shell thickness we have used ($\Delta R/R_s \approx 0.15$) is consistent with the adiabatic self-similar solutions of Chevalier (1982). However, in the adiabatic case these shells will be hot, and they probably will not have had time to cool sufficiently by expansion. If the shells cool radiatively during the interaction phase, the pressure imbalance will compress them into an even thinner layer, in which case they may become too thin to create narrow absorption lines (note, the depth of the line at a certain wavelength depends on the percent of the photosphere covered on the corresponding CV plane, and so is proportional to $\Delta R/R_s$). In the future, we need realistic hydrodynamical/interaction calculations to determine the resulting shell thickness. In general, however, the picture presented here seems very appealing.

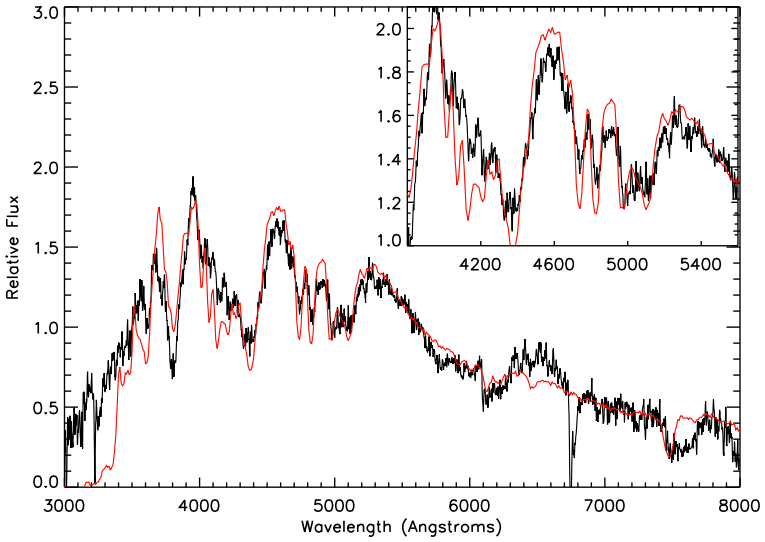

Figure 6.6 Synthetic spectrum of a shell model (thin line) compared to the March 15 spectrum of SN 1999as. The inset shows a zoom-in on the region of narrow line formation.

6.6 Conclusions

The basic puzzle of SN 1999as is that its spectrum indicates normal or low kinetic energy, whereas its luminosity was extraordinary. It is difficult for any existing model of SN Ic explosions to explain this unlikely combination of properties. Spherical hypernova models are unable to reproduce the low absorption blueshifts and narrow Fe II lines, while normal SN Ic explosions cannot power the luminosity. We have argued here that SN 1999as may indeed have been an energetic SN Ic, but that both its light curve and its ejecta structure were profoundly affected by circumstellar interaction.

Our analysis has focused on the spectra of SN 1999as, and we leave detailed modeling of the light curve to future work. Presumably strong CSI can explain the early, very bright observations of SN 1999as in a way similar to that already discussed for SN 1997cy and SN 1998S (Turatto et al., 2000; Chugai, 2001) (note that Turatto et al. (2000) claim

that even when strong CSI is taken into account, a hypernova-like kinetic energy is needed to tap enough kinetic energy to reproduce the high luminosity of SN 1997cy). In SN 1999as, the strongest CSI has apparently ceased by around day ∼25, but contributions to the luminosity may still come from the continued deceleration of the supernova ejecta by a reverse shock, or from diffusion of the thermal energy released in the earlier epoch of interaction. In any case, it is likely that at these later times, the ^{56}Ni produced in the initial explosion makes an increasingly dominant contribution to the total luminosity. In fact, to achieve the narrow line formation, it is essential that the primary energy source be situated within the shell – any radiation generated at or exterior to the shell will dilute the line strengths (Branch et al., 2000). However, assuming we attribute the earliest, extremely bright observations of SN 1999as to CSI, the required ^{56}Ni mass needed to explain the later-time light curve (∼0.5-1.0 $M_{\odot}$) may not be totally unusual for energetic SNe Ic.

If the CSI interpretation is correct, the observations of SN 1999as strengthen the connection between SNe Ic and SNe IIn in an unexpected way. Such a connection had already been guessed at from the SN Ic-like spectrum of SN 1998S (Leonard et al., 2000a), and the broad, SN 1998bw-like absorption features of SN 1999E and SN 1997cy (Filippenko et al., 1999; Turatto et al., 2000). A interesting link is also suggested by the tentative association of both SN 1997cy and SN 1999E with GRBs (Germany et al., 2000; Rigon et al., 2003). If in addition one recalls that Hamuy et al. (2003) found a *Type-Ia supernova* with strong narrow hydrogen emission lines, it starts becoming clear that the SNe IIn are probably not a distinct sub-class of supernovae, but encompass the entire range of known supernova types that, for whatever reason, happened to occur in a dense CSM. The fact that the SN 1999as spectra were so typical of a SN Ic, and that no narrow emission lines were seen, raises an interesting question: Might circumstellar interaction be significantly affecting the luminosity, light curves, and ejecta structure of many other supernovae, without leaving any of the obvious traces?

Chapter 7

Conclusion

7.1 Summary

The goal of this thesis has been to apply 3-D radiative transfer techniques to study asymmetry in supernovae. In Chapter 2 we laid out the basic concepts and in Chapter 3 the mathematical/computational methods needed to approach the transfer problem. The following three chapters consisted of applications. In Chapter 4 we took a "top-down" approach, empirically fitting the polarization data of SN 2001el, and speculating about the implications of its geometry for theoretical models of SNe Ia. In Chapter 5, we took a "bottom-up" approach, calculating the optical properties of a supernova with an ejecta hole, and speculating about the relevance of the asymmetry to observations of SNe Ia. A little bit of both approaches went into the analysis of the unusual Type Ic SN 1999as in Chapter 6.

In this Conclusion, we first look ahead to planned advances in the 3-D radiative transfer methods. We then discuss how the results of this thesis relate to the larger scientific questions raised in the Introduction. We end with some general reflections on the challenge of studying supernovae in 3-D.

7.2 Improvements to the Radiative Transfer Calculations

The Monte Carlo methods pursued in this thesis proved highly applicable to the problem of 3-D radiative transfer in supernovae. The only major drawback of the approach is the computational inefficiency, and this becomes increasingly irrelevant as the speed of computers advances. In the future, we hope to improve both the applicability and the physical accuracy of the calculations within the basic MC framework. Two of the most significant planned developments are discussed below.

Time Dependence: Relaxing the quasi-static assumption made in the current calculations would allow for computations of 3-D supernova light curves, polarization curves, and a self-consistent time series of spectra. Time-dependence can be incorporated into the MC procedure in a symmetric way. To our 3-D atmospheric grid we add a fourth time dimension, and photon packets now propagate not only through the spatial grid, but also the temporal one. In taking a spatial step of length Δv, the packet also moves forward in time a duration $\Delta v t_{\rm exp}/c$. All packets that escape the atmosphere are binned in both viewing angle and time observed.

Chugai (2000) has implemented these ideas in a relatively simple MC light curve code, which assumes spherical symmetry and a constant opacity. The goal of future work is to generalize time-dependent methods to include 3-D models with realistic opacities, gamma-ray deposition, polarization, and an iterative solution of the evolving temperature structure. Such calculations are essential for testing the validity of 3-D explosion models, and for investigating, for example, how asymmetries might affect the width-luminosity relationship so essential to SN Ia cosmology.

Non-Local Thermodynamic Equilibrium: Perhaps the most significant physical approximation made in the present code is that ionization and excitation are computed in local thermodynamic equilibrium. Although this is likely a reasonable approximation for SNe Ia near maximum light, inclusion of NLTE is necessary for calculating SN II atmospheres and for quantitative accuracy in the SNe Ia. The assumption of LTE completely breaks down at very late times (the nebular phase); here the ejecta are optically thin in the continuum,

and the emission is through low-level forbidden lines (Ruiz-Lapuente et al., 1995). 3-D nebular spectra provide a powerful diagnostic of supernova models, as late-time observations probe the innermost layers of supernova ejecta. For example, the 3-D SN Ia deflagration models (see Figure 2.3) have unburned carbon and oxygen at their center, whereas in a deflagration-to-detonation explosion this would be burned to ^{56}Ni by the detonation wave.

Solving for departures from equilibrium can, in fact, be naturally incorporated into the MC scheme through a solution of the rate equations and a procedure of branching (Li & McCray, 1993; Zhang & Wang, 1996; Lucy, 2001, 2002, 2003). These techniques make it feasible for MC codes to eventually match the physical accuracy of formal solutions of the radiative transfer equation.

7.3 Scientific Retrospective

In the Introduction to this thesis, we mentioned how studies of the spectra and polarization of supernovae related to three larger scientific questions. Now we reflect on the small ways in which we have touched upon these areas, and discuss how future studies may contribute further to our understanding.

7.3.1 Type Ic Supernovae and GRBs

Our study of the peculiar Type Ic supernova SN 1999as (Chapter 6) emphasized the spectroscopic and photometric diversity of SNe Ic. SN 1999as was further evidence that the kinetic energy as measured from the spectral lines is not always a good indicator of the luminosity. One of the main challenges of future theoretical modeling will be to understand the wide range of SN Ic properties, and explain why some create GRBs, while others, like SN 2002ap and SN 1999as, apparently do not.

The "collapsar"/jet scenario is perhaps the most popular model for SNe Ic/GRBs, but as yet no multi-dimensional explosion calculation has been directly compared to supernova observations. Among the questions that might be addressed by future 3-D radiative transfer calculations are the followingq: Is enough high-velocity material ejected along the

(largely evacuated) polar regions to explain the broad spectral features of SN 1998bw? Are the shape and compositional asymmetries consistent with the polarization levels and polarized line features? Is the amount of ^{56}Ni produced and the trapping of gamma-rays in the aspherical ejecta sufficient to explain the light curve? What are the consequences of jets of different energy or collimation angle? What do the models look like when viewed away from the jet axis, and what connection is there, if any, to the normal SNe Ic?

7.3.2 The Progenitors and Explosion Mechanism of SNe Ia

Most people believe that the progenitors of SNe Ia are white dwarfs accreting material from a non-degenerate companion star. Direct verification of this, however, has been slow to come. The recent discovery by Hamuy et al. (2003) of SN 2002ic, a SN Ia with overwhelming strong hydrogen emission, does not necessarily clear up the issue (Livio & Riess, 2003; Baron, 2003). If SNe Ia in general arise in the vicinity of a hydrogen-rich companion, why have we not see any signs of the hydrogen until now?

In this thesis we have noted several more subtle ways in which we may detect traces of a companion star. The high velocity material seen in SN 2001el could be explained as the result of swept-up circumstellar material (Gerardy et al., 2003), or material stripped directly from the companion star upon impact (Marietta et al., 2000). In fact, both Branch et al. (2004) and Thomas et al. (2004) have suggested an identification of high-velocity Hβ in the Type Ia SN 2000cx, which if correct would strongly suggest that the material was associated with the companion in some way. In SN 2001el, the polarization data allowed us to infer a unique geometry for the high velocity material, which suggests that this material did indeed have a different origin than the bulk of the ejecta.

Our calculations of a SN Ia with an ejecta hole (Chapter 5) have provided some completely new tests of the single-degenerate progenitor scenario. Assuming the simulations of Marietta et al. (2000) are reliable in the sense that a substantial hole is indeed formed and does not quickly close with time, our studies suggest that signs of a companion may have already been seen in the polarization and SN 1991T-like spectral peculiarities of some

SNe Ia. Moreover, we have described some observational signatures that will allow us to rigorously test for the ejecta-hole in the future.

The most important new issues to address in SN Ia studies are those related to the supernova explosion physics. As discussed earlier, 3-D deflagration models predict a very clumpy ejecta composition structure. Whether this highly irregular structure is consistent with observations is not yet clear (Thomas et al., 2002). If the deflagration transitions into a detonation, however, most of the inhomogeneities will be burned away (Höflich et al., 2002). In the next year or so, full explosion models will be run to completion, and made available for 3-D radiative transfer calculations.

7.3.3 Type Ia Supernovae and Cosmology

Although the number of published SNe Ia with clear polarization detections is still relatively small, many more (so far unpublished) have been observed. Asphericity is therefore not the exception, but the rule for SNe Ia. This may have a number of subtle consequence on the use of supernovae as calibrated candles for cosmology.

Given the observed polarization levels, asymmetry is expected to cause a $\sim 20\%$ dispersion in SN Ia peak magnitude (Howell et al., 2001; Kasen et al., 2003a). If the asymmetry is identical in all supernovae, this dispersion behaves like a statistical error (although a non-Gaussian one) and can be averaged out by observing enough objects. The averaging out is not achieved, however, if one does not sufficiently sample *every* possible viewing angle. For example, in the ejecta hole model, the luminosity peaks sharply for views down the hole, and so the reduction of errors will hinge upon how often we sample this infrequent view. Trouble may also arise if some viewing angles are withheld from the sample due to concern over their spectral peculiarities, or because of an ill-advised data cut (e.g., on color). In addition, if the nature, degree, or frequency of the asymmetry evolves with redshift (say, because of evolving progenitor populations), the peak magnitudes of SNe Ia become a function of redshift.

These potential effects on cosmology should be relatively small, but may need to

be considered in the next generation of precision supernova cosmology experiments. For example, the proposed SNAP satellite experiment would like to control systematic errors to the $\lesssim 2\%$ level (Aldering et al., 2002) – if the uncertainties are increased to just 4%, the determination of the cosmic equation of state parameter w and its time derivative are significantly degraded (Kim et al., 2004). In general, one should try to accomplish this level of precision empirically, without having to rely on the still uncertain theoretical models. However, 3-D radiative transfer calculations may be helpful in identifying the potential sources of luminosity variations, and how they may be correlated with observables. One might hope to identify key spectral and photometric features that reduce the intrinsic dispersion of SNe Ia, and provide a handle on any potential evolution of the asymmetry with redshift.

7.4 Some Final Reflections

Looking ahead to future studies of asymmetry in supernovae, what are the challenges facing us? The first thing to admit is that the fundamental problem ahead is *not* the difficulty of solving the 3-D radiative transfer problem. This is despite the substantial suffering endured already in beginning to develop such transfer codes – in the end, although 3-D radiative transfer problems pose a very significant technical challenge, the physics is for the most part well understood, and it is fairly straightforward how to proceed; all that is needed is powerful enough computers and a good deal of dedication, and the first of these, at least, is certainly not long to come.

The more fundamental difficulty in 3-D studies, then, is the opening up of an enormous parameter space. We confronted the problem head-on in our fitting of the polarization spectra of SN 2001el in Chapter 4. In that case, even though we constrained our models to idealized "two-axis" systems, the number of available configurations was still overwhelming, and fitting the data through trial and error was at the limit of what is humanly possible. Moreover, as the number of free parameters is increased further, the meaning behind the fitted values probably diminishes. Eventually, we had to admit that this inverse problem

was ill-posed, and that more than one configuration could provide a good fit to the data. This fundamental limitation would not have been helped by taking more observations at more epochs, or with higher signal-to-noise ratio – there simply is not enough information in the observations of an individual supernova to completely constrain the geometry of its ejecta.

Thus, the fitting of data in an empirical spirit – an approach which has been so crucial to our understanding of supernovae to date – may become an increasingly useless exercise when we move to 3-D. One might therefore abandon the "top-down" approach in favor of first-principle, "bottom-up" calculations. The role of the radiative transfer specialist is then to churn out the optical properties of hydrodynamical explosion models, and compare them against observations. Unfortunately, a different set of difficulties emerge. First, even our most fundamental explosion calculations will still have to include a very large number of free parameters, as we will never fully know the initial conditions describing the structure and geometry of the supernova progenitor or its environment. Second, each 3-D supernova model actually makes not one, but multiple predictions depending upon which of the many different lines of sight from which it is viewed. Third, if we believe, as we do, that much of the geometrical structure in supernovae is the result of random processes, then both the object and our simulation of it are singular events – even if our treatment of the physics and knowledge of the initial conditions are completely correct, the predicted theoretical ejecta structure may not match up to any actual observed event. Finally, because the spectropolarimetric signatures can be rather sensitive to the detailed ejecta structure, a model that does indeed capture the salient features of the explosion scenario may still fail to "fit" the data of any supernova very well. In fact, by pure coincidence the data may be fit as well by an irrelevant model. Thus, the process of comparing theory to observations is no longer completely trivial.

The final solution may require a synthesis of both the "top-down" and "bottom-up" approaches. While it may not be possible to empirically reconstruct the 3-D structure of any given supernova, using the "top-down" approach in Chapter 4 we were able to constrain the allowed regions of parameter space, and this narrowing of the possibilities is certainly of

some use in guiding detailed explosion models. On the other hand, while our "bottom-up" calculation of the ejecta-hole model may not have been able to perfectly fit the polarization data of any particular supernova, we could understand the qualitative trends arising from the explosion/progenitor scenario, and hence assess its general relevance to observations.

Our theoretical insights into supernova asymmetry thus involve clarifying the relevant polarization signatures and line-of-sight variations specific to different geometries. For this reason, future studies of 3-D supernovae may focus less on "fitting" individual objects, and more on identifying the statistical properties inherent to a specific subset of models. The "predictions" of these theoretical models will be the statistical distribution of certain observable quantities, such as light curve rise times, absorption blueshifts, continuum polarization levels, etc. Different regions in the theoretical parameter space can be ruled out by comparing calculated distributions to those of a large sample of well-observed supernovae. We can only hope that supernovae are not so diverse a phenomenon that the geometrical effects are lost in a confusion of other sources of individual variety.

While this thesis has focused on theoretical studies of supernovae, for the foreseeable future our understanding will be driven by the observations. Given the number of peculiar objects turned up in the last few years alone, it is clear that we haven't yet come close to completely sampling the full variety of supernovae; in any program that discovers many supernovae – or looks very closely at one – you are almost assured of finding something unexpected. In the next decade the quantity and quality of the observations should both greatly increase; before long, thousands of well-observed supernovae may be available. It is hoped that once the rich data set is laid out before us, most of the mysteries surrounding supernovae will be dissolved. Actually, the opposite may be the case – with the ceaseless variety of these objects exposed, more questions will be raised than answered. Then we face an even greater challenge to piece together a coherent picture of what is an increasingly diverse and complicated phenomenon.

Bibliography

Aldering, G. et al. 2002, in Future Research Direction and Visions for Astronomy. Edited by Dressler, Alan M. Proceedings of the SPIE, Volume 4835, pp. 146-157 (2002), 146–157

Ambwani, K. & Sutherland, P. 1988, ApJ, 325, 820

Arnett, W. D. 1982, ApJ, 253, 785

Auer, L. 2003, in Stellar Atmosphere Modeling, Proceedings of an International Workshop held in Tübingen, Germany, 8-12 April 2002, ed. D. M. Ivan Hubeny & K. Werner (Astronomical Society of the Pacific), 3

Bailey, J. 1988, Proceedings of the Astronomical Society of Australia, 7, 405

Baron, E. 2003, Nature, 424, 628

Baron, E., Branch, D., Hauschildt, P. H., Filippenko, A. V., & Kirshner, R. P. 1999, ApJ, 527, 739

Baron, E., Hauschildt, P. H., & Mezzacappa, A. 1996a, MNRAS, 278, 763

Baron, E., Hauschildt, P. H., Nugent, P., & Branch, D. 1996b, MNRAS, 283, 297

Berger, E., Kulkarni, S. R., & Chevalier, R. A. 2002, ApJ, 577, L5

Branch, D. 1987, ApJ, 316, L81

—. 2001, PASP, 113, 169

—. 2004, to appear in 3-D Signatures of Stellar Explosions: astro-ph/0310685

Branch, D., Doggett, J. B., Nomoto, K., & Thielemann, F.-K. 1985, ApJ, 294, 619

Branch, D., Fisher, A., & Nugent, P. 1993, AJ, 106, 2383

Branch, D., Fisher, A., & Nugent, P. 1993, AJ, 106, 2383

Branch, D., Jeffery, D. J., Blaylock, M., & Hatano, K. 2000, PASP, 112, 217

Branch, D., Livio, M., Yungelson, L. R., Boffi, F. R., & Baron, E. 1995, PASP, 107, 1019

Branch, D. et al. 2004, ApJ, in preperation

Brown, J. C. & McLean, I. S. 1977, A&A, 57, 141

Burrows, A., Hayes, J., & Fryxell, B. 1995, ApJ, 450, 830

Burrows, A. & Thompson, T. A. 2003, in From Twilight to Highlight: The Physics of Supernovae, ed. W. Hillebrandt & B. Leibundgut (Springer-Verlag), 53

Cassinelli, J. P. & Haisch, B. M. 1974, ApJ, 188, 101

Castor, J. I. 1970, MNRAS, 149, 111

Chandrasekhar, S. 1960, Radiative Transfer (New York: Dover, 1960)

Chevalier, R. A. 1982, ApJ, 258, 790

Chevalier, R. A. & Fransson, C. 1994, ApJ, 420, 268

Chevalier, R. A. & Klein, R. I. 1978, ApJ, 219, 994

Chugai, N. N. 2000, Astronomy Letters, 26, 797

—. 2001, MNRAS, 326, 1448

Code, A. D. & Whitney, B. A. 1995, ApJ, 441, 400

Cropper, M., Bailey, J., McCowage, J., Cannon, R. D., & Couch, W. J. 1988, MNRAS, 231, 695

Daniel, J. Y. 1980, A&A, 86, 198

Decourchelle, A. et al. 2001, A&A, 365, L218

Deng, J. S., Hatano, K., Nakamura, T., Maeda, K., Nomoto, K., Nugent, P., Aldering, G., & Branch, D. 2001, in ASP Conf. Ser. 251: New Century of X-ray Astronomy, 238

Eastman, R. G. & Pinto, P. A. 1993, ApJ, 412, 731

Fassia, A., Meikle, W. P. S., Chugai, N., Geballe, T. R., Lundqvist, P., Walton, N. A., Pollacco, D., Veilleux, S., Wright, G. S., Pettini, M., Kerr, T., Puchnarewicz, E., Puxley, P., Irwin, M., Packham, C., Smartt, S. J., & Harmer, D. 2001, MNRAS, 325, 907

Fassia, A., Meikle, W. P. S., Vacca, W. D., Kemp, S. N., Walton, N. A., Pollacco, D. L., Smartt, S., Oscoz, A., Aragón-Salamanca, A., Bennett, S., Hawarden, T. G., Alonso, A., Alcalde, D., Pedrosa, A., Telting, J., Arevalo, M. J., Deeg, H. J., Garzón, F., Gómez-Roldán, A., Gómez, G., Gutiérrez, C., López, S., Rozas, M., Serra-Ricart, M., & Zapatero-Osorio, M. R. 2000, MNRAS, 318, 1093

Fesen, R. & Gunderson, K. 1996, ApJ, 470, 967

Filippenko, A. V. 1992, ApJ, 384, L37

—. 1997, Ann. Rev. Astr. Ap., 35, 309

Filippenko, A. V., Leonard, D. C., Riess, A. G., & Schmidt, B. P. 1999, in International Astronomical Union Circular, 2

Filippenko, A. V., Richmond, M. W., Branch, D., Gaskell, M., Herbst, W., Ford, C. H., Treffers, R. R., Matheson, T., Ho, L. C., Dey, A., Sargent, W. L. W., Small, T. A., & van Breugel, W. J. M. 1992a, AJ, 104, 1543

Filippenko, A. V., Richmond, M. W., Matheson, T., Shields, J. C., Burbidge, E. M., Cohen, R. D., Dickinson, M., Malkan, M. A., Nelson, B., Pietz, J., Schlegel, D., Schmeer, P., Spinrad, H., Steidel, C. C., Tran, H. D., & Wren, W. 1992b, ApJ, 384, L15

Filippenko, A. V. et al. 1995, ApJ, 450, L11

Fisher, A., Branch, D., Hatano, K., & Baron, E. 1999, MNRAS, 304, 67

Fisher, A., Branch, D., Nugent, P., & Vaughan, T. 1997, ApJ, 481, 89

Foley, R. J., Papenkova, M. S., Swift, B. J., Filippenko, A. V., Li, W., Mazzali, P. A., Chornock, R., Leonard, D. C., & Van Dyk, S. D. 2003, PASP, 115, 1220

Fryer, C. L. & Warren, M. S. 2004, ApJ, 601, 391

Fryxell, B., Olson, K., Ricker, P., Timmes, F. X., Zingale, M., Lamb, D. Q., MacNeice, P., Rosner, R., Truran, J. W., & Tufo, H. 2000, ApJS, 131, 273

Fryxell, B. A. & Arnett, W. D. 1981, ApJ, 243, 994

Gal-Yam, A., Ofek, E. O., & Shemmer, O. 2002, MNRAS, 332, L73

Galama, T. J. et al. 1998, Nature, 395, 670

Gamezo, V. N., Khokhlov, A. M., Oran, E. S., Chtchelkanova, A. Y., & Rosenberg, R. O. 2003, Science, 299, 77

Garnavich, P., Jha, S., Kirshner, R., Challis, P., Balam, D., Berlind, P., Thorstensen, J., & Macri, L. 1997, in International Astronomical Union Circular, 2

Gerardy, C. L. et al. 2003, ApJ, submitted; astro-ph/0302260

Germany, L. M., Reiss, D. J., Sadler, E. M., Schmidt, B. P., & Stubbs, C. W. 2000, ApJ, 533, 320

Goobar, A., Dahlen, T., Hook, I., & Aldering, G. 1999, in International Astronomical Union Circular, 2

Höflich, P. 2002, New Astronomy Review, 46, 475

Höflich, P., Gerardy, C. L., Fesen, R. A., & Sakai, S. 2002, ApJ, 568, 791

Hamilton, D. R. 1947, ApJ, 106, 457

Hamuy, M., Phillips, M. M., Suntzeff, N. B., Maza, J., González, L. E., Roth, M., Krisciunas, K., Morrell, N., Green, E. M., Persson, S. E., & McCarthy, P. J. 2003, Nature, 424, 651

Hamuy, M., Phillips, M. M., Suntzeff, N. B., Schommer, R. A., Maza, J., & Aviles, R. 1996, AJ, 112

Hatano, K., Branch, D., Fisher, A., Baron, E., & Filippenko, A. V. 1999, ApJ, 525, 881

Hatano, K., Branch, D., Qiu, Y. L., Baron, E., Thielemann, F.-K., & Fisher, A. 2002, New Astronomy, 7, 441

Hauschildt, P. H., Baron, E., & Allard, F. 1997, ApJ, 483, 390

Henry, R. B. C. & Branch, D. 1987, PASP, 99, 112

Hillier, D. J. 1994, A&A, 289, 492

Hjorth, J. et al. 2003, Nature, 423, 847

Hoeflich, P., Khokhlov, A., & Mueller, E. 1994, ApJS, 92, 501

Höflich, P. 1991, A&A, 246, 481

Hoflich, P. 1995, ApJ, 443, 89

Hoflich, P., Khokhlov, A. M., & Wheeler, J. C. 1995, ApJ, 444, 831

Höflich, P., Wheeler, J. C., Hines, D. C., & Trammell, S. R. 1996, ApJ, 459, 307

Howell, D. 2004, To appear in 3-D Signatures of Stellar Explosions

Howell, D. A., Höflich, P., Wang, L., & Wheeler, J. C. 2001, ApJ, 556, 302

Hu, J. Y., Qiu, Y. L., Qiao, Q. Y., Wei, J. Y., Filippenko, A. V., Martin, E. L., Li, W. D., Treffers, R. R., Modjaz, M., Moretti, S., & Tomaselli, S. 1997, in International Astronomical Union Circular, 1

Hungerford, A. L., Fryer, C. L., & Warren, M. S. 2003, ApJ, 594, 390

Hwang, U., Holt, S., & Petre, R. 2000, ApJ, 537, L119

Iben, I. & Tutukov, A. V. 1984, ApJS, 54, 335

Ignace, R. & Hendry, M. A. 2000, ApJ, 537, L131

Iwamoto, K., Mazzali, P. A., Nomoto, K., Umeda, H., Nakamura, T., Patat, F., Danziger, I. J., Young, T. R., Suzuki, T., Shigeyama, T., Augusteijn, T., Doublier, V., Gonzalez, J.-F., Boehnhardt, H., Brewer, J., Hainaut, O. R., Lidman, C., Leibundgut, B., Cappellaro, E., Turatto, M., Galama, T. J., Vreeswijk, P. M., Kouveliotou, C., van Paradijs, J., Pian, E., Palazzi, E., & Frontera, F. 1998, Nature, 395, 672

Iwamoto, K., Nakamura, T., Nomoto, K., Mazzali, P. A., Danziger, I. J., Garnavich, P., Kirshner, R., Jha, S., Balam, D., & Thorstensen, J. 2000, ApJ, 534, 660

Iwamoto, K., Nomoto, K., Hoflich, P., Yamaoka, H., Kumagai, S., & Shigeyama, T. 1994, ApJ, 437, L115

Jeffery, D. & Branch, D. 1990, in Supernovae, Jerusalem Winter School for Theoretical Physics, ed. S. W. J.C. Wheeler, T. Piran (World Scientific Publishing Co.), 149

Jeffery, D. J., Leibundgut, B., Kirshner, R. P., Benetti, S., Branch, D., & Sonneborn, G. 1992, ApJ, 397, 304

Jeffrey, D. J. 1989, ApJS, 71, 951

—. 1991, ApJ, 375, 264

Kasen, D., Branch, D., Baron, E., & Jeffery, D. 2002, ApJ, 565, 380

Kasen, D., Nugent, P., & Thomas, R. C.and Wang, L. 2003a, ApJ, submitted; astro-ph/0311009

Kasen, D., Nugent, P., Wang, L., Howell, D. A., Wheeler, J. C., Höflich, P., Baade, D., Baron, E., & Hauschildt, P. H. 2003b, ApJ, 593, 788

Khokhlov, A. 1991, A&A, 245, 114

—. 1994, ApJ, 424, L115

Khokhlov, A. M., Höflich, P. A., Oran, E. S., Wheeler, J. C., Wang, L., & Chtchelkanova, A. Y. 1999, ApJ, 524, L107

Kifonidis, K., Plewa, T., Janka, H.-T., & Müller, E. 2000, ApJ, 531, L123

Kim, A. G., Linder, E. V., Miquel, R., & Mostek, N. 2004, MNRAS, 347, 909

Knop, R., Aldering, G., Deustua, S., Goldhaber, G., Kim, M., Nugent, P., Helin, E., Pravdo, S., Rabinowitz, D., & Lawrence, K. 1999, in International Astronomical Union Circular, 1

Kulkarni, S. R., Frail, D. A., Wieringa, M. H., Ekers, R. D., Sadler, E. M., Wark, R. M., Higdon, J. L., Phinney, E. S., & Bloom, J. S. 1998, Nature, 395, 663

Kurucz, R. 1993, CD-ROM 1, Atomic Data for Opacity Calculations (Cambridge: Smithsonian Astrophysical Observatory)

Landi degl'Innocenti, E. 2002, in Astrophysical Spectropolarimetry, 1

Leibundgut, B., Kirshner, R. P., Filippenko, A. V., Shields, J. C., Foltz, C. B., Phillips, M. M., & Sonneborn, G. 1991, ApJ, 371, L23

Lentz, E. J., Baron, E., Branch, D., & Hauschildt, P. H. 2001, ApJ, 557, 266

Leonard, D. C. & Filippenko, A. V. 2001, PASP, 113, 920

Leonard, D. C., Filippenko, A. V., Ardila, D. R., & Brotherton, M. S. 2001, ApJ, 553, 861

Leonard, D. C., Filippenko, A. V., Barth, A. J., & Matheson, T. 2000a, ApJ, 536, 239

Leonard, D. C., Filippenko, A. V., Chornock, R., & Foley, R. J. 2002, PASP, 114, 1333

Leonard, D. C., Filippenko, A. V., & Matheson, T. 2000b, in American Institute of Physics Conference Series, 165–168

Li, H. & McCray, R. 1993, ApJ, 405, 730

Li, W., Filippenko, A. V., Chornock, R., Berger, E., Berlind, P., Calkins, M. L., Challis, P., Fassnacht, C., Jha, S., Kirshner, R. P., Matheson, T., Sargent, W. L. W., Simcoe, R. A., Smith, G. H., & Squires, G. 2003, PASP, 115, 453

Li, W., Filippenko, A. V., Gates, E., Chornock, R., Gal-Yam, A., Ofek, E. O., Leonard, D. C., Modjaz, M., Rich, R. M., Riess, A. G., & Treffers, R. R. 2001a, PASP, 113, 1178

Li, W., Filippenko, A. V., Treffers, R. R., Riess, A. G., Hu, J., & Qiu, Y. 2001b, ApJ, 546, 734

Li, W.-D., Li, C., Filippenko, A. V., & Moran, E. C. 1998, in International Astronomical Union Circular, 1

Li, W. D., Qiu, Y. L., Qiao, Q. Y., Zhu, X. H., Hu, J. Y., Richmond, M. W., Filippenko, A. V., Treffers, R. R., Peng, C. Y., & Leonard, D. C. 1999, AJ, 117, 2709

Liu, Q.-Z., Hu, J.-Y., Hang, H.-R., Qiu, Y.-L., Zhu, Z.-X., & Qiao, Q.-Y. 2000, A&A, 144, 219

Livio, M. 2000, in Type Ia Supernovae, Theory and Cosmology. Edited by J. C. Niemeyer and J. W. Truran. Published by Cambridge University Press, 2000., p.33, 33

Livio, M. & Riess, A. G. 2003, ApJ, 594, L93

Livne, E., Tuchman, Y., & Wheeler, J. C. 1992, ApJ, 399, 665

Lucy, L. B. 1999a, A&A, 344, 282

—. 1999b, A&A, 345, 211

—. 2001, MNRAS, 326, 95

—. 2002, A&A, 384, 725

—. 2003, A&A, 403, 261

MacFadyen, A. I. & Woosley, S. E. 1999, ApJ, 524, 262

Maeda, K., Nakamura, T., Nomoto, K., Mazzali, P. A., Patat, F., & Hachisu, I. 2002, ApJ, 565, 405

Marietta, E., Burrows, A., & Fryxell, B. 2000, ApJS, 128, 615

Matheson, T., Filippenko, A. V., Chornock, R., Leonard, D. C., & Li, W. 2000, AJ, 119, 2303

Matheson, T., Filippenko, A. V., Li, W., Leonard, D. C., & Shields, J. C. 2001, AJ, 121, 1648

Matheson, T. et al. 2003, ApJ, 599, 394

Mazzali, P. A., Cappellaro, E., Danziger, I. J., Turatto, M., & Benetti, S. 1998, ApJ, 499, L49

Mazzali, P. A., Chugai, N., Turatto, M., Lucy, L. B., Danziger, I. J., Cappellaro, E., della Valle, M., & Benetti, S. 1997, MNRAS, 284, 151

Mazzali, P. A., Danziger, I. J., & Turatto, M. 1995, A&A, 297, 509

Mazzali, P. A., Deng, J., Maeda, K., Nomoto, K., Umeda, H., Hatano, K., Iwaoto, K., Yoshii, Y., Kobayashi, Y., Minezaki, T., Doi, M., Enya, K., Tomita, H., Smartt, S. J., Kinugasa, K., Kawakita, H., Ayani, K., Kawabata, T., Yamaoka, H., Qiu, Y. L., Motohara, K., Gerardy, C. L., Fesen, R., Kawabata, K. S., Iye, M., Kashikawa, N., Kosugi, G., Ohyama, Y., Takada-Hidai, M., Zhao, G., Chornock, R., Filippenko, A. V., Benetti, S., & Turatto, M. 2002, ApJ, 572, L61

Mazzali, P. A. & Lucy, L. B. 1993, A&A, 279, 447

Mazzali, P. A., Nomoto, K., Patat, F., & Maeda, K. 2001, ApJ, 559, 1047

McCall, M. L. 1984, MNRAS, 210, 829

McKenzie, E. H. & Schaefer, B. E. 1999, PASP, 111, 964

Meikle, W. P. S. et al. 1996, MNRAS, 281, 263

Mezzacappa, A. et al. 2002, Bulletin of the American Astronomical Society, 34, 687

Mihalas, D. 1978, Stellar Atmospheres (San Francisco: W. H. Freeman)

Millard, J. et al. 1999, ApJ, 527, 746

Monard, L. A. G. 2001, IAU Circ. No. 7720

Nomoto, K. 2003, in Stellar Collapse, ed. C. L. Fryer (Kluwer)

Nomoto, K., Thielemann, F., & Yokoi, K. 1984, ApJ, 286, 644

Nugent, P., Baron, E., Branch, D., Fisher, A., & Hauschildt, P. H. 1997, ApJ, 485, 812

Nugent, P., Phillips, M., Baron, E., Branch, D., & Hauschildt, P. 1995, ApJ, 455, L147

Nugent, P. et al. 2004, ApJ, in preperation

Olson, G. L. 1982, ApJ, 255, 267

Patat, F. et al. 1996, MNRAS, 278, 111

Perlmutter, S. et al. 1999, ApJ, 517, 565

Phillips, M. & Heathcote, S. 1989, PASP, 101, 137

Phillips, M. M. 1993, ApJ, 413, L105

Phillips, M. M., Krisciunas, K., Suntzeff, N. B., Roth, M., Germany, L., Candia, P., Gonzalez, S., Hamuy, M., Freedman, W. L., Persson, S. E., Nugent, P. E., Aldering, G., & Conley, A. 2003, in From Twilight to Highlight: The Physics of Supernovae. Proceedings of the ESO/MPA/MPE Workshop held in Garching, Germany, 29-31 July 2002, p. 193., 193

Phillips, M. M., Lira, P., Suntzeff, N. B., Schommer, R. A., Hamuy, M., & Maza, J. 1999, AJ, 118, 1766

Phillips, M. M., Wells, L. A., Suntzeff, N. B., Hamuy, M., Leibundgut, B., Kirshner, R. P., & Foltz, C. B. 1992, AJ, 103, 1632

Pinto, P. A. & Eastman, R. G. 2000a, ApJ, 530, 744

—. 2000b, ApJ, 530, 757

Reinecke, M., Hillebrandt, W., & Niemeyer, J. C. 2002, A&A, 391, 1167

Riess, A. G., Press, W. H., & Kirshner, R. P. 1995, ApJ, 438, L17

—. 1996, ApJ, 473, 88

Riess, A. G. et al. 1998, AJ, 116, 1009

Rigon, L., Turatto, M., Benetti, S., Pastorello, A., Cappellaro, E., Aretxaga, I., Vega, O., Chavushyan, V., Patat, F., Danziger, I. J., & Salvo, M. 2003, MNRAS, 340, 191

Ruiz-Lapuente, P., Cappellaro, E., Turatto, M., Gouiffes, C., Danziger, I. J., della Valle, M., & Lucy, L. B. 1992, ApJ, 387, L33

Ruiz-Lapuente, P., Kirshner, R. P., Phillips, M. M., Challis, P. M., Schmidt, B. P., Filippenko, A. V., & Wheeler, J. C. 1995, ApJ, 439, 60

Saha, A., Sandage, A., Thim, F., Labhardt, L., Tammann, G. A., Christensen, J., Panagia, N., & Macchetto, F. D. 2001, ApJ, 551, 973

Schlegel, E. M. 1990, MNRAS, 244, 269

Serkowski, K., Mathewson, D. L., & Ford, V. L. 1975, ApJ, 196, 261

Shapiro, P. R. & Sutherland, P. G. 1982, ApJ, 263, 902

Sobolev, V. V. 1947, Moving Envelopes of Stars (Leningrad: Leningrad State University)

Stanek, K. et al. 2003, ApJ, 591, L17

Steinmetz, M. & Hoeflich, P. 1992, A&A, 257, 641

Stenflo, J. O. & Keller, C. U. 1997, A&A, 321, 927

Sutherland, P., Xu, Y., McCray, R., & Ross, R. 1988, in IAU Colloq. 108: Atmospheric Diagnostics of Stellar Evolution, 394

Swartz, D. A., Sutherland, P. G., & Harkness, R. P. 1995, ApJ, 446, 766

Tan, J. C., Matzner, C. D., & McKee, C. F. 2001, ApJ, 551, 946

Thomas, R. 2003, PhD thesis, University of Oklahoma

Thomas, R. C., Branch, D., Baron, E., Nomoto, K., Li, W., & Filippenko, A. V. 2004, ApJ, 601, 1019

Thomas, R. C., Kasen, D., Branch, D., & Baron, E. 2002, ApJ, 567, 1037

Trammell, S. R., Hines, D. C., & Wheeler, J. C. 1993, ApJ, 414, L21

Tran, H. D., Filippenko, A. V., Schmidt, G. D., Bjorkman, K. S., Jannuzi, B. T., & Smith, P. S. 1997, PASP, 109, 489

Trujillo Bueno, J. 2003, in Stellar Atmosphere Modeling, Proceedings of an International Workshop held in Tübingen, Germany, 8-12 April 2002, ed. D. M. Ivan Hubeny & K. Werner (Astronomical Society of the Pacific)

Trujillo Bueno, J., Landi Degl'Innocenti, E., Collados, M., Merenda, L., & Manso Sainz, R. 2002, Nature, 415, 403

Trujillo Bueno, J. & Manso Sainz, R. 1999, ApJ, 516, 436

Turatto, M., Benetti, S., Cappellaro, E., Danziger, I. J., della Valle, M., Gouiffes, C., Mazzali, P. A., & Patat, F. 1996, MNRAS, 283, 1

Turatto, M., Suzuki, T., Mazzali, P. A., Benetti, S., Cappellaro, E., Danziger, I. J., Nomoto, K., Nakamura, T., Young, T. R., & Patat, F. 2000, ApJ, 534, L57

Utrobin, V., Chugai, N., & Andronova, A. 1995, A&A, 295, 129

Wang, L., Baade, D., Höflich, P., Khokhlov, A., Wheeler, J. C., Kasen, D., Nugent, P. E., Perlmutter, S., Fransson, C., & Lundqvist, P. 2003a, ApJ, 591, 1110

Wang, L., Baade, D., Höflich, P., & Wheeler, J. C. 2003b, ApJ, 592, 457

Wang, L., Howell, D. A., Höflich, P., & Wheeler, J. C. 2001, ApJ, 550, 1030

Wang, L., Wheeler, J. C., & Hoeflich , P. 1997, ApJ, 476, L27

Wang, L., Wheeler, J. C., Li, Z., & Clocchiatti, A. 1996a, ApJ, 467, 435

—. 1996b, ApJ, 467, 435

Webbink, R. F. 1984, ApJ, 277, 355

Wheeler, J. 1990, in Supernovae, Jerusalem Winter School for Theoretical Physics, 1

Wheeler, J. C. & Harkness, R. P. 1990, Reports of Progress in Physics, 53, 1467

Wheeler, J. C., Lecar, M., & McKee, C. F. 1975, ApJ, 200, 145

Wood, K., Bjorkman, J. E., Whitney, B. A., & Code, A. D. 1996, ApJ, 461, 828

Woosley, S. E. 1993, ApJ, 405, 273

Woosley, S. E. & Eastman, R. G. 1997, in NATO ASIC Proc. 486: Thermonuclear Supernovae, 821

Woosley, S. E., Eastman, R. G., & Schmidt, B. P. 1999, ApJ, 516, 788

Yamada, S. & Sato, K. 1990, ApJ, 358, L9

Yamaoka, H., Nomoto, K., Shigeyama, T., & Thielemann, F. 1992, ApJ, 393, L55

Young, T. R. & Branch, D. 1989, ApJ, 342, L79

Zhang, Q. & Wang, Z. R. 1996, A&A, 307, 166